Fall 2019

A Laser Ion Source for Thin Film Deposition: Characterization of Source and Growth Conditions

Md Mahmudur Rahman
Old Dominion University, mahmud7778@gmail.com

A LASER ION SOURCE FOR THIN FILM DEPOSITION: CHARACTERIZATION OF SOURCE AND GROWTH CONDITIONS

by

Md Mahmudur Rahman
M.Sc. August 2013, Bangladesh University of Engineering and Technology
B.Sc. December 2009, Bangladesh University of Professionals

A Dissertation Submitted to the Faculty of
Old Dominion University in Partial Fulfillment of the
Requirements for the Degree of

DOCTOR OF PHILOSOPHY

ELECTRICAL AND COMPUTER ENGINEERING

OLD DOMINION UNIVERSITY
November 2019

Approved by:

Hani Elsayed-Ali (Director)

Helmut Baumgart (Member)

Shu Xiao (Member)

Bala Ramjee (Member)

ABSTRACT

A LASER ION SOURCE FOR THIN FILM DEPOSITION: CHARACTERIZATION OF SOURCE AND GROWTH CONDITIONS

Md. Mahmudur Rahman
Old Dominion University, 2019
Director: Dr. Hani Elsayed-Ali

Multicharged aluminum and carbon ions are generated by a laser-arc ion source. The design, construction, and testing of a compact laser ion source is demonstrated where the laser plasma is amplified by a high voltage spark-discharge. Optical emission and ion time-of-flight are measured for a spark-coupled laser aluminum plasma. A Q-switched Nd:YAG laser (wavelength λ = 1064 nm, pulse width τ ~7 ns, pulse energy $E_p \leq 260$ mJ, intensity $I \leq 15 \times 10^9$ W/cm^2) generates the Al plasma, while a synchronized spark-discharge enhances the ion flux and charge state. Time-integrated, spatially resolved optical spectra are used to obtain the plasma excitation temperature T_e and density n_e. The coupling of 2.4 J of spark-discharge to the laser plasma enhances the optical emission line intensity. The effective ion temperature T_i is calculated from a shifted Maxwell-Boltzmann distribution fit of the time-of-flight signal deconvolved for each ion charge. For $I = 3.5 \times 10^9$ W/cm^2, T_i is ~15 eV. For spark energy of 2.4 J coupled to the laser plasma, T_i increases to ~50 eV, and up to Al^{8+} is identified from the ion time-of-flight signal. The T_i obtained from the ion time-of-flight is much larger than T_e obtained from optical spectroscopy, although the plasma is considered to be in local thermodynamic equilibrium. This result is explained in view of the temporal development of the ablation plume and the different plasma regions probed by the two methods.

Multicharged carbon ions are also generated by a different laser-assisted spark-discharge (laser-arc) ion source configuration. A Q-switched Nd:YAG laser pulse (1064 nm, 7 ns, $\leq 4.5 \times 10^9$ W/cm^2) focused onto the surface of a glassy carbon target results in its ablation. The spark-discharge (~1.2 J energy, ~1 μs duration) is initiated along the direction of the plume propagation between the target surface and a grounded mesh that is parallel to the target surface. Ions emitted from the laser-spark plasma are detected by their time-of-flight using a Faraday cup. The ion energy-to-charge ratio is analyzed by a three-mesh retarding field analyzer. In one set of experiments, the laser plasma is generated by target ablation using a 50 mJ laser pulse. In another

set of experiments, ~1.2 J spark-discharge energy is coupled to the expanding plasma to increase the plasma density and temperature that results in the generation of carbon multicharged ions up to C^{6+}. A delay-generator is used to control the time delay between the laser pulse and the thyratron trigger. The highest charge amplification is recorded at ~0.9 μs time delay between the laser pulse and spark-discharge. Ion generation from a laser pulse when a DC high-voltage is applied to the target is compared to that when a spark-discharge with equivalent pulsed voltage is applied to the target. The laser-coupled spark-discharge (7 kV peak voltage, 810 A peak current) increases the maximum detected ion charge state from C^{4+} to C^{6+}, accompanied by an increase in the ion yield by a factor of ~6 compared to applying 7.0 kV DC voltage to the target.

Pulse laser deposition is used to deposit Al thin film on Si substrate. The growth conditions of the Al thin-film are investigated using a femtosecond pump-probe setup. The thermomodulation response from the thin film is measured. The goal is to measure the thin-film heat transfer as well as the thickness of the thin film. A femtosecond (800 nm, 100 fs FWHM, 0.15 nJ/pulse) laser pulse creates acoustic-strain pulse in the Al thin film. The time of flight of the acoustic pulse shows that the echoes of the acoustic pulse reflected from the metal/substrate interface change the optical reflectivity at the film surface. This information can be used to determine the thin-film thickness. The sensitivity of the femtosecond pump-probe setup is in the range of 10^{-6}.

On-line thickness measurement of Al thin-film during pulse laser deposition is not successful due to the roughness of the thin film; instead, thermal evaporation on Si substrate is demonstrated by femtosecond optical pump-probe spectroscopy. A femtosecond Ti:sapphire laser pulse (wavelength λ = 800 nm, pulse width $\tau \sim$ 100 fs, pulse energy Ep = 1.25 nJ) is used to instantaneously heat (pump) the surface of Al thin-film that changes the temperature profile of the target surface. The delayed probe pulse, also with λ = 800 nm, is used to investigate the change in transient thermoreflectance $\Delta R/R$ in order of 10^{-6} for the Al thin-film. The thermal expansion creates isotropic thermal stress in the Al surface that generates an acoustic wave of ultrasonic frequency. The travel time of the optically induced strain normal to the surface of the sample is measured to evaluate *in-situ* thickness measurement of Al in the range of 30 to 450 nm during the film deposition.

This dissertation is dedicated to my mother, “Moriom Sultana”

I would have never made it without you

ACKNOWLEDGMENTS

I would like to express my acknowledgment to several people, without their continuous support it was not possible to complete my dissertation

First of all I would like to thank my Ph.D. supervisor, Dr. Hani Elsayed-Ali, for his guidance and feedback throughout my doctoral studies. I'm extremely grateful to him for giving me the opportunity to work in the laser lab.

I would like to express my deepest appreciation to my committee Dr. Helmut Baumgart, Dr. Shu Xiao, and Dr. Bala Ramjee for the time from their busy schedules and valuable suggestions as members of my thesis committee.

I express my thanks to Oguzhan Balki, Haider Ali Shaim and Md Nizam Sayeed for the relentless support they provided throughout my graduate studies. The research would not have been possible without them. I also gratefully acknowledge the help of Dr. Wei Cao for training me on different instruments.

I would like to extend my thanks to Abdullah Al Mamun, Tanzila Tasnim, Obidul Islam, Waleed, and Didar for a great amount of support. Your helping hand and support always guide me to achieve my goal.

I wish to extend a heartfelt thank you to my mother, father and sister, and friends for their everlasting support and encouragement.

Finally, I would like to mention the most inspirational person in my life, my wife "Kathleen Rahman". I am so lucky for your daily inspiration and support.

TABLE OF CONTENTS

Page

Page

Page

APPENDICES

LIST OF FIGURES

Figure Page

Page

Page

Page

Page

Page

Page

Page

Page

Page

LIST OF TABLES

CHAPTER 1

INTRODUCTION

Multicharged ions are used in many applications including surface hardening of iron [1], the growth of diamond-like thin films [2], carbon ion radiotherapy [3], bandgap modification of TiO_2 [4], and synthesis of multi-layer graphene [5]. Although the singly-charged ions are used in most of these applications, the use of multicharged ions (MCIs) offers several advantages compared to the singly-charged ions. MCIs require less accelerating voltage to gain certain kinetic energy as well as a less magnetic field to focus and bend the ion beam [6]. Slow MCIs with potential energy in the hundreds or thousands of eV interact with the top atomic layer of the irradiated surface allowing for highly-localized energy deposition. Applications of MCIs include ion implantation [7], ion lithography [8], potential sputtering for surface patterning and cleaning [9], and carbon ion radiotherapy [10, 11]. In carbon radiotherapy, accelerated carbon ions are used to deliver a radiation dose to the tumor with minimal impact on the neighboring healthy cells. Carbon ions can reach deep-seated tumors that are difficult to access and are shown to be effective in their treatment [12, 13].

The interaction of high-power laser pulse with solids ablates the target material and generates plasma that is utilized in applications such as pulsed laser deposition, laser-induced breakdown spectroscopy, and in laser material processing. Recent developments in the generation of multicharged ions (MCI) from laser plasma are attracting significant interest [14, 15]. Applications of MCI sources include nanoprocessing, nanofabrication, ion implantation, ion lithography, cancer therapy, and secondary ion mass-spectrometry [6]. A variable energy radiofrequency quadrupole implanter was developed to implant Al^{2+} ions on a wafer, with energies of 1.0 MeV and 0.9 MeV [7]. Masked ion beam lithography by MCI was demonstrated by producing an array of hundreds of ordered micrometer wide dots using Xe^{44+} on poly (methylmethacrylate) resist [8]. Selective sputtering of impurity hydrogen atoms from a GaN surface by slow multicharged Ar^{q+} was demonstrated and suggested that the potential sputtering rather than the kinetic sputtering of impurities was dominant in the Ar^{8+} impact [16]. MCI was also used in protein fragmentation of biomolecules. Peptides plasmid DNA molecules were

irradiated with Xe^{44+} and dramatic molecular damage was reported [17]. Kitagawa *et al.* showed the use of carbon ions at the heavy-ion medical accelerator where C^{2+} or C^{4+} ions were produced for daily clinical treatments, mainly by a 10 GHz electron cyclotron resonance ion source [18]. Carbon implantation into titanium is known to enhance surface properties like wear behavior, mechanical hardness or the friction coefficient. An implantation technique was developed which allows simultaneous multicharged ion implantation (from C^{+} up to C^{4+}) to enhance the surface performance and microstructural modifications of the near surface region of Ti-6Al-4V [19].

1.1 Laser multicharged ion source

The use of laser plasma as an efficient source of highly-charged ions was reported in the early seventies [20]. Most of the initial laser ion source experiments were focused on elements with a low atomic number but later extended to heavier elements [21]. Laser-driven ion acceleration, using a nanosecond laser pulse was demonstrated in a number of experiments [22]. Laser-ablation generates an intense laser-plasma from any solid target and requires no differential pumping, as in the case of electron cyclotron resonance and electron beam ion trap sources [15, 23-26]. The ion yield of the laser ion source depends on the laser pulse energy, pulse width, spot size, and target material. The charge separation from laser plasma can be achieved by creating a uniform ion accelerating external electric field. Decoupling of the laser plume expansion, that is accompanied by ion separation, from external ion acceleration by allowing the plasma to expand in a field-free region then accelerating them is well-demonstrated [22]. For laser ion sources, scaling ion yield is accomplished by increasing the laser pulse energy. This approach is constrained by the need for larger laser systems and reduced pulse repletion rate. Laser-arc ion sources are an attractive approach as only a low-energy laser pulse is required for target ablation while the energy for ionization and plasma heating mainly comes from a spark-discharge coupled to the laser plasma [27, 28].

Laser MCI sources offer a pulsed, high flux source of ions from practically any solid target and require no differential pumping, as in the case of electron cyclotron resonance and electron beam ion trap sources [13, 14]. Although nanosecond lasers are mainly used in the generation of MCIs, femtosecond lasers have also been demonstrated to yield MCIs with high charge states [15,16]. The ion generation and the charge state of the MCIs are dependent on the

laser parameters, such as laser intensity and wavelength [17, 18]. However, in addition to the complexity of lasers delivering pulses with high energy, increasing the laser pulse energy generally limits the pulse repetition rate. The basic characteristics of plasma generated by nanosecond laser ablation have been the subject of many studies, but only a few studies considered the properties of a spark-discharge coupled to a laser-plasma generated in vacuum [19-22].

Multicharged ions are generated by ablating a solid target with a focused laser pulse where the power densities are between $10^9 – 10^{16}$ W cm^{-2} [29]. In a laser-produced plasma, the Knudsen layer is formed within a few particle-free paths near the target surface in which as few as 3 collisions per particle occurs [30]. Particles vaporized, sputtered, or desorbed reach equilibrium with each other within the Knudsen layer formed in a near-surface region during the laser ablation due to strong gas-phase interactions. This leads to a directional expansion perpendicular to the target surface. The ions freely drift into the vacuum, and ion charge-states are frozen at large distances. Furthermore, introducing an electric field increases the kinetic energy of ions; thus, separation of ions occurs with faster arrival time at the Faraday cup. More electrons are repelled, and more ions are exposed to the accelerating field. Space-charge limited flow in the ion sheath governs the ion extraction if the ion density is neglected during ion extraction by the external electric field [31]. The process of ion acceleration is initiated by electron acceleration by inverse Bremsstrahlung within the laser pulse duration. Due to the slower mobility of ions compared to the electrons, large Coulomb forces are formed between fast electron and ion layers in the early stages of plasma plume formation. The electric field due to the Coulomb forces accelerates ions with higher degree of ionization to higher kinetic energies. The ions with higher kinetic energies are located in the outer position of the plasma plume due to their higher flow velocity [32].

1.2 Laser-arc ion source

Cathodic-arcs, also called a metal-vapor-vacuum-arc or simply a vacuum-arc, are also used for ion generation [33]. Cathodic-arc occurs at different gas pressures with the background gas significantly participating in the discharge processes [34]. Cathodic-arcs have been investigated for applications in thin film deposition, ion implantation, and high current switches

[35]. The plasma generated by cathodic-arcs is highly ionized and contains a large number of MCIs with average kinetic energies of up to 100 eV [36]. However, cathodic-arcs are highly unstable [37]. The stability of the cathodic-arc depends on the arc energy, background pressure, electrode temperature, electrode shape, and electrode surface morphology. During the spark-discharge, the arc current is localized to cathode spots. The formation of the cathode spot is necessary to provide sufficient power density for plasma heating, electron emission, and current transport between the cathode and anode [37]. The metal plasma that is generated at the cathode spot contains an ion drift energy of about 10 to 200 eV depending on the ion mass [38].

Coupling of a spark-discharge to a laser-plasma is shown as an effective method of enhancing the MCI generation. Takagi *et al*. reported on a laser-triggered spark MCI source that can produce ions with energies from several hundreds of eV to several tens of keV and charge states up to Fe^{16+} using a spark-discharge (10.4 μF capacitor charged to 5 kV) [20]. Shaim and Elsayed-Ali reported enhancement of the total charge of a laser Al MCI source by a factor of ~9 and the generation of charge states up to Al^{6+} by a spark-discharge (0.1 μF capacitor charged to 5.0 kV) coupled to the Nd:YAG laser plasma. The spark was triggered by the laser plasma plume, and the discharge time was ~1.2 μs [23]. Coupling the arc to laser-plasma is used as an effective deposition method. Deposition of diamond-like carbon (DLC) films by laser-arc method was reported with a deposition rate of 5 nm/s [39]. The laser-arc deposition was also used in industrial hard coating applications where different substrate materials were coated by DLC resulting in films with frictional coefficient ~0.1 and hardness up to 80 GPa compared to steel [40]. Extreme ultraviolet light was generated by hybrid laser-assisted-vacuum-arc discharge plasmas using Sn-coated rotating-disc-electrodes [41]. Moreover, the laser-arc ion source was used as an effective method to increase the ion yield and charge state [42]. A laser ablation-assisted plasma discharge source was used to generate Al ions where laser ablation was accomplished by focusing a KrF excimer laser (1.2 J pulse energy, 40 ns pulse width, 248 nm wavelength) onto a solid Al target with a fluence of approximately 10 J/cm^2 [43]. Takagi *et al.* reported the generation of Fe^{16+} with ion energies from several hundreds of eV to several tens keV using a 125 J spark-discharge pulse energy coupled to a laser pulse [44]. Shaim *et al.* reported an Nd:YAG laser-arc ion source where the total Al ion yield from the laser-plasma was enhanced by a factor of ~9 and the maximum charge state was increased from Al^{4+} to Al^{6+} with spark-discharge coupling [32]. In that case, the spark-discharge was generated by a 0.1 μF

capacitor charged to a maximum 5.0 kV and the discharge time was ~1.2 μs [27]. Balki *et al.* reported the generation of the fully-ionized C^{6+} by a spark-discharge coupled to a carbon laser plasma with a spark discharge energy of ~0.75 J and a laser pulse energy of ~50 mJ [28].

1.3 Growth of the Al thin film by pulsed laser deposition

Laser ablation is a physical method that has emerged as an effective method for the growth of high purity thin films and nanostructured materials. By adjusting the deposition parameters, this technique offers the possibility to deposit and control the morphology of a large variety of materials from small metallic nanoparticles, to semi-continuous or continuous ultra-thin layered or multilayered films [45]. Most studies dealing with the deposition of metals by pulsed laser deposition concern noble metals for catalytic and optical applications. There are many reports in the literature describing the deposition of Al by PLD [19, 32–34]. One reason is the high reflectivity of Al in the first steps of the ablation process (~92% in the UV range), leading to a low ablation rate. In addition, plume deflection occurring as a result of Al target degradation under UV irradiation can also affect the deposition rate and the quality of the deposited layer [34]. For these reasons, it can be challenging to obtain thick aluminum films (>100 nm) by PLD.

1.4 Scope of research

The research presented in this dissertation provides a detailed experimental procedure for MCI production by means of a laser-spark ion source. The main goal is to increase the plasma ionization by coupling a spark discharge with the laser-plasma. The increase in the plasma ionization enhances the total ion generation along with the increase in maximum charge state. This dissertation is organized as follows:

Chapter 1 describes the MCIs, mechanism of laser ion source, literature review of previous work on laser multicharged ion source.

Chapter 2 explains the details of the optical emission spectroscopy, experimental setup of a LIBS, the laser-plasma characterization using optical spectroscopy.

Chapter 3 covers the details of the ion transport line module simulation. Faraday cup with three-grid retarding field ion energy analyzer, einzel lens, cylindrical ion deflector, and parallel plate ion selector is fabricated and tested.

Chapter 4 explains the details of the laser-spark MCI source. The laser produced plasma is reheated by deposition of external energy from a capacitor. The laser-spark plasma is characterized in terms of spark energy and laser fluence.

Chapter 5 describes a different configuration of the laser-arc ion source. The carbon plasma is generated between the target and the mesh parallel to each other.

Chapter 6 provides a detailed account of construction and optimization of a femtosecond pump-probe optical setup. pulsed laser deposition technique is applied to deposit Al thin-film. Later a modified optical pump-probe setup is also discussed to study the online thickness measurement of the Al thin-film deposited by the thermal evaporation.

Chapter 7 covers the conclusion and a summary of the work presented along with suggestions for future work.

CHAPTER 2

LASER PLASMA AND OPTICAL EMISSION SPECTROSCOPY

2.1 Introduction

Laser-produced plasma can be generated by applying a high-intensity laser beams on a solid, liquid or gas sample. Different types of laser can be used to generate laser plasma. The ablation process changes depending on the laser pulse type. We used a nanosecond laser pulse to ablate a solid Al target. For nanosecond laser pulse the ablation process is divided into three main stages. The first stage is the ablation and evaporation of the target material. The second stage is the interaction between the evaporated material and laser pulse resulting in the material heating and plasma formation. The third stage is the plasma plume expansion and rapid cooling [46]. The main absorption mechanisms of the plasma consist of the electron-atom inverse bremsstrahlung, electron-ion inverse bremsstrahlung, photoionization, and Mie absorption [47]. The contribution of each of these mechanisms depends on the laser pulse width, the stage of plasma formation, and the plasma properties.

2.2 Formation of laser plasma

The various complex mechanisms are involved in a laser ablation process includes laser absorption by the target material, evaporation, transient gas dynamics, ionization, and recombination. For nanosecond laser ablation, the electrons in the plume gain energy mainly by inverse bremsstrahlung. The electrons transfer their energy to the ions and the neutrals through collision processes. The time needed to transfer the energy from the electrons to the ions is much shorter than the nanosecond laser pulse duration resulting in the thermalization of the electrons and ions in the laser plume. Due to the small mass of the electrons compared to the ions, some of the thermalized electrons develop high velocities and escape earlier than the ions resulting in the formation of a transient electrostatic. The optical emission spectra are dominating when the radiation process decays significantly. During that stage, the excited electrons travel back to the

initial energy level and produce the optical emission spectrum [48]. Fig. 2.1 shows the basic mechanism of laser plasma generation. During the interaction of the laser pulse with a metal surface the electrons absorb the energy. The excited electrons transfer the energy to the phonon which is known as electron-phono coupling. However, for the nanosecond laser pulse ablation the ultrafast events like electron-phonon coupling is not observed as it takes place in 10^{-12} sec time range.

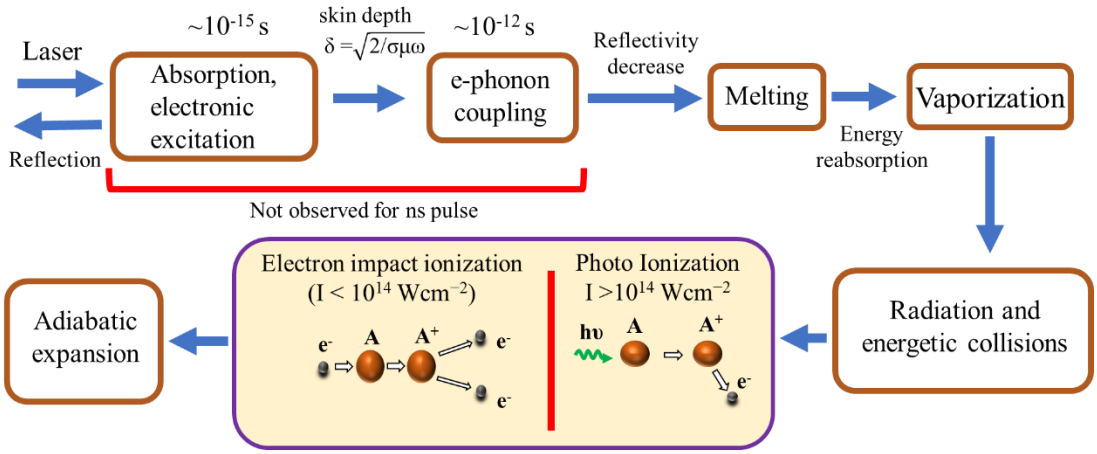

Fig. 2.1 Laser-material interaction process. Figure is reproduced after [48].

The main physical process of laser-plasma generation involves heat conduction, melting and vaporization of the target. The density and temperature of the laser-produced plasma can be so high that an efficient shielding of the target occurs during the laser pulse. For the nanosecond laser pulse, the absorbed laser energy heats up the target to the melting point and then to the vaporization temperature. In the laser produced plasma the ionization takes place. The two main mechanisms of ionization of laser plasma are electron impact ionization and photo ionization. The photoionization takes place for laser pulse intensity higher than 10^{14} W/cm^2 whereas, the electron impact ionization occur at laser intensity lower than 10^{14} W/cm^2 [48].

2.2.1 Electron impact ionization

Two dominant photon absorption processes can take place during laser material interaction which lead to breakdown and consequently the formation of plasma. The electron

impact ionization, also known as inverse bremsstrahlung (IB) absorption, takes place for comparatively low laser pulse intensity. In this process, a free electron gains kinetic energy from the laser beam. The energized electron starts a cascade of ionization and excitation through collision with neutral atoms. Fig. 2.2 shows the basic mechanism of the IB process. Initially the electron gains the energy from the laser pulse. The photons will couple into the available electronic or vibrational states in the material depending on the photon energy. In insulators and semiconductors, the absorption of laser light predominantly occurs through resonant excitations such as transitions of valence band electrons to the conduction band (inter-band transitions) or within bands (inter-sub-band transitions) [49]. The energized electron knocks out another electron from a neutral atom and starts an avalanche mechanism. The large density of neutrals in the initial vapor significantly enhances the IB process. The efficiency of the laser heating of the plasma by IB

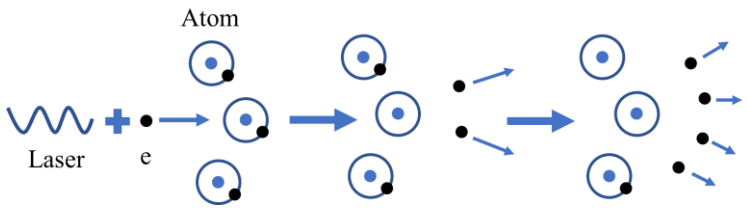

Fig. 2.2 Schematic illustration of inverse Bremsstrahlung absorption. Figure is reconstructed after [50].

decreases with the square of the laser wavelength when the degree of ionization is low and as the cube of the wavelength when the ionization is extensive [51]. As a result, the IB process is less efficient in the UV than in the visible part of the spectrum.

2.2.2 Multiphoton ionization (MPI)

The second mechanism of photon absorption is photoionization (PI) of excited species and, at sufficiently high laser intensity, multiphoton ionization (MPI) of excited or ground-state atoms. In general, an atom with ionization potential (E_i) can be ionized by the intense photon flux of Q-switched lasers by simultaneously absorbing $E_i/h\nu$ quanta. Since atoms and molecules exist only in discrete energy states, photon absorption cannot take place unless there is resonance

between an allowed state and the quantum energy *hν*. However, a virtual excited state of the atom to exist on absorbing a photon for a time dictated by the uncertainty principle. If photons are absorbed with sufficient frequency in a succession of higher energy states, ionization can result. Fig. 2.3 shows that an atom will acquire total E_i energy in a successive process by travelling *n* number virtual energy stage to get ionized. This process of successive absorption into a sequence of virtual states is known as multiphoton absorption [52].

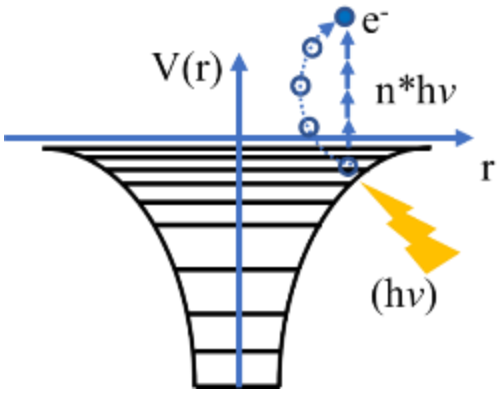

Fig. 2.3 Schematic illustration of multiphoton ionization. Figure is reconstructed after [50].

2.3 Optical emission spectroscopy

Optical emission spectroscopy (OES) is a common technique used to probe the excitation temperature T_e and density n_e in plasma [24-29]. Sabsabi *et al.* used LIBS in the air to analyze an Al alloy target and reported plasma T_e ~6730 K [3]. Abdellatif *et al*. studied Al laser plasma (λ = 1064 nm, τ = 7 ns, and laser intensity $I = 8.7 \times 10^{10}$ W/cm^2). Using OES, they reported n_e ~1.13×10^{18} cm^{-3} and T_e ~1.17 eV at 100 μm from the Al target surface [28]. Nassef and Elsayed-Ali developed a spark-discharge coupled laser induced breakdown spectroscopy (SD-LIBS) operating in air. Their spark circuit consisted of a 0.25 μF capacitor charged to 3.5 kV and triggered by the laser plasma. Spark-discharge coupling resulted in an intensity enhancement of the Al II at 358.56 line by a factor of 50 to 400 as the laser fluence was decreased from 48 to 4 J/cm^2 [21]. OES was used to probe the T_e by observing the Cu atomic lines at 510.55, 515.32, and 521.82 nm at delays of 1 and 4 μs after the laser pulse. For the laser plasma alone, with a

laser fluence of 48 J/cm^2, T_e exhibited a fast decay from ~9500 to ~6000 K at 10 μs after the laser pulse. While for SD-LIBS, this decay time increased to 60 μs. In that case, the persistence of the plasma for longer times, due to the spark, contributed to the increase in the measured time-integrated line intensity amplification [21]. Laser Al plasma generated in an electric field applied in the direction parallel to the plume expansion was previously characterized by ion time-of-flight combined with optical emission spectroscopy [30].

2.4 Laser Induced optical emission spectroscopy (LIBS)

There are several diagnostic techniques for characterizing a laser produced plasma including optical emission spectroscopy, mass spectroscopy, laser induced fluorescence, Langmuir probe, photothermic beam deflection, microwave and laser interferometry, and Thomson scattering [53]. Fast photography adds another dimension to ablation diagnostics by providing two-dimensional snapshots of the three-dimensional plume propagation [54]. These capabilities become essential for understanding the plume hydrodynamics, propagation, and reactive scattering. Laser Induced optical emission spectroscopy (LIBS) is a technique to determine the elemental composition. Compared to conventional methods, its ability to analyze solids, liquids, and gases with a little or no sample preparation makes it suitable for multi-element analysis. The method can be certified for analytical applications of interest in space applications, environmental monitoring, and quality control processes. To generate laser plasma, the laser must generate pulses of sufficient energy above a certain threshold whose values depend on the target and the laser characteristics. The excitation is accompanied by atomic, molecular and ionic spectral emission over a wide range of spectra. As the plasma cools, broadband emission decays and atomic and ionic lines are emitted. Several different experimental parameters such as laser wavelength, repetition rate, interaction geometry, surface conditions may affect the effective analytical possibilities of the optical emission spectroscopy method [55].

Fig. 2.4 shows the basic components of LIBS. LIBS involves focusing of a laser pulse on a target to generate optically induced plasma from the target. A delay generator can be used to trigger the spectrometer with respect to the laser pulse to record the time-resolved-spectroscopy of the laser plasma. The triggering option is usually integrated with most of the advanced

spectrometer. The 1:1 image of the laser plasma can be created, using two identical lenses, on the tip of an optical fiber which is connected to the spectrometer. The spatial information of the laser plasma plume is recorded by changing the position of lens L3 which changes the position of the plasma image. The element type and concentration of the target material are determined by analyzing the optical spectrum.

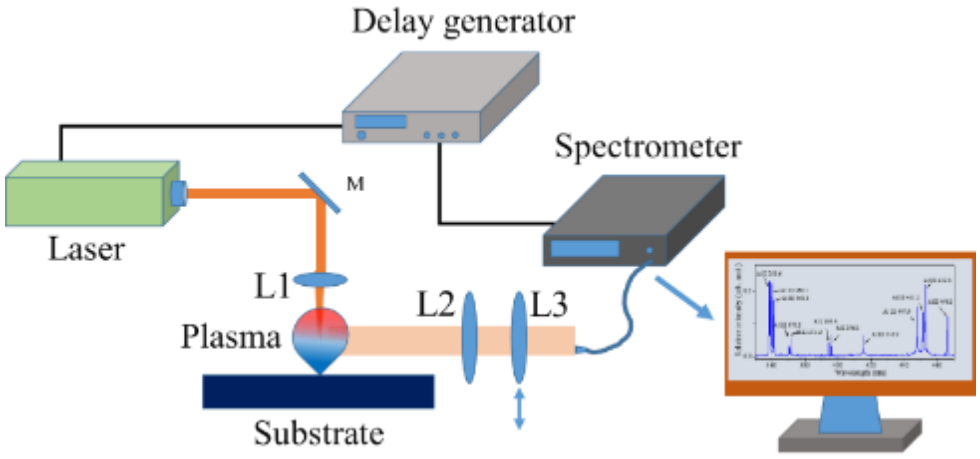

Fig. 2.4 Experimental setup of optical emission spectroscopy. The image of the laser plasma is created by combination of L2 and L2 lens. Delay generator is used to determine the time-resolved optical spectra. The spatially resolved optical spectra are achieved by changing the position of L3.

2.5 Emission process in laser plasma

The plasma becomes an electron-rich high-temperature environment at the early time of breakdown, due to the ionization process produced by multiphoton absorption and inverse bremsstrahlung. This results in the formation of time-dependent continuum radiation that may last for hundreds of nanoseconds. As the plasma propagates in the perpendicular direction to the target surface, the particle number density begins to decrease. The plasma begins to cool down at the end of the laser pulse. The recombination and de-excitation events dominate starts when the plasma power source laser pulse is terminated. During the plasma relaxation the neutral and ion line characteristic spectral line emission prevails. Three types of radiative transitions as

spontaneous emission stimulated emission, and absorption is possible due to the interaction of atom with radiation.

2.5.1 Line emission (bound-bound)

An atom or ion inside of a plasma emits radiation when radiative transitions between various quantum states occur. The interaction of ions and electrons with the radiating species is important in plasma spectroscopy. A schematic energy level diagram (Fig. 2.5) of a hydrogenic species representing the line radiation for electron transitions between bound levels. If υ_{pq} is the frequency of radiation when a transition from a level of principal quantum number p and energy $E(p)$ to a level of energy $E(q)$ occurs, then $h\upsilon_{pq} = E(p) - E(q)$ where h is the planks constant. However, the transition will depend on the transition-probability (A_{pq}) of the level p and q. [56]

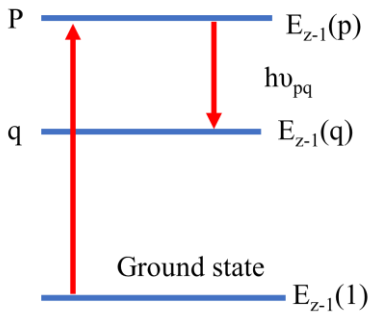

Fig. 2.5 Schematic of absorption and emission process. Figure is reconstructed after [56]

2.5.2 Bremsstrahlung radiation (free-free)

Continuous radiation can be observed experimentally originate from mainly three elementary processes. There are free-bound and free-free electron transitions corresponding to continuum [59]. Additionally, continuum may be superposed belonging to different ionic states of the same atomic species. Also, different atomic species present in the plasma may contribute

to continuous radiation. Free-free radiation occurs due to electron transition between two free energy levels. Fig. 2.6 shows that a moving electron radiates energy due to the change in momentum when accelerate or decelerate. If the electron has initial energy E_1 and velocity v_1. Due to the coulomb attraction with a positively charge particle the final energy and velocity are E_2 and v_2. The change is energy E_1-E_2 produces the $h\upsilon$ radiation where the h is the planks constant and υ is the frequency of the radiation [59].

2.5.3 Recombination radiation (free-bound)

Recombination radiation occurs when a free electron collides with ion. The electron can be captured and forms a new excited ion or a neutral particle. In dielectric recombination a free electron may be captured without the emission of radiation into a higher energy level of the ion. Instead of the emitted radiation one of the bound electrons is excited to a higher level by the excess energy. The new doubly excited atom or ion is de-excited by photon emission or through an inelastic collision. The rate of this process is known to be very small [57]. Three-body recombination may occur if two electrons collide with the ion simultaneously. One electron is captured into an upper excited level, and the other electron carries away the surplus energy. The captured electron cascades down to the ground state either by radiative transitions or collisions. Three-body recombination is in competition with radiative recombination and becomes more probable as the density increases [58].

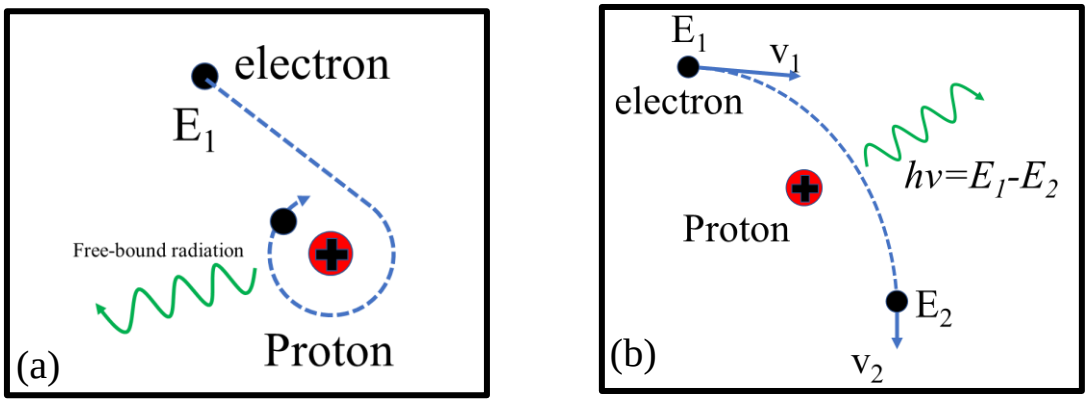

Fig. 2.6 Schematic of free-bound and free-free radiation. Figure is reconstructed after [56].

2.6 Plasma characterization

The characterization of laser-induced plasmas through the determination of their important parameters, such as the temperature, the electron density and the number densities of the different species present in the plasma, provides a better understanding of complex laser-plasma. The temperature is a crucial parameter that can be determined through the Boltzmann equation if local thermodynamic equilibrium (LTE) is satisfied. For LTE to exist in the plasma, the electron density must be high enough so that the collision rates exceed the radiative rates.

Boltzmann's law enables the determination of the excited state population of an atom or a molecule. Let N_1 and N_2 be the densities of particles of a given species, which are distributed into 1 and 2 levels, respectively. Boltzmann's law is described as,

$$\frac{N_2}{N_1} = \frac{g_2}{g_1} exp(-\frac{E_2 - E_1}{kT}) \tag{2.1}$$

where E_1 and E_2 are the energies of levels 1 and 2, g_2 and g_1 are the statistical weights of the energies of levels 1 and 2 and T is the temperature. The statistical weight or state density g_1 of a state of energy E_1 is related to the quantum number J_1, which corresponds to the total kinetic moment of the energy level i through the relationship $g_i = 2J_i + 1$ [59]. It is interesting to express the density of particles, N_i, of the energy state i as a function of the total relative density of all levels $\sum Ni = N$. Using (2.1), the following equation is obtained

$$N_i = N \frac{g_i}{U(T)} exp(-\frac{E_i}{kT}) \tag{2.2}$$

where T is the average temperature of the electrons in the energy state i and the partition function [60], which is written as

$$U(T) = \sum_i g_i exp(-\frac{E_i}{kT}) \tag{2.3}$$

This function acts like a normalization factor that ensures the fulfillment of equation (2.2)

An emission line depends on the probability of transitioning between the two involved energy levels and their electron population. In thermodynamic equilibrium, the population distribution of the energy state *i*, $N_i(E_i)$, is given by the Boltzmann distribution, which is presented in Equation (2.2). The absorption rate $N_1B_{12}I(\nu)$ represents the number of absorbed photons per volume per second that must be equal to total emission rate $N_2B_{21}I(\nu) + N_2A_{21}$ because of the energy conservation law. N_1 and N_2 represent the population of levels 1 and 2, $I(\nu)$ is the spectral intensity, and A_{21}, $B_{21,}$ and B_{12} are the Einstein coefficients of spontaneous emission, stimulated emission and spontaneous absorption, respectively.

$$[B_{21}I(\nu) + A_{21}]\, N_2 = B_{12}N_1I(\nu) \tag{2.4}$$

$$I(\nu) = \frac{A_{21}/B_{21}}{\left(\frac{N_1}{N_2}\frac{B_{12}}{B_{21}}\right)-1} \tag{2.5}$$

From the Boltzmann equation, we know

$$\frac{N_2}{N_1} = \frac{g_2}{g_1} exp\left(-\frac{h\nu}{kT}\right). \tag{2.6}$$

By substituting the value of $\frac{N_2}{N_1}$ in equation (2.5) by (2.6) we get

$$I(\nu) = \frac{A_{21}/B_{21}}{\left[\frac{B_{12}}{B_{21}}\frac{g_2}{g_1} exp\left(-\frac{h\nu}{kT}\right)\right]-1} \tag{2.7}$$

From plank's law, we know that the spectral radiance of a body,

$$B(\nu) = \frac{2h\nu^3}{c^2}\,\frac{1}{exp\left(-\frac{h\nu}{kT}\right)-1} \quad . \tag{2.8}$$

At local thermodynamic equilibrium $B(\nu)=I(\nu)$ and The Einstein coefficients can be written as,

$$\frac{B_{12}}{B_{21}} = \frac{g_1}{g_2} \qquad \frac{A_{21}}{B_{21}} = \frac{2h\nu^3}{c^2} \quad . \tag{2.9}$$

The electron temperature of a plasma is determined by the ratio of line intensities. If the plasma is optically thin for line radiation from level *j* to level *i*, the emission coefficient of spectral line can be defined as [50].

$$I_{ji} = \frac{hc}{4\pi\lambda_{ji}} A_{ji} N_j \tag{2.10}$$

where λ_{ji} is the wavelength of the emitted light, h is the Planck's constant (6.626×10^{-34} J·s), c is the velocity of light in vacuum (3×10^8 m/s), and A_{ji} is the transition probability, which is the probability per second that an atom in State 2 spontaneously emits in a random direction and is de-excited to State 1. If the upper levels are in local thermal equilibrium (LTE) the population density is entirely function of electron temperature. Using the Boltzmann relation, the ratio of two-line intensities is written as

$$\frac{\lambda_{ji} I_{ji}}{A_{ji} g_j} = \frac{hcN}{4\pi U(T)} \exp\left[-\frac{E_j}{kT}\right] \quad . \tag{2.11}$$

Taking the logarithm on both sides of Eq. (12) gives

$$\ln\left(\frac{\lambda_{ji} I_{ki}}{g_j A_{ji}}\right) = C - \frac{E_j}{kT} \tag{2.12}$$

where λ_{ji} is the wavelength, I_{ji} is the relative emissivity, g_j is the statistical weight of upper level, A_{ji} is the transition probability, E_j is excited level energy. A plot of $\ln\left(\frac{\lambda_{ji} I_{ji}}{g_j A_{ji}}\right)$ with respect to E_j for the observed spectral line follows a straight line and its slope $-1/kT$ represents the temperature.

The temperature is given by

$$T = -\frac{E_i - E_j}{k} \ln\left(\frac{I_j g_i A_i \lambda_j}{I_i g_j A_j \lambda_i}\right) \tag{2.13}$$

with the degeneracy of the upper and lower levels denoted by g, the transition probability by A, and the wavelength by λ. The advantage of the two-line method is avoiding the need for knowing the value for the effective path length through the source, the total particle number density, the partition function, the absolute intensity calibration of the detection system and absolute transition probabilities. Considerations when selecting a line pair are to have the wavelengths nearly identical and the difference in upper energies of the two transitions as large as possible. The first criterion is useful as the relative intensity calibration is easier and more accurate, and the second ensures that the calculated temperature is more reproducible and not over-sensitive to small fluctuations in the radiance ratio measurement.

2.7 Conclusion

The process of laser plasma formation is described in this chapter. The laser plasma generation depends on the various parameters including pulse energy and pulse duration. The basic principle of a nanosecond laser ablation of the Al and C target is described. The laser plasma is analyzed by optical emission spectroscopy. The spectral lines recorded from the laser plasma provide valuable information as plasma temperature and plasma density. The basic mechanism of laser induced breakdown spectroscopy is also discussed. The various radiation process of the laser plasma is discussed in this chapter. The plasma temperature evaluation method using Boltzmann plot is also discussed.

CHAPTER 3

MCI ION TRANSPORT LINE COMPONENTS SIMULATION

3.1 Introduction

The laser ion source is effective to generate multicharged ions. Although electron cyclotron resonance ion source (ECRIS) and electron beam ion sources (EBIS) are widely used to generate multicharged ions, laser ion source has several advantages compare to EBIS and ECIRS. Laser multicharged ion source (LMCIS) can produce an ion directly from any conducting, nonconducting and refractory targets, whereas both ECRIS and EBIS operate only with gases. The LMCIS is compact and transportable because the LMCIS does not require a large magnet or solenoid. The main component of LMCI is a laser system. The multicharged ions are generated by focusing a laser pulse on a solid target. In LMCIS the ions are produced from a very small spot on the target and the spot size depends on laser beam diameter. The generated ions can be collimated, focused, deflected and filtered by different ion optics.

Several groups have reported on the transport line components to enhance the analytical ability of the ion source. Veryovkin *et al.* reported an electrostatic grid energy analyzer, electrostatic lenses, and electrostatic mirrors to improve selectivity and to reduce the background noise of a time-of-flight mass-spectrometer [61]. Toker *et al.* reported a mass selection technique using einzel lens, deflector plates, and beam cleaner in the ion transport line based on the TOF principle [62]. Steele *et al.* reported the generation of focused chromium ion beam using a dipolar deflector and einzel lens in the transport line [63].

3.2 LMCI experimental setup

A Q switch Nd:YAG laser is used to ablate the solid target material in the laser multicharged ion source shown in Fig. 3.1. Positive voltage is applied to the target, and a grounded mesh is mounted in front of the target to create an external electric field between the target and mesh to accelerate the multicharged ions. The detail dimension of the experimental set up of the laser multicharged ion source is discussed in chapter 4. An einzel lens was provided by

Michael Korwin Pawlowski affiliated with the Département d'Informatique et d'Ingénierie, Université du Québec en Outaouais, QC, Canada. The einzel lens is integrated with the Al multicharged laser ion source in the applied research center in Virginia, United States. I would like to thank Haider Shaim for allowing me take the measurement of the ion optics. A second einzel lens and an electrostatic ion analyzer lens was constructed by Zachary Adams, Seth Berl, Brian Bishop, Derrick Jung, and Paul Rainey affiliated with Old Dominion University in Virginia, USA. The einzel lens and the electrostatic ion analyzer is added to the carbon multicharged laser ion source built by Oguzhan Bulki. My work is focused on the simulation and comparison of the simulation result with the experimental work conducted by Haider and Oguzhan.

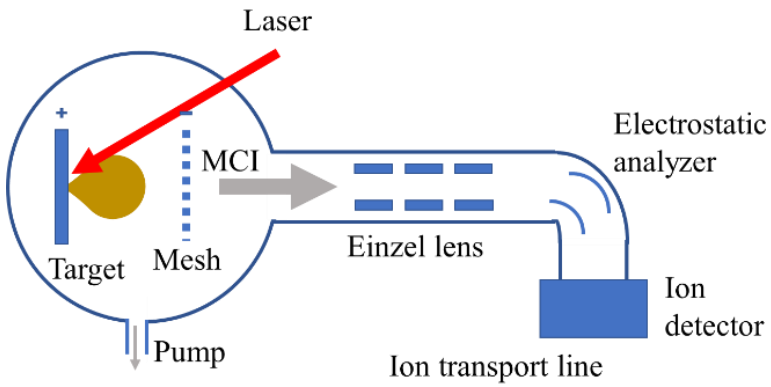

Fig. 3.1 The schematic diagram of a laser ion source. The main components are vacuum chamber, laser pulse, target, ion transport line, ion detector.

3.3 Einzel lens simulation

The three-electrode electrostatic lenses can be operated with fixed image position, but the magnification is not constant. Several groups have reported on the simulation and analytical solution of the three-electrode einzel lens. Omer sise *et al.* modeled multi-element cylindrical electrostatic lenses for focusing and controlling charged particles [64]. Three, four, and five cylindrical electrode lens properties were simulated as a function of lens voltage and electrode dimensions and for three-electrode lens, the line shape profile was also simulated [65]. Simulation results of the spherical and chromatic aberration coefficient that increases the size of

the final image of spot of multi-element electrostatic lens system were discussed [66]. Abdelrahman using SIMION, designed and optimized three-electrode einzel lens system for minimum oxygen beam diameter of 3 mm for energy of 5 keV [67]. The potential and the fields are evaluated by SIMION for cylindrical einzel lens [68]. Al-Moudarris *et al.* designed an einzel lens with small aberration and with minimum path trajectory using a non-classical variation technique to solve the paraxial ray equation of charged particles beams [69]. These simulated and analytical solutions show promising characteristic that the einzel lens can be used to focus ion beam depending on the focusing voltage and electrode dimension.

SIMION 8.1 [70, 71] ion optics simulation software is used for the modeling of the einzel lens. SIMION uses the 2D potential array approach to estimate the electrostatic fields created by the well-defined electrode geometry. A potential array contains a collection of a square mesh of points. The potentials at points outside of the electrodes are determined by solving the Laplace equation via finite difference methods [70]. SIMION works on the Laplace differential equation for computing the electric and magnetic potential for zero charge volume density with the electrode's geometries and potentials as the boundary condition. However, large density ions significantly distort the electrostatic potential field, in that situation the Poisson equation is used to estimate the potential field. For computation we have chosen a geometry representing closely the actual experimental chamber used. The model simulated here is a three-electrode einzel lens as our experimental one. Electrode length is L1 = L2 = L3 = 33 mm and inner diameter is 43 mm as shown in Fig. 3.2. The gap between the two electrodes is 10 mm. To simulate the ion source, experimentally obtained spatial distribution (fitted with Gaussian distribution) at knife edge is used. In SIMION model we defined the spatial distribution of the ion source with Gaussian 3D distribution with mean at origin and FWHM of 40 mm calculated from the knife-edge experiment, though the energy distribution was fitted by Coulomb-Boltzmann shifted model by Torrisi *at el.* and as shifted Maxwellian by Bulgakova *at el.* [72, 73]. The energy distribution of the Al ions is measured experimentally. Al^{1+}, Al^{2+}, Al^{3+}, and Al^{4+} has mean kinetic energy of 2.66 kV, 4.75 kV, 8.5 kV and 11.5 kV, respectively. The FWHM of energy distribution of Al^{1+}, Al^{2+}, Al^{3+}, and Al^{4+} are recorded as 1.09 kV, 1.52 kV, 3.58 kV, and 2.7 kV, respectively. The modeling of ion source distribution is very crucial for focusing of ion. Fig. 3.3 (a) and (b) shows the difference between cylindrical ion distribution and Gaussian 3D ion distribution. For cylindrical ion source Al^{4+} ion beam focus 11 mm before comparing to the Gaussian ion beam

focus, for – 3.5 kV voltage. The minimum beam diagram for cylindrical ion source is 1.2 mm whereas for 3D Gaussian distribution it is1.9 mm. The possible deviation between the experimental result and simulation is due to the nature of the ion source distribution as the ion trajectory has strong dependence on the ion source distribution.

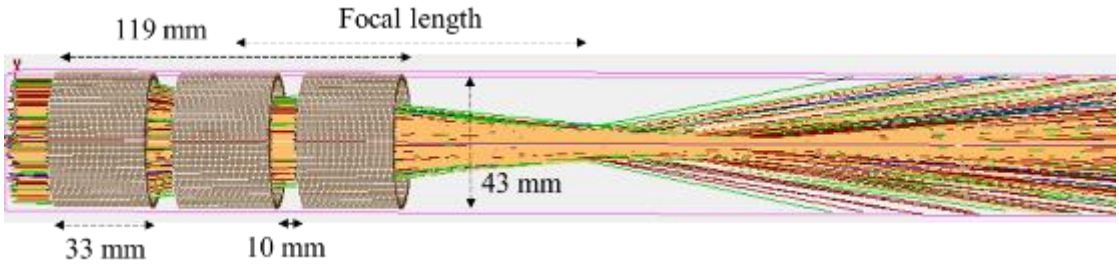

Fig. 3.2 Simulation result by SIMION. Al^{1+}, Al^{2+}, $Al^{3+,}$ and Al^{4+} charges are indicated by the color blue, red, green and yellow respectively

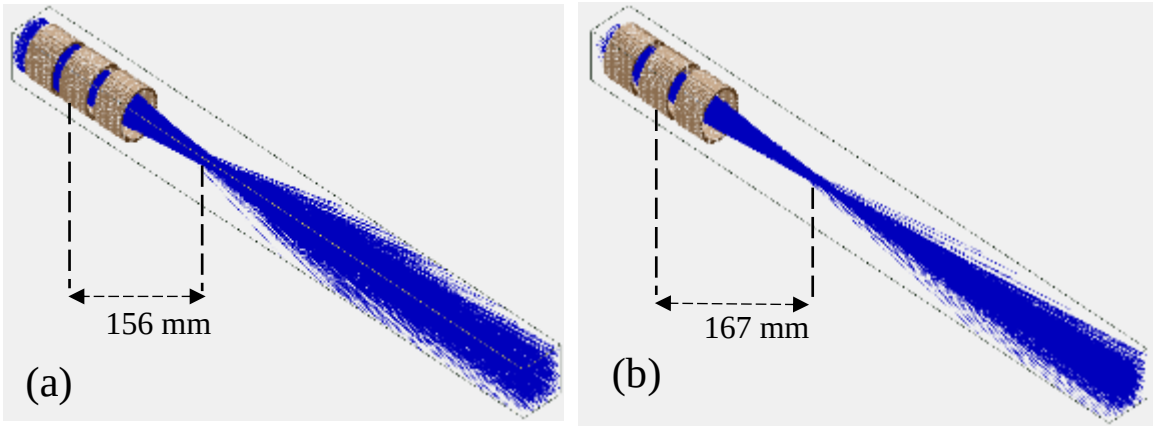

Fig. 3.3 Effect on ion trajectory for ion source distribution. Al^{4+} ions are focusing with applied voltage -3500 V and Gaussian energy distribution with mean 11.5 kV and FWHM 2.7 kV for (a) cylindrical distribution (b) Gaussian 3D distribution with a mean of 0 mm, Effect on ion trajectory for ion source distribution. Al^{4+} ions are focusing with applied voltage -3500 V and Gaussian energy distribution with mean 11.5 kV and FWHM 2.7 kV for (a) cylindrical distribution (b) Gaussian 3D distribution with mean of 0 mm, and standard deviation of 8 mm. Gaussian distribution of ions shows longer focal length.

The ion beam diameter is measured at 30 cm from the focusing electrode of the einzel lens (same as the distance from focusing electrode to knife-edge in the experimental chamber). The ions detected by the FC travel through a 40 mm circle at 55.5 cm far from the central electrode. Fig. 3.4 shows simulated results for the effect of change of Einzel lens voltage on the ion beam focus diameter at knife-edge using SIMION. Increase of the einzel lens focusing voltage from zero to -3.5 kV, the beam diameter of the ions decreases continuously. The minimum beam diameter for Al^{1+}, Al^{2+}, $Al^{3+,}$ and Al^{4+} is ~2 mm, observed for einzel lens voltage of -2.8 kV, -2.8 kV, -2.7 kV and -2.6 kV respectively. The focal length of the higher charge state ion species affected more than the lower state ions. At -3.5 kV einzel lens voltage, Al^{1+}, Al^{2+}, $Al^{3+,}$ and Al^{4+} has the focal length of 180 mm, 170 mm, 167 mm and 165 mm, respectively.

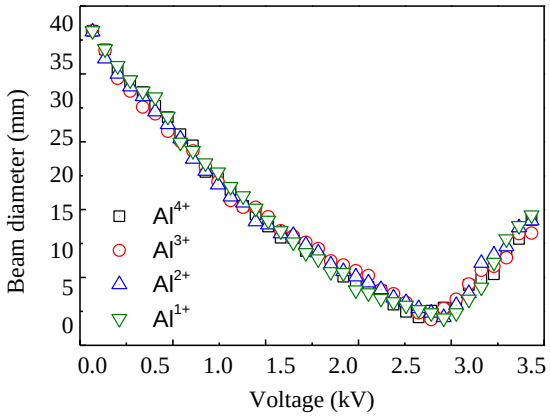

Fig. 3.4 Effect of change of einzel lens voltage on (a) beam diameter of Al^{+1}, Al^{+2}, Al^{+3}, Al^{+4} ions measured at 30 cm distance from Einzel lens.

The trend of focusing the ion beam for different charge states for varying einzel lens voltages in SIMION shows deviation from the experimental results. In the simulation, the ions are emitting from near the einzel lens with an experimentally obtained ion divergent, instead of ions emitting from the target to FC as the experimental could be the possible reason for this deviation. Also, the ion energy distribution difference between experimental and simulation runs can affect the number of ions delivered to the FC.

3.4 Electrostatic cylindrical deflector simulation

Previous results show that electrostatic ion analyzer is coupled with other devices to identify the charge state along with the ion energy distribution. Torrisi *et al.*, reported on laser ablation of different metals by using 3 ns Nd:YAG laser radiation, at 532 nm wavelength using mass quadrupole spectrometry assisted with electrostatic ion deflection system [74]. This system has a 45^0 electrostatic deflection to detect ion species in the energy range of 1 eV to 1 keV. This group has evaluated ion energy increments of Al, Ta, Zn, and Pb by simply recording different *E/z* values versus laser energy. Sha Shan *et al.*, analyzed the charge state and energy distribution of the ions produced by the laser ion source. Using the electron multiply tube (EMT) detector with electrostatic ion analyzer (EIA), the spectrum of the flight time of different charge state ions (Al^{12+}, Pb^{7+}) was achieved using Nd: YAG laser at 1064 nm with 8 ns pulse width and an energy of 1 J/pulse [75]. Electrostatic cylindrical deflector (ECD) alone is capable of selecting ions with E/z ratio and the ion energy distribution can be obtained from the information of E/z selection.

The ECD instrument consists of two curved parallel plates at different potentials and a radial cylindrical design with a deflection angle of 90^o as shown in Fig. 3.5. Ions enter the analyzer at one side and either pass through the other side or collide with the walls of the analyzer, depending on their initial kinetic energy. The ions selected by the ECD have a range of *E/z* obtained from the equation $\frac{E}{z} = eR_oE_r(R_o) = \frac{eV}{\left[2\,ln\left(\frac{R_2}{R_1}\right)\right]} = keV$, where *E* is the kinetic energy of the ion, E_r is the radial electric field inside the deflection plates, k is the geometric factor defined as $k = R_0/2\Delta R$. The inner radius R_1 = 5.69 inch, outer radius R_2 = 7.19 inch, mean radius R_0 = 6.44 inch, and $\Delta R = R_2 - R_1$, the gap width between the two cylindrical electrodes [76].

SIMION is used to simulate the carbon MCI trajectory in the EIA. The measurement is provided by Oguzhan Balki. The EIA geometry in SIMION is set similar to the experiment with the inner radius R_1 = 5.69 inch and outer radius R_2 = 7.19 inch. The voltage across the plates is varied. The maximum number of ions detected for ±500 V on the deflection electrodes with *E/z* = 2.2 keV. Fig. 3.6 shows the TOF spectrum in terms of the number of ions reaching the FC with ±500 V applied on the electrodes of the EIA. The EIA ion transmission increases with the MCI charge state. The number of particles in the ion source is 500 for each charge state. All the ions are simulated with both energy distribution and special distribution obtained from the

experiment. For ion energy distribution, a Gaussian 3D distribution is used with a mean of 2.3, 4.2, 7 and 10.3 keV for C^{1+}, C^{2+}, $C^{3+,}$ and C^{4+}, respectively. The FWHM of the Gaussian energy distribution is 1.5, 2.9, 3.8, and 4.3 keV for C^{1+}, C^{2+}, C^{3+} and C^{4+}, respectively. The simulated TOF corresponding to peak signal for C^{1+}, C^{2+}, $C^{3+,}$ and C^{4+} are 3.90, 4.58, 5.54, and 7.92 µs, respectively, whereas, the experimental TOF is 4, 4.6, 5.4, and 7.2 µs as shown in Fig. 3.6.

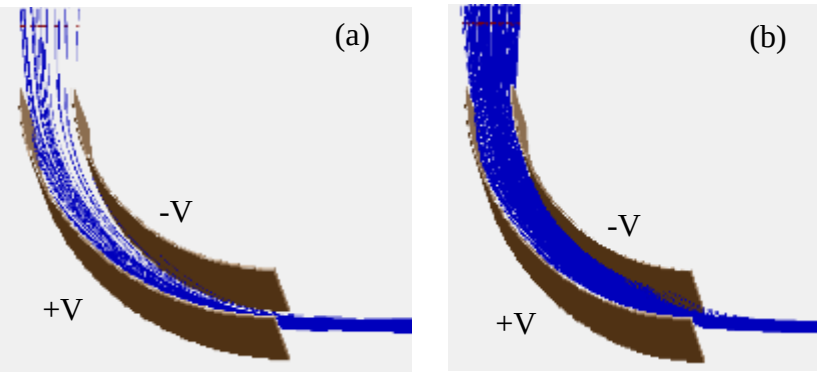

Fig. 3.5 Ion trajectory path for C^{4+} through the EIA. The applied voltage to the EIA (a) ±500 V, (b) ±300 V.

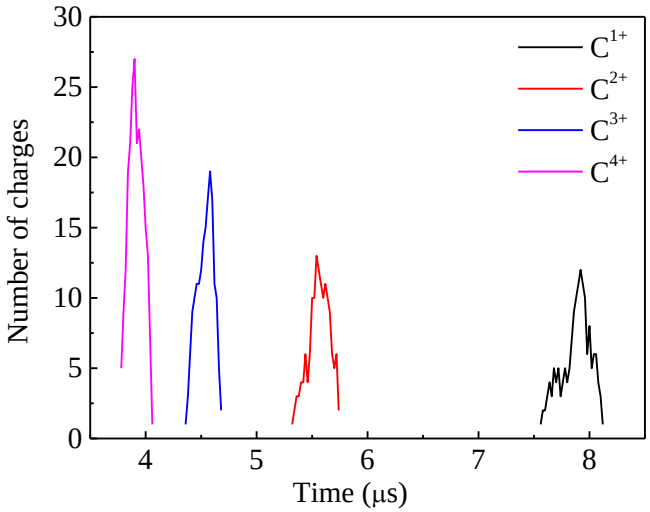

Fig. 3.6 Simulated TOF spectrum for C^{1+}, C^{2+}, $C^{3+,}$ and C^{4+}. Applied voltage to the EIA is ±500 V.

3.5 Space-charge effect on ion beam

SIMION has two methods for space-charge handling: the charge-repulsion method and the Poisson solver method. The repulsion method is an efficient and simple approximation method, whereas, the Poisson approach is complete but requires more set-up, thought, and care.

SIMION support a charge repulsion calculation method that provides estimate of space-charge effects in a system. The use of SIMION in space-charge effect calculation is reported in several papers [71, 77]. The SIMION methods are based on Coulombic repulsion between the charged particles. The coulomb repulsion is achieved by either of two methods. First method is the factor method where particles are represented as point charges or clouds. Second method is the beam method where the particles are represented as narrow charged beamlines. In the factor method the force on a charge particle due to the Coulombic repulsion from the other charged particles is superimposed with force due to the electric fields from the surrounding electrodes. Repulsion method does not consider any alteration of the surface charge distribution on the electrodes due to the space-charge (i.e. Poisson equation), nor the subsequent effect those rearrangements have on the space-charge. Further, at least in the case of "beam" repulsion where ions are flown by space-coherent integration, it does not consider the electric field forces from the space-charge in front of or behind the current particle locations on the current particles.

3.6 Space-charge in einzel lens simulation

In our einzel lens simulation work beam current is calculated as 50 µA for Al^{4+} and 43µA for Al^{1+}. No significant space-change effects are observed for this level of ion beam current. To detect the space-charge effect for our experiential set up the beam current is increased for Al^{1+} and Al^{4+} in SIMION simulation. Al^{1+} and Al^{4+} show significant space-charge effect when the ion beam current is increase beyond 100 µA for our experimental condition. Fig 3.7 (a) shows the effect of the space change effect on Al^{4+} ion beam focusing when the beam current is increased up to 100 µA. Fig 3.7 (b) shows the effect of the space change effect on Al^{1+} ion beam focusing when the beam current is increased up to 100 µA. The beam diameter at focus point is recorded as ~ 4.5 and ~ 2.5 mm for Al^{4+} and Al^{1+}, respectively and no significant effect on beam focusing

is observed up to 100 µA. Fig. 3.8 shows a linear increment in the beam diameter when the beam current is increased more than 100 µA and space-charge effect becomes significantly dominated.

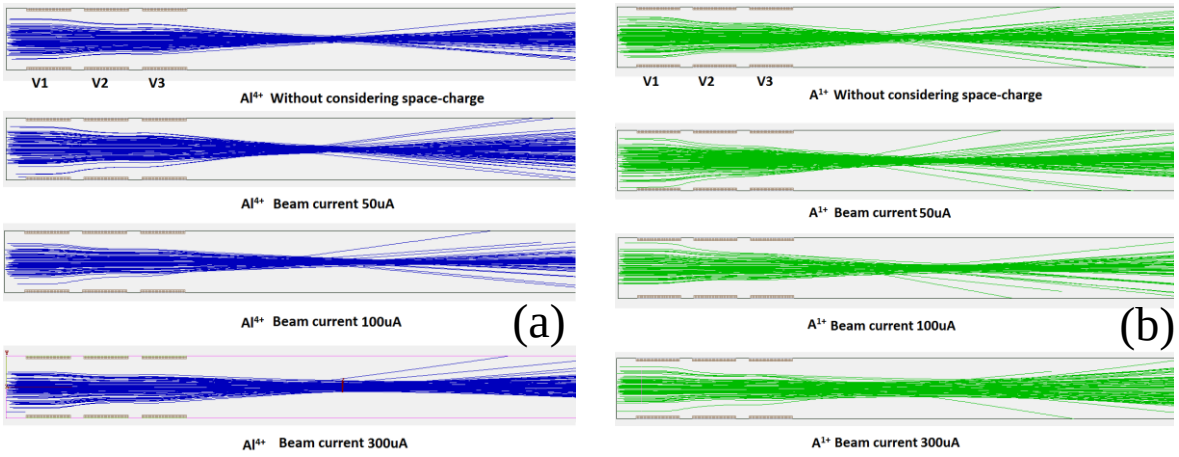

Fig. 3.7 The effect of space-charge by charge repulsion method for (a) Al^{1+} and (b) Al^{4+}. The einzel lens electrodes voltage are *V1*= 0 V, *V2*= -3000 V and *V3*= 0 V. The beam become diverge as the current increases.

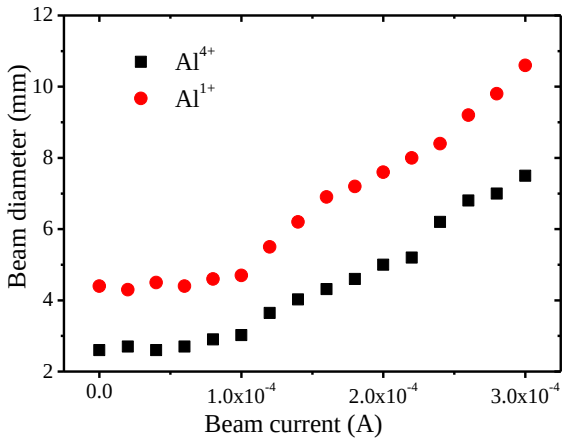

Fig. 3.8 Beam diameter is measured at 20 cm in front of the middle electrode of einzel lens.

3.7 Pulse forming network: High voltage pulse generation

The pulse-forming network serves the dual purpose of storing energy required for a single pulse as well as discharging that energy into the load in the form of a pulse of specified shape. The required energy may be stored either in a capacitor or in an inductor or in combinations of both. Networks in which the energy is stored in an electrostatic field are referred to as voltage-fed networks (Fig. 3.9). When the energy is stored in a magnetic field, networks are referred to as current-fed networks. In practice networks of the voltage-fed type are universally used because only with this type the gaseous-discharge switches such as spark gaps and thyratrons can be used. The current-fed network is not suitable for gaseous-discharge switch that allow high power operations. The voltage-fed network is constructed in ODU's laser lab to generate high voltage spark-discharge. The characteristic of pulse forming network is recognized as the impedance function for an open-circuited lossless transmission line [78]. However, the development of pulse-forming networks that represent a transmission line is a mathematical problem because no network having a finite number of elements can exactly simulate a transmission line [78].The degree of simulation will improve as the number of elements for a given network type is increased. The network pulse may exhibit overshoots and excessive oscillations, especially near the beginning and end of the pulse [78]. The oscillation in the signal arises due to the mismatch of load and line impedances. Nearly square voltage pulse can be generated if the line impedance is equal to the impedance of the load [78].

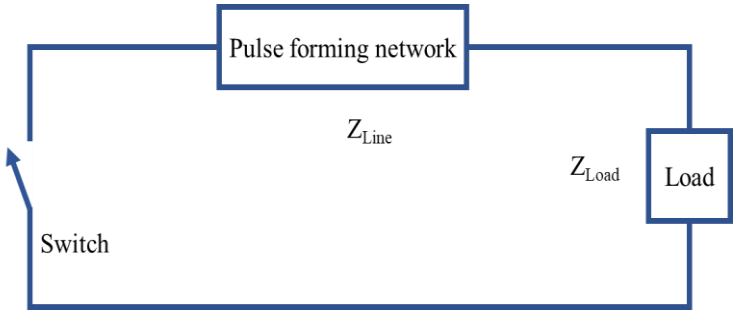

Fig. 3.9 Schematic diagram of the discharging circuit for a line type pulse generating circuit.

According to Rayleigh's principle the pulse duration can be calculated as $2n\sqrt{LC}$ where n is the number of stage in PFN, C is the capacitance and L is the inductance [78]. As an example, a pulse forming network with 30 pieces of 2 nF capacitor connected by a copper wire which typical inductance is 1 nH will produce a 84 ns nearly square shape pulse if the line resistance = $n\sqrt{L/C}$ matches with the load resistance [78]. A pulse forming network consist of total capacitance C = 60 nF and the input voltage of V = 18.25 kV can generate up to 10 J spark-discharge energy.as the energy stored by the capacitors is defined by $E = \frac{1}{2}CV^2$.

A thyratron can be used as a high-power electric switch. Thyratron works based on electron multiplication in ionized gas for this reason gas-filled thyratron can carry much more current than other vacuum tubes. This phenomenon is called Townsend discharge. Different kind of inert gases like mercury vapor, xenon, neon, and hydrogen are generally used in thyratron. In our experiment, hydrogen thyratron is used as a switch. The switching circuit is provided by Dr. Shu Xiao, Old Dominion University. I would like to thank him for providing the idea and training on the modification pulse forming network.

The thyratron is connected between the first end of pulse forming network and the electrode. A pulse cable is included between second end and the load for load matching, although they are not essential to the operation of the equipment. The pulse cable is usually added only for convenience in engineering and for greater flexibility in the physical location of the pulser and the load [78]. The resistance of the plasma is variable, and it depends on the plasma potential. In plasma, the density of the negative charge is equal to the density of the positive charge but on the scale of Debye length there can be charge imbalance [79]. In our design, shown in Fig. 3.10, the pulse forming network 5 equally length of RG58 cables are used to carry the high current and produce a resistance of 5 ohms. This represents the resistance of the line. To match up the impedance of the plasma with the pulse forming network a resistance branch has been built. 0.5 W of carbon resistance with value of 20 Ω is connected parallelly and series which creates 8 ohms resistance. It can be varied with different combinations. This resistance creates resistance matching with the plasma and produces a nearly rectangular pulse.

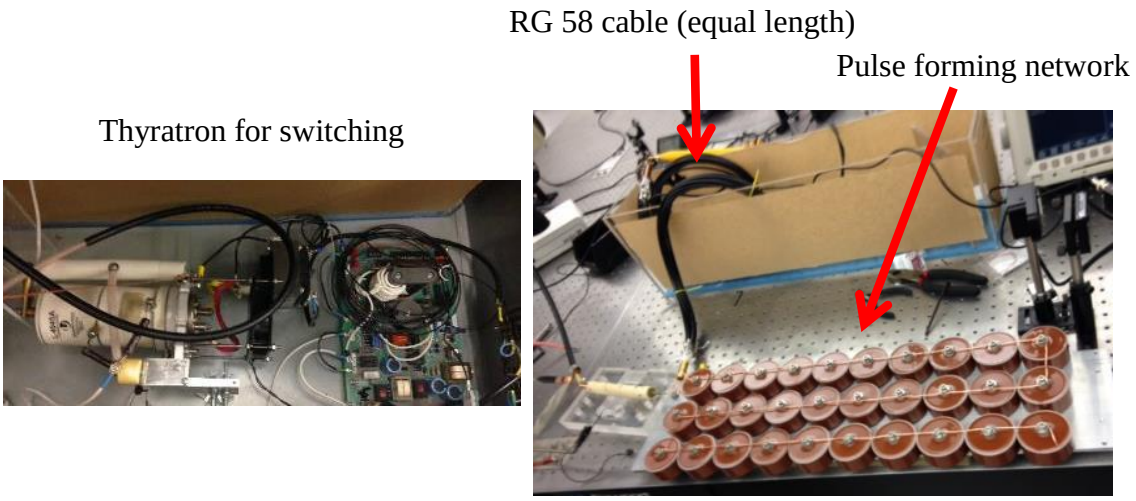

Fig. 3.10 The construction of the pulse forming network with thyratron switching and variable resistance.

A general voltage and current signal are shown in Fig. 3.11. The high voltage probe and high current coil are used to detect the voltage across and current through the spark discharge electrodes. The spark discharge is triggered by the laser pulse detected by the photo diode signal shown in Fig. 3.11 (a). The maximum voltage and current are measured as ~5 kV and ~800 A, respectively. The power of the spark discharge signal can be calculated from the value of the voltage and the current.

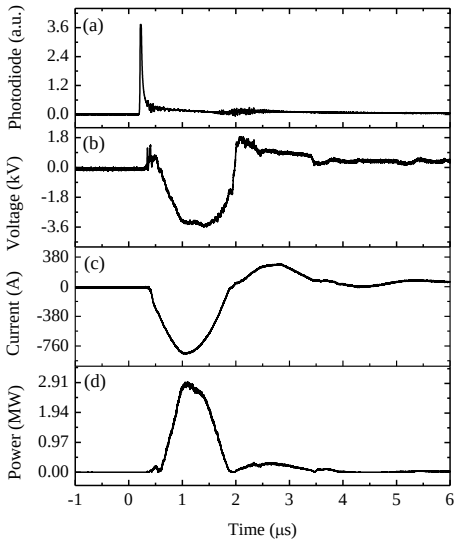

Fig. 3.11 (a) The photodiode signal of Nd:YAG laser pulse, (b) spark-discharge voltage measured across the electrodes (c) current measured through the electrodes (d) the calculated power from the voltage and current signal.

3.8 Conclusion

Simulation of the various components of the laser ion source is discussed in this chapter. SIMION 8.1 ion trajectory software is used to simulate ion optics. A three electrode einzel lens is simulated for aluminum multi charged ions, and the simulation results are compared with the experimental results. For carbon multicharged ion sources, an electrostatic energy analyzer is designed and simulated by SIMION 8.1. The simulation results are correlated with the experimental results. The basic construction of the high voltage pulse generator is also discussed. A pulse generator consists of a voltage-fed network designed to generate a voltage pulse width of 1 μs and pulse energy as high as 3 J.

CHAPTER 4

DIAGNOSTICS OF A SPARK-DISCHARGE COUPLED TO LASER ALUMINUM PLASMA BY OPTICAL EMISSION SPECTROSCOPY AND ION TIME-OF-FLIGHT

4.1 Introduction

We report on the diagnostics of a spark-discharge coupled to laser Al plasma by combined OES and ion time-of-flight (TOF) measurements. A pulse forming network (PFN) is used to produce a voltage pulse (pulse width ~1 μs) triggered by a variable time delay from the laser pulse. The optimum time delay between the spark-discharge initiation and the laser pulse is determined. The spark-discharge amplifies the ion flux, charge state, and the effective plasma ion temperature T_i. The intensity and linewidth of the neutral and the Al^{1+} optical emission lines are used to obtain the spatially-resolved T_e and n_e, respectively. The ion TOF and the OES are conducted on the Al laser plasma plume and on the laser spark-coupled plasma in order to elucidate the effects of spark coupling to the laser plasma on plasma properties. Deconvolution of the ion TOF signal into components from different species corresponding to different charge states is used to obtain the ion maximum charge state and T_i.

4.2 Experimental

A schematic of the spark-discharge coupled laser plasma source is shown in Fig. 4.1. A Q-switched Nd:YAG laser (λ = 1064 nm, τ = 7 ns, $E_p \leq 260$ mJ, $I \leq 15 \times 10^9$ W/cm^2, repetition rate 1 Hz) is used to ablate an Al target (99.9% pure, 0.5 mm thick, 5 cm in diameter) mounted on a target holder connected to a vacuum x-y manipulator. A ceramic standoff insulator is used to isolate the target from the vacuum chamber. The target is externally grounded. The vacuum is maintained by a turbomolecular pump at a base pressure in the low 10^{-7} Torr range. A biconvex lens L1 (f = 40 cm) is used to focus the laser beam on the target with the laser beam incident at an angle θ = 45° with the target surface. The laser spot on the target has an elliptical area of ~2.5 × 10^{-3} cm^2. The spark electrodes are made of cylindrical Al rods 5 mm in diameter with rounded

tips that are mounted on the multiport mini flange that holds the target. The gap between the two electrodes and the distance of the center point of the electrodes from the target surface are 5 and 6 mm, respectively.

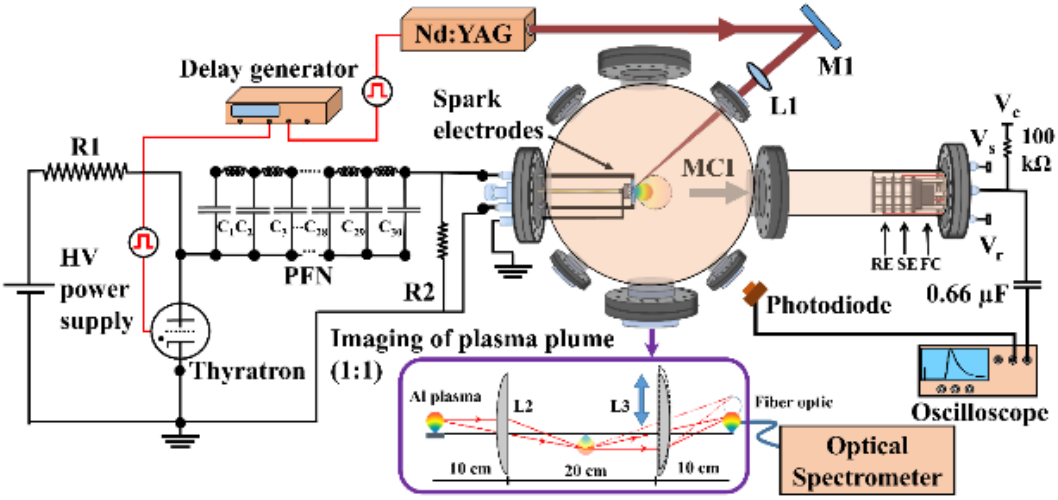

Fig. 4.1 Spark-discharge coupled laser plasma source. The pulse forming network (PFN) is triggered at a delay time from the laser pulse which can be varied using the delay generator. Two lenses (L2, L3) are used to image the plasma on a fiber optics bundle connected to the optical spectrometer. The ion detection system consists of a Faraday cup (FC), secondary electron suppressor ring (SE), and a three-grid retarding field ion energy analyzer, with (RE) referring to its central retarding electrode. *Vr* is the retarding voltage on RE, *Vc* the Faraday cup voltage, and *Vs* is suppressor ring voltage.

The PFN consists of 30 high-voltage capacitors (UHV 9 A, 2 nF, 40 kV TKD) mounted on an Al plate and connected in parallel with a 1.8 mm thick Cu wire, to keep the inductance low (~40 nH). The charging power supply (Glassman, PSLG30R5, 0-20 kV) is connected to R1 = 350 kΩ, which serves as a current limiting resistor. A hydrogen thyratron (L-4945A) is used to trigger the spark-discharge. A delay generator (SRS-DG645) is connected to trigger both the laser and the spark-discharge with a variable delay. The voltage across and the current through the spark electrodes are measured by a high-voltage probe (Tektronix, P6015A) and a current pick-up coil (Pearson 6595). A Si photodiode (Thorlabs DET10A, spectral range 200-1100 nm, rise time 1 ns, and active area 0.8 mm^2) is used to trigger the oscilloscope. The PFN is

terminated with a 300 Ω load resistor (R2) connected in parallel with the spark gap. The PFN can produce voltage pulses that are near square shape with a pulse width of ~1 μs.

Two identical uncoated UV fused silica plano-convex (Newport SPX016) lens L2 and L3 of 25.4 mm diameter and 5 cm effective focal length are used to create a 1:1 image of the plasma plume. The distance between the plasma plume and L2 is ~10 cm. L2 and L3 are placed on the same principle axis with 20 cm distance between them. L3 is mounted on a translation stage to scan the image of the plasma plume on the entrance of a fiber optic cable FC-UV-600 (spectral range 200-800 nm, fiber diameter 600 μm, length 2 m, field of view 22°, and numerical aperture 0.22), which guides the probed plasma emission to a spectrometer. Time-integrated, spatially-resolved optical emission spectra of the laser plasma are obtained using AvaSpec-ULS3648 (grating 1800 line/mm, blaze ~230 nm, resolution 0.1 nm, usable range 200-650 nm, slit width 10 μm). The optical spectrometer wavelength is calibrated by a low-pressure Hg lamp. Linearity of the detector response is checked by inserting a calibrated neutral density filter before the input of the fiber and checking the change in the detector response. Each optical spectrum is collected for 30 s with the laser operating at 1 Hz repetition rate. The background noise is measured and subtracted before recording each spectrum. The data is averaged for 30 s to average-out pulse-to-pulse fluctuations in the laser pulse energy and spark-discharge energy in addition to pulse shape fluctuations. The target is moved to expose a new surface spot to the laser after 30 pulses in order to avoid the formation of deep craters. The total number of ions detected decreases by ~6% for the 100^{th} laser pulse compared to the first laser pulse when the laser pulse intensity is 10×10^9 W/cm^2 with the laser pulses repeatedly hitting the same target spot.

The ion pulse is detected by a Faraday cup (FC), which is placed 1.54 m away from the surface of the Al target. The inner diameter and length of the ion drift tube are 10 and 125 cm, respectively. The FC consists of a 5 cm diameter Al cylindrical cup biased at −80 V with a suppressor ring mounted 1 cm away from the FC entrance to suppress the signal from secondary electron emission that is produced when the ions hit the FC. The voltage on the suppressor ring is kept at −120 V, which is found to completely suppress the secondary electron emission signal. Before reaching the FC, the ions pass a retarding field ion energy analyzer (RFA) consisting of three nickel grids, each with 70% open area, separated by 1 cm. The two outer grids are grounded while the central grid is connected to a variable voltage supply V_r. The central retarding electrode is positively biased with a variable voltage and is used to analyze the

extracted ion energy distribution. An oscilloscope (Tektronix DPO 3034, 50 Ω termination) is used to record the ion signal through a 0.66 µF coupling capacitor.

4.3 Results and discussions

4.3.1 Spark-discharge pulse characterization

The voltage across and the current through the spark electrodes for no delay set between the laser pulse and the spark-discharge are shown in Fig. 4.2. The total power dissipation from the spark is calculated from the voltage and current signals. The photodiode signal of the laser pulse indicates the approximate time the laser pulse interacts with the target. The capacitors in the PFN are charged to a maximum voltage of 10 kV. The width of the spark-discharge voltage pulse varies from pulse-to-pulse between 0.9 to 1.1 µs.

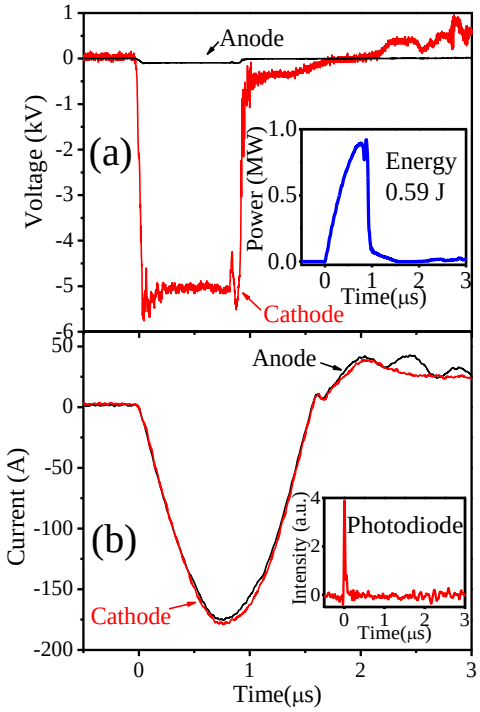

Fig. 4.2 (a) Measurement of the voltage signal on the anode and the cathode for 5 kV PFN charging voltage. Inset shows the spark-discharge power. The spark-discharge pulse energy is 0.59 J for 5 kV

charging voltage. (b) Measurement of the current through the anode and cathode. Inset shows the photodiode signal, indicating no measurable delay between the spark-discharge and the laser pulse.

Fig. 4.2 shows the spark-discharge energy deposited in the laser plasma for different charging voltages for delays of 0, 0.2, and 0.4 μs between the trigger of the laser pulse and that of the spark-discharge. The maximum spark energy of 2.4 J is achieved for 0.2 μs delay, as shown in the inset of Fig. 4.2. The spark-discharge energy drops for a delay > 0.2 μs due to the decay of laser plasma between the spark electrodes, which agrees with previous reports on laser plume expansion velocity [30-31].

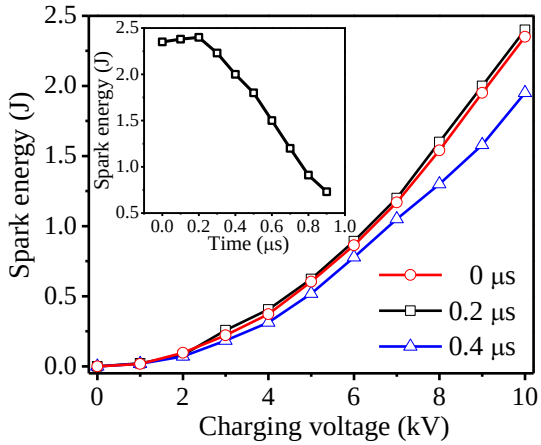

Fig. 4.3 The spark-discharge energy deposited in the laser plasma for different charging voltages up to 10 kV measured for delays of 0, 0.2, and 0.4 μs between the laser pulse and the spark-discharge. Inset shows the maximum spark energy deposition of 2.4 J into the laser plasma at 0.2 μs delay for 10 kV charging voltage.

4.3.2 Ion time-of-flight measurement

In addition to the thermal and adiabatic expansion velocities of the ions generated in the laser plasma, ions emitted from the plasma plume are accelerated by the double-layer potential at the interface of the expanding plasma with vacuum, which can significantly contribute to the ion energy. Fig. 4.4(a) shows the TOF distribution of Al ions measured by the FC for laser intensity from 2.9×10^9 to 4.5×10^9 W/cm^2 (E_p = 50 to 78 mJ). Ions with higher charge states are

accelerated to higher kinetic energies by the double-layer potential and are therefore detected earlier in the TOF signal. A retarding field energy analysis of the TOF ion signal is used to probe the ion energy.

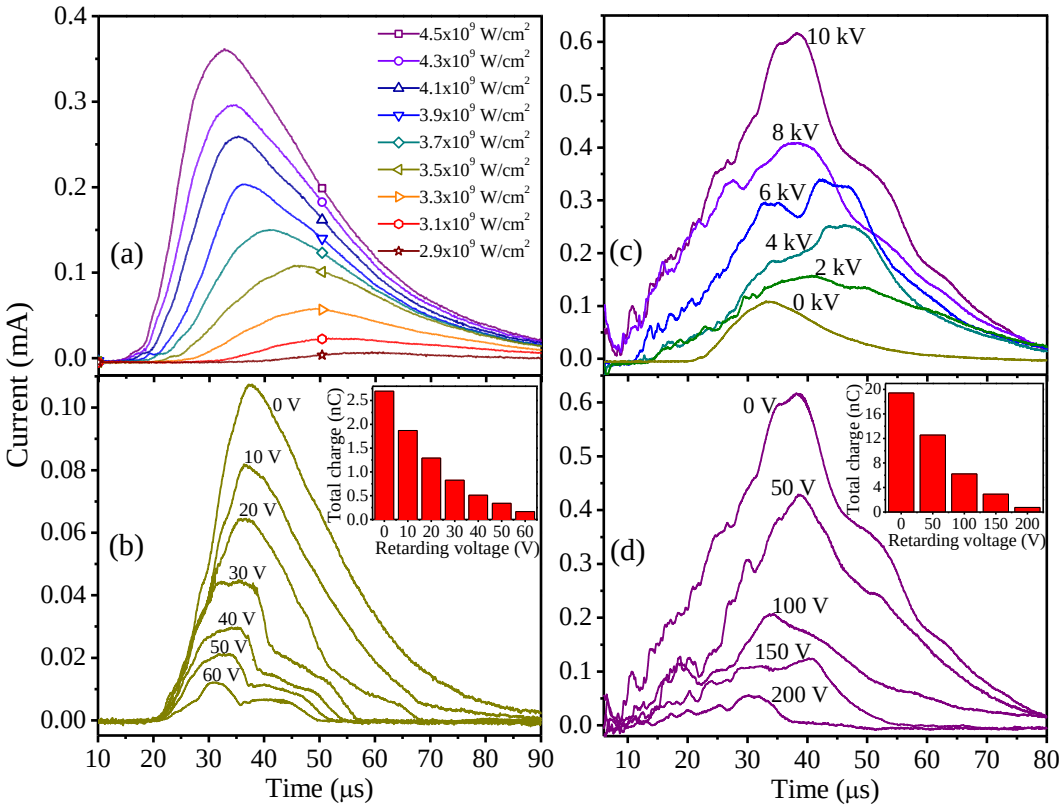

Fig. 4.4 (a) Ion time-of-flight (TOF) signal for different laser intensities (2.9×10^9 to 4.5×10^9 W/cm^2) without retarding voltage. (b) The effect of the retarding voltage on the TOF signal for a laser intensity of 3.5×10^9 W/cm^2. Inset shows the total ion charge detected for different retarding voltages. Only the laser pulse is used to generate the plasma in (a) and (b). (c) Amplification of the ion signal for different spark-discharge PFN charging voltages for a laser intensity of 3.5×10^9 W/cm^2. (d) The retardation of TOF signal from the laser-coupled spark-discharge 10 kV PFN charging voltage for a laser intensity of 3.5×10^9 W/cm^2. Inset shows the total ion charge detected as a function of charging voltage.

The retarding voltage stops all ions having kinetic energies less than zeV_0, where z is the ion charge state, V_0 is the retarding voltage, and e is the unit charge in Coulomb. Fig. 4.4(b) shows the TOF signal of the Al ions for different retarding voltages for a laser intensity of 3.5×10^9 W/cm^2 (E_p = 60 mJ). The inset in Fig. 4.4(b) gives the total ion charge detected as a function

of the retarding voltage. A retarding voltage of 60 V is sufficient to retard more than 96% of the generated ions. Fig. 4.4(c) shows the amplification of the ion TOF signal with 0-10 kV spark-discharge charging voltage for a laser intensity of 3.5×10^9 W/cm^2. Fig. 4.4(d) shows the ion signal with different retarding voltages when the spark-discharge is coupled to the plasma. The 2.4 J spark-discharge energy increases the total number of ions by a factor of ~7 compared to the laser pulse alone. Comparing Fig. 4.4(b) for the laser alone with Fig. 4.4(d) for the laser spark-discharge plasma, spark-discharge coupling increases the ion energy. With the spark-discharge, ~200 V is needed to retard 97% of the ions. Without the spark-discharge, ~90% of the total ions generated by laser ablation are stopped with 60 V applied to the retarding grid. To block almost all the ions, ~140 V is required. The full-width at half-maximum (FWHM) of the TOF increases with the spark-discharge due to the increased maximum charge state generated.

For laser plasma, the ion TOF signal can be fitted to a shifted Maxwell-Boltzmann (SMB) distribution [32-35]. The SMB distribution is established due to collisions in the dense plasma in the region near the target surface [32]. The thermalization of the plasma plume electrons and ions is often indicated by a good fit of the measured TOF signal to the SMB distribution. The sum of the SMB signals of the different ion charges fit the TOF signal of the observed ion pulse, which is composed of all ions. Different MCIs peaks are identified in the TOF signal as the retardation voltage is increased. As the retardation voltage is increased, the signal from each ion charge state is suppressed from the lower to the higher energy. Since the energy distribution of ions with each charge can be described by the SMB ion energy distribution, each ion state passing the three-grid analyzer have an energy distribution resembling a truncated SMB distribution. As a result, the individual MCI peaks become observable as the retardation voltage is increased. Fig. 4.5(a) shows the ion TOF signal passing the three-grid-analyzer for different retardation potentials. Al^{1+}, Al^{2+}, and Al^{3+} peaks are detected for a pulse laser energy of 3.5×10^9 W/cm^2. Fig. 4.5(b) shows that when 2.4 J spark-discharge is coupled to the laser plasma for the same laser conditions as Fig. 4.5(a), up to Al^{8+} is detected and the number of MCIs is increased. In the TOF signal, it is possible that the Al^{4+} peak is merged with the Al^{3+} peak.

The effective ion temperature can be extrapolated from the ion TOF signal by using the SMB distribution.

$$F(t) = \sum_i A_i \left(\frac{m}{2\pi k T_i}\right)^{\frac{3}{2}} \left(\frac{L^4}{t^5}\right) exp\left[-\frac{m}{2kT_i}\left(\frac{L}{t} - \sqrt{\frac{\Upsilon k T_i}{m}} - \sqrt{\frac{2zeV_0}{m}}\right)^2\right] \quad (4.1)$$

where $F(t)$ is the overall distribution of the ejected ions, Σ_i represents the summation of individual SMB distributions, A_i is a normalizing constant, m is the atomic mass of Al, L is the distance from the target to the FC, k is the Boltzmann constant, T_i is the effective ion plasma temperature, Υ is the adiabatic coefficient, for aluminum Υ = 5/3, z is the charge state, and V_0 is the equivalent accelerating voltage developed at the plasma-vacuum. In defining T_i as an effective ion plasma temperature, we follow the assumption that the ions extracted from the plasma have an energy distribution that corresponds to a thermalized ion distribution in the plasma core but shifted in energy by the adiabatic expansion of the plume and Coulomb acceleration by the double-layer potential.[33] In Eq. (1), $\sqrt{\Upsilon k T_i/m}$ represents the adiabatic expansion velocity, whereas $\sqrt{2zeV_0/m}$ is the velocity due to Coulomb acceleration. The ion TOF signals, for a laser intensity of 3.5 × 10^9 W/cm^2, with and without the spark-discharge and the corresponding SMB fits are shown in Fig. 4.5(c) and 5(d). The ion energy distribution of each charge state is assumed to follow the SMB distribution described in Eq. (1). The total energy of the Al ions without the externally applied electric field is $E_{zT} = (E_t + E_k) + zE_c$, where E_{zT} = total energy gain for charge state z, $E_t = \frac{3}{2}kT_i$ is the thermal energy, $E_k = \frac{\Upsilon}{2}kT_i$ is the adiabatic energy, and E_c = eV_0 is the Coulomb energy associated with the equivalent accelerating voltage due to the double-layer potential (V_0). For the deconvolution of the ion pulse into different ion charges, the ion energy distribution of each charge state is assumed to follow the SMB distribution and the maximum charge state z generated is based on the TOF measurement cutoff point in the early part of the pulse. The equivalent accelerating voltage developed inside the plasma due to the double-layer potential V_0 and the equivalent ion plasma temperature T_i are set as free variables. The most probable energy of each ion charge is separated by V_0. The sum of the SMB distributions of different ion charges fits the TOF signal of the observed ion pulse that is composed of all ions. For the SMB fit in Fig. 4.5(c), with the laser pulse only, we used V_0 ~ 60 V for the deconvolution of the TOF signal with Al^{1+}, Al^{2+}, and Al^{3+}. The effective ion temperature T_i that best fits the deconvolution is ~15 eV. The ion TOF signal we present is the average of the TOF for 30 pulses. Therefore, the target surface is expected to be free of oxides and adsorbed hydrogen after the first few pulses. Oxygen and hydrogen ions are not observed in the TOF signal. With the 2.4 J spark-discharge energy deposited in the laser plasma, charge states up to Al^{8+} are

fitted into SMB distribution in Fig. 4.5(d) assuming all detected ions are aluminum. Using a maximum charge state of Al^{8+} gives the best fit to the early part of the TOF signal. The deconvolution is performed by visually comparing the experimental TOF with the fit using different T_i and V_0 values. The agreement between the TOF ion signal and the SMB fit of Fig. 4.5(d) is confirmed by comparing the area under each curve which is proportional to the total charge. These two areas show 99% agreement. A maximum charge of Al^{8+} is consistent with the previously reported maximum charge state of Al^{6+} with 1.25 J spark energy coupled to the laser plasma [23]. From the deconvolution of the TOF signal with spark-discharge, T_i and V_0 are estimated to be ~50 eV and ~250 V, respectively. The slow ions referred to as Al_s^{1+} and Al_s^{2+} in Fig. 4.5(d), have extrapolated T_i and V_0 of 8 eV and 70 V, respectively. It was previously reported that the fast Al^{1+} ions are generated by direct multiphoton laser ionization, while the slow Al^{1+} ions result from collisional processes between the electrons and the neutrals [36]. The stretched tails in Fig. 4.5(c)-5(d) correspond to the slow Al^{1+} ions that contribute to the TOF signal. When the slow Al^{1+} ions are considered, better SMB fitting to the TOF ion signal is obtained. It is known that, after a few hundred nanoseconds from the laser pulse interaction with the target, the different ion species are not homogeneously distributed in the plasma plume. Therefore, there is some spread in the effective ion temperature within the plume [33]. However, this limitation has not been shown to significantly affect the ion energy distribution from the ns laser plasma [36,37].

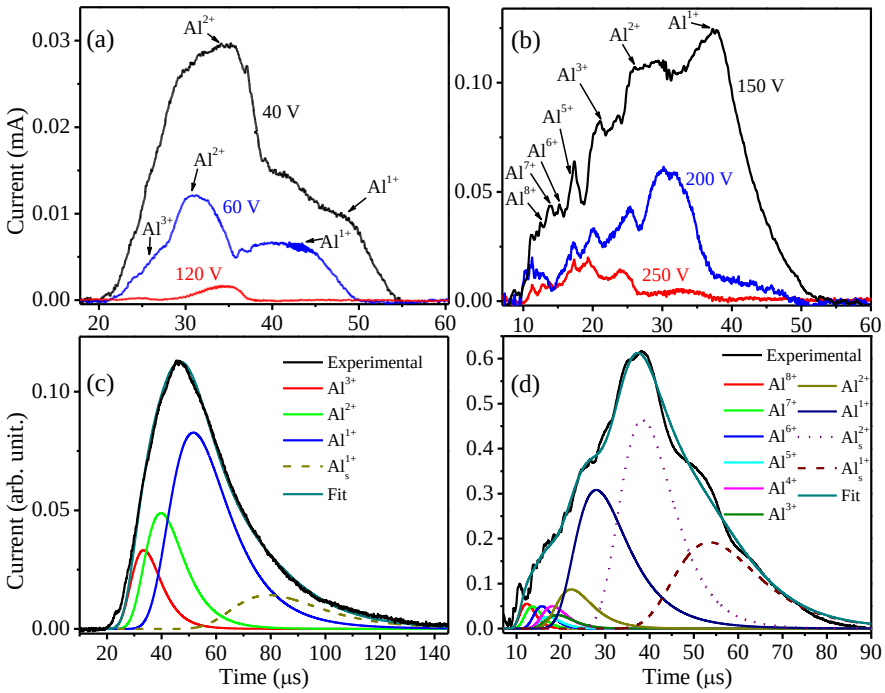

Fig. 4.5 (a) Individual Al ion charge peaks detected in the ion TOF signal passing a retardation potential. For *Vr*=60V, up to Al^{3+} is detected for a laser intensity of 3.5×10^9 W/cm^2. (b) Up to Al^{8+} is identified when 2.4 J spark-discharge energy is coupled to the laser plasma for 3.5×10^9 W/cm^2. The voltage on the retarding grid *Vr*=150 V. (c) Deconvolution of the ion TOF signal into different ion charges, each with an SMB distribution. Al^{1+}, Al^{2+}, and Al^{3+} are used to fit the TOF signals to estimate the Ti~15 eV. (d) The spark-discharge increases the generation of charge states up to Al^{8+} with Ti~50 eV. The same laser intensity is used in (a)–(d).

We note that the cross sections for interaction of different MCIs, ranging from H^+ to Ca^{20+}, with hydrogen gas was previously measured [38]. Considering an MCI with 100 eV per unit charge, the mean free path of the MCI is orders of magnitude longer than the experimental drift tube. Therefore, collisional loss of ions by charge transfer to the background gas is negligible in our experiment and the ion charge remains almost unchanged as the MCIs drift towards the Faraday cup.

4.4 Spectral intensity analysis

The Al laser plasma parameters are further characterized by time-integrated, spatially-resolved OES for a laser intensity of 5×10^9 W/cm^2 (E_P ~90 mJ) with the laser operating at a 1 Hz repetition rate. As shown in Fig. 4.6, the spark-discharge coupling to the laser plasma increases the intensity of the spectral lines for all Al spectral lines in comparison to those obtained with the laser alone at ~1 mm away from the target surface. Spectral lines up to Al III are observed in the present experiment.

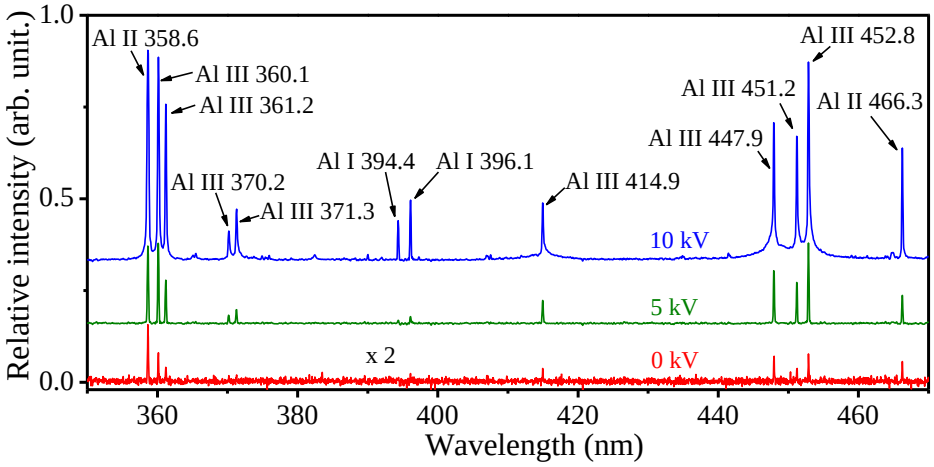

Fig. 4.6 Optical emission spectra (OES) of Al neutral and ion lines for spark-discharge at different PFN charging voltages. The laser intensity is 5×10^9 W/cm^2. The spectrum with the laser alone (0 kV) is multiplied by 2.

Fig. 4.7 shows the line intensities as a function of the PFN charging voltage. For the spark-discharge operating at 10 kV PFN charging voltage, the line intensities of the Al II 358.6, Al III 360.1, and Al I 394.4 nm are increased by a factor of ~9, ~14, and ~13, respectively compared to their intensities without the spark-discharge for a laser intensity of 15×10^9 W/cm^2. When the laser intensity is reduced to 5×10^9 W/cm^2, 2.4 J spark-discharge enhances the Al II 358.6, Al III 360.1, and Al I 394.4 nm by a factor of ~10, ~15, and ~37, respectively. It indicates that the spark-discharge increases the OES signal more for the low laser intensity than the high laser intensity. At the lower laser intensities, more neutrals are produced relative to the ions. As a

result, the neutral lines show more amplification with the spark-discharge compared to ion lines, for the lower low laser intensity.

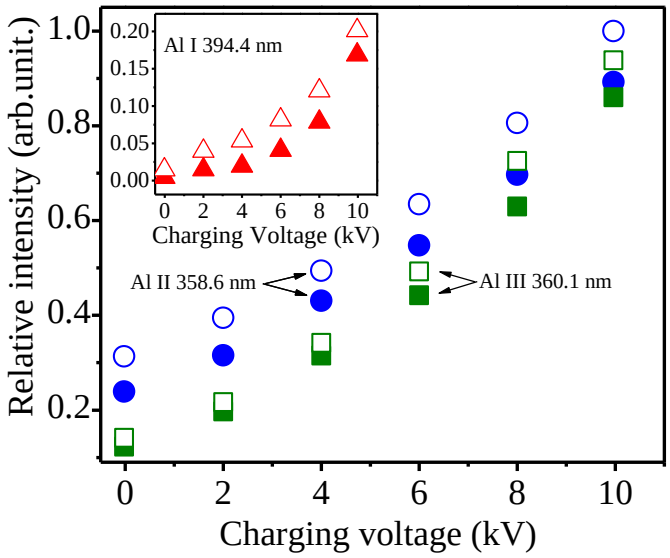

Fig. 4.7 Intensities of the Al II 358.6 (circle) and Al III 360.1 nm (square) optical emission lines as a function of PFN charging voltage (0-10 kV). Intensities of the Al I 394.4 (triangle) line is shown in the inset for clear depiction.

4.5 Measurement of plasma density and temperature

The Stark broadening profile of emission lines is commonly used to determine the plasma electron density n_e [39]. The Al II 281.6, and Al II 466 nm emission lines are used to determine n_e, because these lines are not affected by self-absorption [3,40]. The FWHM of a spectral line depends on electron and ion broadening [41]. As previously reported, the effect of the ion broadening is much smaller than that of electron broadening under similar conditions to that of our experiment [39-42]. Only electron broadening is considered in the FWHM of the Stark-broadened line, $\Delta\lambda_{1/2} = 2\omega.(n_e/10^{16})$, where ω is the electron impact broadening parameter and n_e is the electron density in cm^{-3}. The FWHM of the Hg 253.6 nm line, from a low-pressure Hg lamp, is measured as 0.1 nm. This linewidth is substracted from $\Delta\lambda_{1/2,}$ in order to account for the instrumental response affecting the FWHM of the Al II 281.6 nm line. The normalized

intensities are shown in Fig. 4.8 for the Al II 281.6 nm line. The FWHM increases when the PFN charging voltage is increased from 0 to 10 kV. The value of ω is taken as 0.042 Å for T_e = 10,500 K and $n_e = 0.1 \times 10^{17}$ cm^{-3} [43]. In Fig. 4.8, the Lorentzian function is used to fit the Al 281.6 nm line and obtain its widths. The FWHM values are recorded as 0.324, 0.358, and 0.386 nm and n_e is calculated as 5.3×10^{17}, 6.0×10^{17}, and 6.7×10^{17} for 0, 5, and 10 kV PFN charging voltages, respectively. The use of the value of ω for T_e = 10,500 K is based on the T_e value obtained from the Blotzmann plot in Fig. 4.9, which provides self-consistent analysis and gives values that shows agreement with previous studies of laser ablation of Al with an Nd:YAG laser [28].

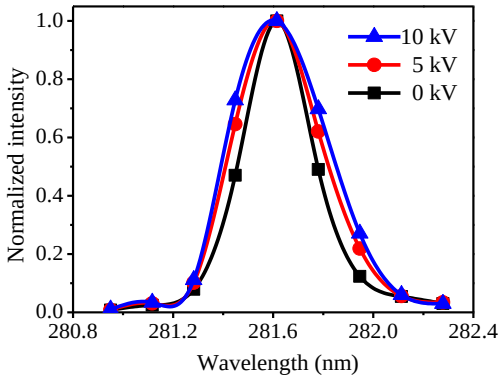

Fig. 4.8 The electron density is calculated from the Stark broadening profile of the Al II 281.6 nm line.

The ratio of the neutral emission lines is used because the ion emission lines have a short lifetime compared to the neutral lines, which results in a lower signal-to-noise ratio [44]. We have used the Al I emission lines to obtain T_e from the Boltzmann plot method. For optically thin plasma in local thermodynamic equilibrium (LTE), the population of an excited level can be related to the total density of neutral atoms or ions by the Boltzmann Law:

$$ln\left(\frac{\lambda_{ki} I_{ki}}{g_k A_{ki}}\right) = ln\frac{N(T)}{U(T)} - \frac{E_k}{kT_e} \tag{4.2}$$

where λ_{ki} is the wavelength, I_{ki} is the relative emissivity, g_k is the statistical weight of the upper level, A_{ki} is the transition probability, E_k is excited level energy, $U(T)$ is the partition function, $N(T)$ is the total number density of atoms. A plot of $\ln(\lambda_{ki} I_{ki}/g_k A_{ki})$ versus E_k for the selected spectral line follows a straight line with a slope $-1/kT_e$. The integrated intensity of the neutral

emission lines AI I 308.2, AI I 309.2, AI I 394.4, and AI I 396.1 nm are used to calculate T_e at a distance 0.5 mm away from the target surface, as shown in Fig. 4.9. The data in Fig. 4.9 are the average of 5 data points, while the error bar represents the range of data obtained from the five points. All spectroscopic parameters are taken from the NIST database [45].

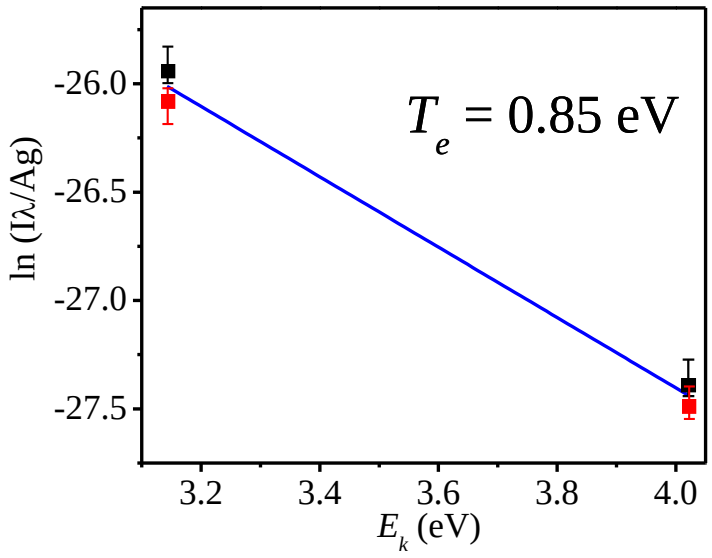

Fig. 4.9 Boltzmann plot is used to calculate the electron temperature T_e from the neutral lines AI I 308.2, AI I 309.2, AI I 394.4, and AI I 396.1 nm.

At the initial stage of laser ablation, the ablated atoms and ions experience collisions in the high-density Knudsen layer region near the target surface. The plume size expands, and the laser pulse energy is absorbed in the expanding plasma depending on the plasma density and the laser pulse duration [28]. Adiabatic expansion of the plasma occurs after the termination of the laser pulse. During expansion, the laser plasma cools down rapidly as the thermal energy is converted into kinetic energy [31]. The cooling of the plasma exterior is limited by ions regaining energy due to recombination processes. In Fig. 4.10, the emission line intensities peak at ~1 mm from the target surface. However, line intensities decrease as the plume expands 2-5 mm away from the surface of the target due to plasma cooling. The Al II 261.1 nm and Al II 281.6 nm persist further away from the target than the Al I 308.2 nm and Al I 309.2 nm,

probably due ion drift to regions with lower plasmas densities and, correspondingly, lower recombination rates.

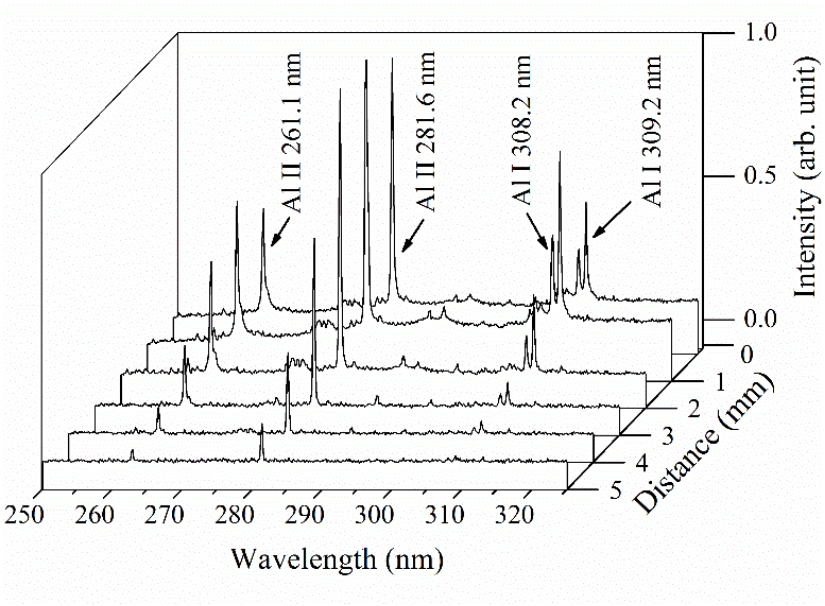

Fig. 4.10 Emission spectra of the selected Al lines along the direction of propagation of the plume. The laser intensity is 5 ×10^9 W/cm^2 and no spark-discharge is initiated.

Fig. 4.11 shows the spatial development of n_e and T_e calculated from the OES data collected along the plume propagation direction for 0 kV and 10 kV spark-discharge voltage. The maximum n_e and T_e measured from OES are ~6.6 × 10^{17} cm^{-3} and ~1.3 eV, respectively. To average-out pulse-to-pulse fluctuations, five spectra are averaged. The error bar in Fig. 4.11 gives the range of measurements from the five different spectra. Since the Al plasma is densest and hottest near the target surface (< 1 mm), the collisional processes between electrons, ions and neutrals are dominating in that region. The collisional processes further increase when the spark-discharge is coupled to the laser plasma causing further plasma heating and density increase. The spark discharge is expected to connect the two spark electrodes through the laser plasma in a path that is close to the target since the current conduction occurs mostly through the dense highly conductive plasma near the target. Also, the spark-discharge coupling to the laser plasma increases the plasma volume by ionizing more atoms at the external parts of the plume.

As a result, the high n_e is sustained for a longer distance (also time) with the spark compared to that with the laser alone. For example, at a distance 8 mm from the target surface, n_e drops to ~2.2 × 10^{17} cm^{-3} for the laser pulse alone, whereas with the spark-discharge n_e is ~5.2 × 10^{17} cm^{-3} at the same distance. The T_e, shown in Fig. 4.11 decreases rapidly over the distance 0 to 2 mm due to the rapid conversion of thermal energy into kinetic energy as the plasma expands.

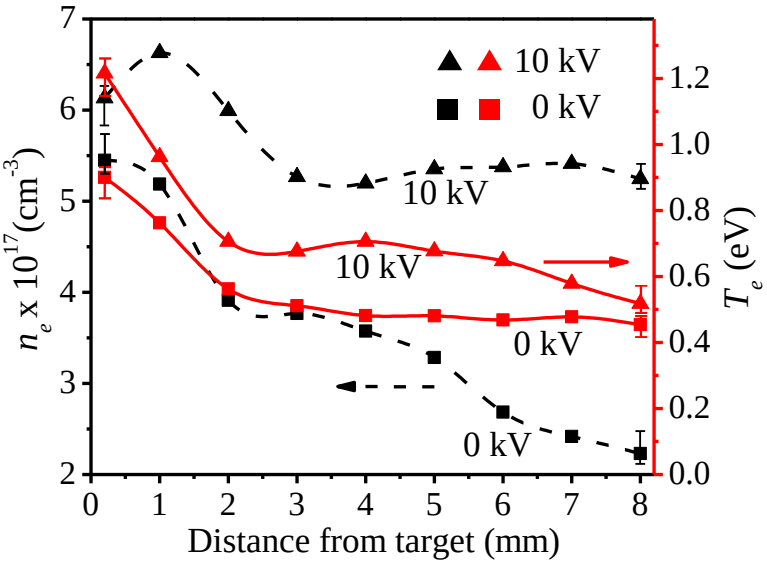

Fig. 4.11 Variation of the electron density ne (dashed line) and excitation temperature *Te* (solid line) along the direction of propagation of the plume for 0 kV (squares) and 10 kV (triangles) spark voltage. The laser intensity is 5×10^9 W/cm^2. Five spectra are averaged with the error bar indicating the range from the five different spectra.

The energy distribution of the electrons in the laser plasma is nearly Maxwellian as the collisional processes dominate over radiative processes [42]. The corresponding minimum n_e for which the plasma can be in LTE is given by the McWhireter criterion as $n_e \geq 1.4 \times 10^{12} . T_e^{1/2} . (\Delta E)^3$, where ΔE is the maximum energy difference between the upper and lower level and T_e is the electron temperature [41]. This criterion is necessary but not sufficient for LTE [44]. For the Al I 308.2 nm emission line, ΔE = 4.02 eV which corresponds to the maximum transition energy from the high energy level E_k to the low energy level E_i. The

maximum value of T_e is measured in our experiment as 1.3 eV and, considering the McWhireter criterion, the lower limit of n_e for the plasma to satisfy the LTE condition is calculated to be 1.12×10^{16} cm^{-3}.

For a plasma satisfying the LTE condition, the electron and ion temperatures are about equal. The discrepancy between the plasma electron temperature T_e evaluated by OES and the effective ion temperature T_i evaluated from the ion TOF signal can be explained by the plasma temperature for the different times and regions probed. The deconvolution of the ion TOF signal indicates that T_i is up to ~50 eV with the spark-discharge. In the core of the plasma plume and at the early stages of its expansion, the plasma temperature and density are at their highest. This is where the MCIs are mainly generated. After the adiabatic expansion, the thermal energy is rapidly converted into kinetic energy, with the plasma attaining high expansion velocities. The ion TOF signal carries information from the initial core of the plasma where both the plasma temperature and density are at their highest values. However, the optical emission from the laser plasma at the initial stage of plasma formation mainly consists of an intense continuum. This continuum radiation occurs due to the combined effects of Bremsstrahlung (free-free transitions) and radiative recombination (free-bound transitions). Bremsstrahlung radiation takes place where free electrons lose kinetic energy as they pass close to ions and can dominate over radiative recombination at the initial part of the laser pulse. However, radiative recombination becomes dominant after a few ns [46]. The line emission (bound-bound) from strong broadened ion lines and weak neutral lines appears a few tens of ns after the laser interacts with the surface. OES is limited by the continuum emission at the initial plasma expansion stage and does not provide information about the initial plasma temperature or density. The OES conducted in the present work is temporally integrated, which contributes to the observed low temperature. The LTE condition requires high plasma density to allow for collisional thermalization of the ions and the electrons. As the plasma expands and its density and temperature are reduced, the plasma parameters deviate from LTE.

4.6 Conclusion

A spark-discharge is coupled to an expanding Al laser plasma produced in a vacuum by a 7 ns Nd:YAG laser with a time delay that can be selected to maximize spark-discharge energy coupling. The spark-discharge effectively amplifies the ion yield and the optical emission line

intensities. The plasma effective ion temperature T_i is obtained from the ion TOF, while the electron temperature T_e is obtained from OES. For a laser intensity of 3.5×10^9 W/cm^2, T_i increases from ~15 to ~50 eV when the laser plasma is coupled to a 2.4 J spark-discharge. The maximum n_e and T_e are recorded with the spark-coupled laser pulse are measured as 6.6×10^{17} cm^{-3} and 1.3 eV, respectively. T_e measured from OES is observed to be significantly lower than T_i obtained from the ion TOF signal, which reflects the temperature of the different spatial and temporal regions probed by each method.

CHAPTER 5

CARBON MULTICHARGED ION GENERATION FROM LASER-ARC ION SOURCE

5.1 Introduction

We report on a laser-arc ion source where the carbon target and a grounded mesh serve as the cathode and anode, respectively. Aluminum multicharged ion generation was reported using a similar experimental setup where the spark-discharge was established between two electrodes positioned in front of the target that the laser ablates [42]. The main drawback of placing external electrodes is that the external electrode electric field reduces the ion acceleration. Also, the coupling between the spark discharge and the laser plasma depends on the shape of external electrodes. In the present laser-spark configuration. the spark-discharge is generated between the target and a mesh placed parallel to the target resulting in a spark in the direction of the plume expansion. This configuration avoids the use of external electrodes and is suitable when the target is a conductor. The time delay between the spark-discharge and the laser pulse is varied to optimize the coupling between the spark-discharge and the laser plasma. The ion generation from laser-arc ion source is compared with the laser ion source with DC electric field in between the target and the mesh. Ion generation of 72 nC with up to C^{6+} charge state is detected when 1.2 J spark-discharge energy is coupled to a ~50 mJ laser pulse.

5.2 Experimental

A schematic of the laser-arc ion source is shown in Fig. 5.1. A Q-switched Nd:YAG laser with pulse width 7 ns, pulse energy ≤ 80 mJ, and pulse intensity ≤ 4.5×10^9 W/cm^2 is used to ablate a 99.99% pure glassy carbon target (0.5 mm thick, 2.5 cm diameter), mounted on 5 cm diameter target holder connected to a vacuum x-y manipulator. A grounded nickel mesh of 10 cm in diameter is mounted parallel to the target surface. The base vacuum pressure is maintained in the high 10^{-9} Torr. The pressure in the vacuum system increases up to the low 10^{-8} Torr range

during laser ablation. A biconvex lens L1 (f = 40 cm) is used to focus the laser beam on the target with the laser beam incident at θ = 45° with the target surface. The laser spot on the target has an area of ~2.5 × 10^{-3} cm^2, as determined by measuring the laser beam width at target-equivalent-plane with the knife-edge method. A DC voltage of 0 – 7 kV is applied to the carbon target using a high-voltage power supply (CPS Inc. 0 – 30 kV, 1 mA). A pulse forming network (PFN) is constructed to generate 0 – 7 kV voltage pulse for the spark-discharge. The PFN consists of 30 high-voltage capacitors (UHV 9 A, 2 nF, 40 kV TKD) mounted on an Al plate and connected with a 1.8-mm thick Cu wire.

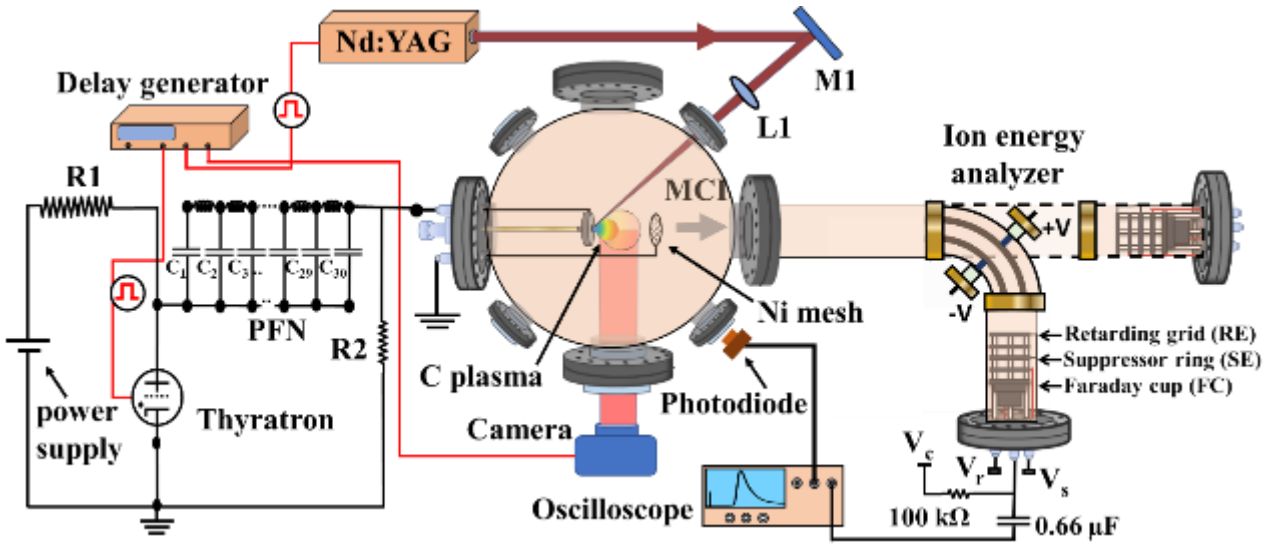

Fig. 5.1 Laser-arc ion source. The pulse forming network (PFN) is triggered by a delay generator at different time delays with respect to the laser pulse. The spark-discharge is coupled to the carbon plasma as the plasma expands between the carbon target

The PFN charging power supply (Glassman, PSLG30R5, 0 – 20 kV) is connected to the current limiting resistor *R1* = 350 kΩ. The PFN is terminated with a 300 Ω load resistor *R2* which is connected in parallel to the spark gap. A digital delay generator (SRS-DG 645) is used to externally trigger the thyratron (L-4945A) and the laser pulse. A digital single-lens reflex camera (DLSR-Canon Rebel T3 EOS 1100D, 12.2-megapixel, 0.25 ms max shutter speed) is used to capture the picture of the plasma plume from an angle of 45° to the plume expansion direction.

The camera is also triggered by the delay generator. The voltage on and current through the target are measured by a high-voltage probe (Tektronix P6015A, rise time 4.5 ns) and a current pick-up coil (Pearson 6595, rise time 2.5 ns), respectively. A Si photodiode (Thorlabs DET10A, spectral range 200 – 1100 nm, rise time 1 ns, active area 0.8 mm^2) is used to trigger the oscilloscope. Ions with a distribution of energy-to-charge *E/z* ratio are selected by an electrostatic ion energy analyzer (EIA) with a radial cylindrical design at a deflection angle of 90°. The range of *E/z* is obtained by the equation $\frac{E}{z} = \frac{eU}{2ln\left(\frac{r_2}{r_1}\right)}$, where *E* is the kinetic energy of the ion, *e* is the electron charge, *U* is the total voltage across the plates, r_1 =14.5 cm is the inner radius, and r_2 =18.2 cm is the outer radius. The length and inner diameter of the ion transport line are 154 cm and 10 cm, respectively. The ions are detected at the end of the ion transport line by a Faraday cup (FC) mounted with a suppressor ring electrode (SE) that is used to suppress the effect of secondary electron emission from ion bombardment of the FC. A three-mesh retarding field ion analyzer (RE) is placed before the SE. The SE and FC are biased at −120 and −80 V, respectively. The RE is used to measure the ion energy distribution. The two-outer meshes of RE are grounded while the central mesh is connected to a variable voltage supply V_r. An oscilloscope (Tektronix DPO 3034) is used to record the time-of-flight (TOF) of the carbon ions through a 0.66 µF coupling capacitor. The data is averaged for 30 laser pulses to average-out any pulse-to-pulse fluctuations in TOF. A new target surface is exposed to the laser spot after 30 consecutive pulses in order to avoid the formation of deep craters. For a new surface spot, the first few laser pulses are disregarded to remove any possible contamination on the target surface. We noted that when the laser pulses repeatedly hit the same target spot, the total number of detected ions is decreased by ~6% at the 100^{th} laser pulse compared to the first laser pulse at 3×10^9 W/cm^2 pulse intensity. The laser intensity is approximated on the target surface considering 10% energy loss in the viewport.

5.3 Result and discussion

5.3.1 Voltage and current

The ions emitted from the laser plasma are accelerated by the electric field that is applied between the target and the mesh. The voltages on the target for different laser intensities are

shown in Fig. 5.2(a). An ~90% drop in the voltage is observed after ~4 and ~2 μs at a laser intensity of 3.0 × 10^9 and 4.5 × 10^9 W/cm^2, respectively. The voltage drop occurs when the plasma plume connects the target to the mesh allowing the arc to occur. The current through the target is shown in Fig. 5.2(b). The maximum current through the target is 1.48 A for 5 kV target voltage and 0.3 A for 1 kV target voltage at a laser intensity I = 3.0 × 10^9 W/cm^2. The maximum current increases up to 6 A for 7 kV target voltage for I = 4.5 × 10^9 W/cm^2.

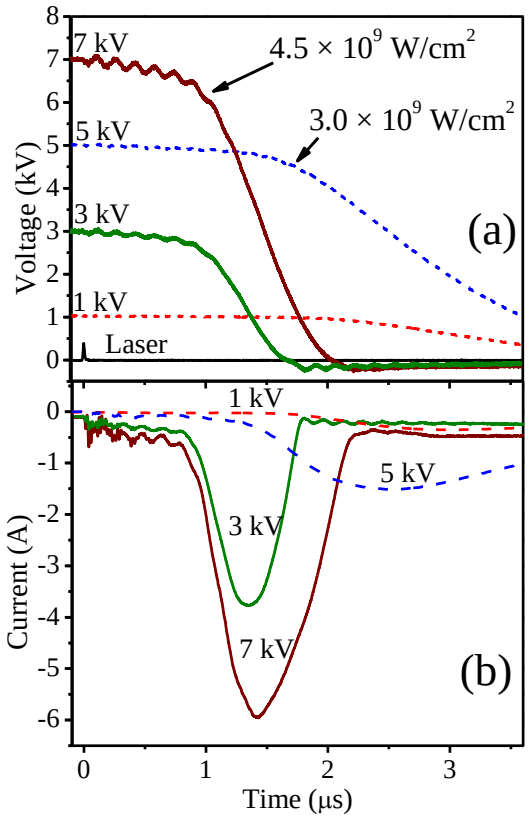

Fig. 5.2 Voltage on the target and (b) current through the target when the target voltage is varied from 1 to 7 kV. The photodiode signal of the laser pulse indicates the laser triggering. The laser pulse intensities are set as 3.0 × 10^9 (dash line) and 4.5 × 10^9 W/cm2 (solid line), respectively in both (a) and (b).

The spark-discharge voltage and current are measured for different time delays t_d between the thyratron and the Q-switch trigger pulse provided by the delay generator. For the laser-arc experimental setup, the laser pulse hits the C target early compared to the electric pulse when the thyratron and the laser Q-switch are triggered at the same time. As a result, the

thyratron is triggered ~210 μs before the triggering of the Q-switch of Nd:YAG laser to overlap the laser pulse and the high voltage electric pulse. The length of each BNC cable is kept less than 3 m to avoid delay on rise time. The signal rise times of the photodiode, voltage probe, and current probe are in the order of a few ns, as provided by the manufacturer, which is adequate for our experiment. The time delay t_d is varied from 0 to 1.6 μs for a laser intensity of 3.0×10^9 W/cm^2. For $t_d < 0.8$ μs, the spark-discharge is not ignited. A significant rise in current across the target is recorded for 0.8 μs < t_d < 1.2 μs, which results from the spark-discharge between the target and the mesh. Over that range of t_d, the peak arc current decreases gradually with time delay. At $t_d > 1.6$ μs, the voltage drop across *R2* is similar to that for $t_d < 0.8$ μs, which indicates the absence of the arc between the target and mesh through the plasma plume. For $I < 1.0 \times 10^9$ W/cm^2, the spark-discharge did not occur for all t_d, as the laser plasma is not dense enough to initiate the spark-discharge.

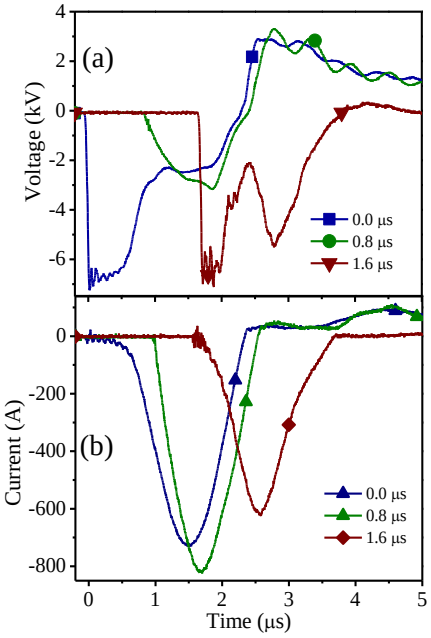

Fig. 5.3 (a) Voltage on and (b) current through the target. The grounded mesh is placed 10 cm in front of the target. The time delay between the laser pulse and PFN trigger is varied from 0 to 1.6 μs for 7 kV PFN charging voltage at 3.0×10^9 W/cm^2 laser intensity

5.3.2 Ion Time-of-flight

The ion velocity generated from a laser plasma has three main components: plume ablation velocity, ion thermal velocity, and ion velocity gain by the double-layer potential at the plume-vacuum interface [80]. The double-layer potential is established due to the emission of fast electrons, at the early stages of plume expansion, leaving a space-charge region in the front of the expanding plume. The energy that the ions gain in the double-layer potential is proportional to their charge state. The ions can be further accelerated by an external electric field. We refer to the ions that are accelerated by the external electric field as fast ions q_{fast}, while the ions that are not accelerated by the external electric field are referred to as slow ions q_{slow}. Both fast and slow ions are accelerated by the double-layer potential. Fast ion peaks are detected early in the TOF signal. For our target-mesh configuration and laser fluence of 3.0×10^9 W/cm^2 with laser plasma coupled to 1.2 J spark-discharge energy, only ~10% of the total detected ions are fast ions. Fig. 5.4 shows the TOF of slow ions for spark-discharge energy of 0 – 1.2 J coupled to the laser plasma, which corresponds to charging the PFN to 0 – 7 kV. The total ion charge $Q = \int I(t)dt$, where *I(t)* is ion current measured from the FC. The TOF shows that the number of slow ions increases from ~12 to ~72 nC when the energy of the spark-discharge is gradually increased from 0 to 1.2 J. The ion TOF peak is also shifted from 19 to 25 μs which indicates the broadening of the ion energy distribution with higher spark-discharge energy. The TOF of the slow ions generated when the DC voltage is applied to the target is also measured. The total charge of the slow ions detected is ~7 nC when 3 kV DC voltage is applied on the target for 3.0×10^9 W/cm^2 laser intesity. The total ion charge detected by the FC for 3 kV external electric field applied to the target is significantly less than for no voltage applied to the target (power supply voltage 0 kV), as shown in Fig. 5.4 (dotted line). The result can be explained by the divergence of the ions emitted by the laser plasma as a result of the distortion of the extraction field due to the presence of the expanding plasma in the target-grid region. This field distortion causes the ion beam to diverge strongly before moving into the drift tube, which is intensified by the thermal kinetic energy of the ions whose velocity vectors are not parallel to the drift tube [81].

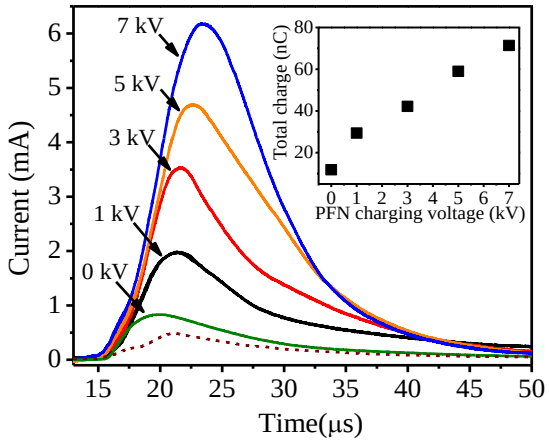

Fig. 5.4 Time-of-flight of slow ions (q_{slow}) ions for different PFN charging voltages. A delay time t_d = 0.9 μs is set between the laser pulse and the spark-discharge. The inset shows that relationship between the total charge and PFN charging voltage. The dotted line is the TOF signal when 3 kV DC accelerating voltage is applied to the target. The laser pulse intensity is fixed at 3.0 × 10^9 W/cm^2.

The three-mesh retarding field analyzer is used to observe the ion energy distribution. The retarding voltage blocks ions with kinetic energy less than zeV_0, where z is the ion charge state, V_0 is the retarding voltage applied to the central electrode of energy analyzer, and e is the unit charge in Coulomb. The ions with higher energy than zeV_0 lose some of their energy as they drift towards the retardation mesh; however, they are accelerated back to their initial energy between the central and final mesh of the three-mesh retarding field ion analyzer before being detected by the FC. The retardation of slow ions generated by ~0.6 J spark-discharge energy coupled to plasma generated by 3.0 × 10^9 W/cm^2 laser pulse is shown in Fig. 5.5(a). The inset of Fig. 5.5(a) shows that the number of ions decreases from 45 to 2 nC when the retarding voltage increases from 0 to 250 V. Fig. 5.5(b) shows the retardation of the carbon ions generated by laser plasma alone with I = 3.0 × 10^9 W/cm^2. A retarding voltage of ~250 V is enough to retard more than 95% of the ions. The results show that the spark-discharge increases the ion-yield, as well as ion energy, compared to the slow ions generated for the laser pulse only (0 kV on target).

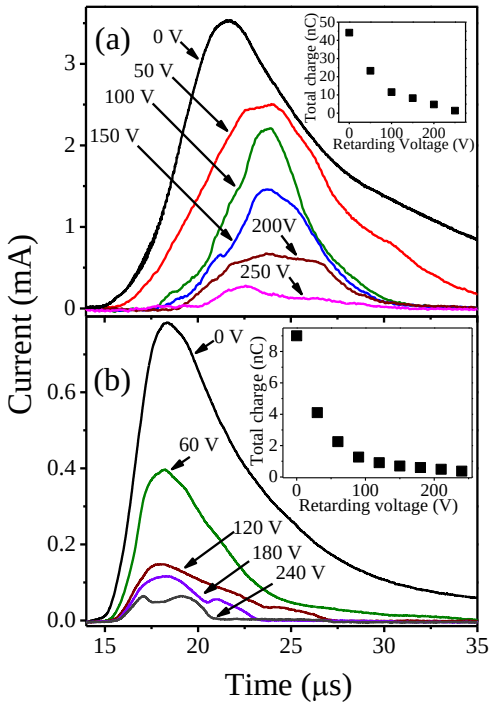

Fig. 5.5 (a) The retardation of q_{slow}, generated by ~0.6 J spark-discharge coupled to laser plasma (3 kV PFN charging voltage). The inset shows the total number of q_{slow} with respect to retarding voltage. (b) The retardation of q_{slow}, generated by the laser pulse.

The ion generation from a laser-arc source starts by the laser pulse ablating the target to produce laser plasma. Then, the ablated plume expands connecting the target to the grid region while the arc is triggered to enhance the plasma temperature and density producing more MCIs. The cathode spots on the target created by the spark-discharge can also act as an ion source. During the spark-discharge, the arc current is concentrated at a small number of cathode spots. The spot is formed by an explosive emission process. The lifetime of a cathode spot can be in the range of 10 ns to 1μs as previously reported [82, 83]. The plasma pressure within a cathode spot is high, and the strong pressure gradient causes the plasma to move forward from the target surface in a similar way to the plasma plume generated by the focused laser beam at a solid surface. As a result, ions are generated with higher ion energy and temperature for the laser-arc compared to the laser pulse alone. Fig. 5.5(a) shows a broader ion energy distribution and higher ion yield for the spark-discharge compared to Fig. 5.5(b) which shows ions generated by the laser pulse alone. The spark discharge causes an increase in the plasma temperature and density [28].

An external DC voltage V_{ext} is applied between the target and the mesh to accelerate the ions. This electric field produces substantially more kinetic energy in the fast component of the ions q_{fast} than their thermal kinetic energy q_{slow}. This ensures that the flight time in the drift tube is mainly due to electric field acceleration, which is charge-dependent. The Debye shielding of the plume usually limits the efficiency of extraction and, therefore, the ions acquire final kinetic energy lower than $Z_i.eV_{ext}$, where Z_i is the ion charge and V_{ext} the extraction voltage. The fast ions are accelerated in the electric field, and the retrograde motion of the plasma edge exposes more ions to the external electric field and repels electrons [84, 85]. The total number of ions reaching the FC is calculated from the TOF signal for a straight drift tube, whereas, the electrostatic ion energy analyzer (EIA) is used for selecting ions with a range of energy-to-charge *E/z* ratio. The ion yield of the q_{fast} is increased by a factor of ~4 when the target voltage is increased from 3 to 7 kV, as shown in Fig. 5.6(a). The charge states of the fast ions are identified with the help of the EIA as they are well-separated in time, as shown in Fig. 5.6(b). A slit with a narrow opening at the entrance and exit of EIA can provide higher resolution in *E/z* selection. However, the EIA is operated without a slit in order to maximize the ion transmission. The resolution of EIA ($\Delta E/E$) is calculated as ~10%. Fig. 5.6(b) shows the TOF signal detected for different *E/z* ratios as selected by the voltage applied to the EIA. The value of *E/z* is set to maximize the ion signal for each accelerating voltage on the target. The maximum ion yield is obtained for *E/z* set at 1.8, 3.2, and 4.3 keV for DC voltages of 3, 5, and 7 kV applied to the target. Up to C^{3+} is detected for 3 kV ion accelerating voltage, whereas a C^{4+} peak is detected for 7 kV DC voltage on the target.

A significant increase in ion detection and charge states is observed for the laser-arc configuration, as shown in Fig. 5.6(c). The number of fast ions increases from 0.12 to 3.5 nC, when the spark-discharge energy is increased from 0.6 to 1.2 J (3 – 7 kV on the PFN). In Fig. 5.6(d), the ion TOF signal is shown for the *E/z* ratio centered at 1.3 keV. C^{5+} and C^{6+} ions are detected when 1.2 J spark-discharge energy is coupled to the laser plasma for a laser intensity $I = 3.0 \times 10^9$ W/cm^2. The time delay t_d between the laser pulse and the spark-discharge is varied. A consistent spark-discharge is observed at $t_d > 0.8$ µs and up to C^{6+} is recorded at $t_d = 0.9$ µs. C^{6+} and C^{5+} are not identified for $t_d > 0.9$ µs, as the higher charge state ions are in the front of the plume and pass the mesh without amplification.

The cross-sections for the interaction of different MCIs, ranging from H^+ to Ca^{20+}, with hydrogen gas were previously measured [86]. Considering an MCI with 100 eV per unit charge,

the mean free path of the MCI is orders of magnitude longer than our experimental drift tube length. Therefore, the ion charge remains almost unchanged in the drift tube.

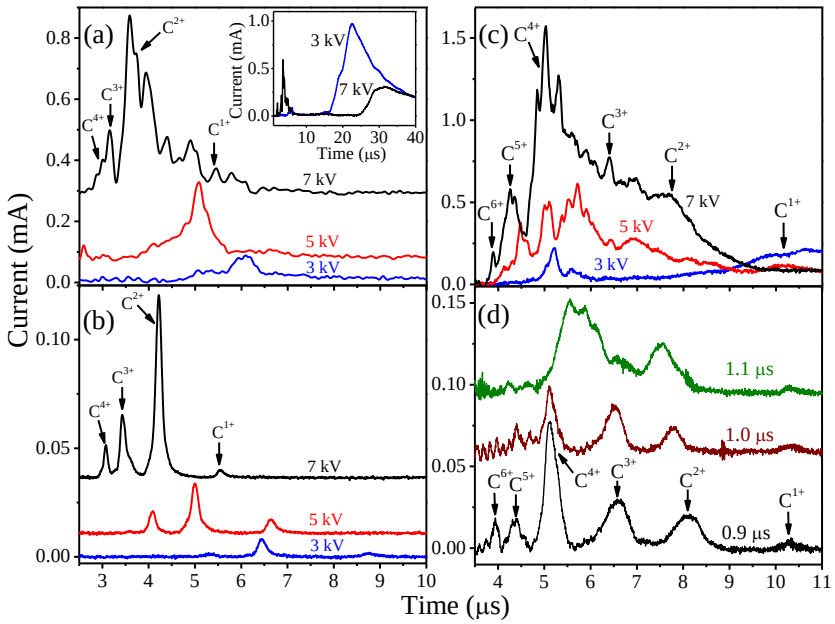

Fig. 5.6 Time-of-flight signal (TOF) of fast carbon ions detected using the straight drift tube. Up to C^{4+} is generated for 7 kV DC voltage applied to the target. The inset shows the TOF of slow and fast ions for 7 and 3 kV on target (b) Ions with different charg

We used a digital camera to record the enhancement of optical emission from the laser-arc plasma plume from that with the laser alone. The camera is triggered by the delay generator at a fixed delay of 1.5 ms from the laser pulse. The plume size increases when the DC and pulsed voltage is applied to the target. The time delay t_d is fixed at 0.9 μs between the laser pulse and spark-discharge. Fig. 5.7(a) shows a bright plasma core at the point of interaction of the laser beam and the target surface. The plasma core length is ~0.5 cm for 4.5×10^9 W/cm^2 laser intensity. Fig. 5.7(b) shows that the plasma core is extended up to ~1 cm when 7 kV DC voltage is applied to the target. Further enhancement of the C plasma plume is observed in Fig. 5.7(c) when a pulsed voltage is applied to the target. We also noticed the generation of macro-particles from the C plasma when spark discharge is initiated. Carbon macro-particles are an incandescently glowing species that were previously reported for carbon target ablation by a laser intensity of 5×10^{10} W/cm^2 [87]. The generation of macro-particles is also well known in

vacuum-arc deposition [88]. Some macro-particles appear much brighter than others. The brightness changes due to the different speed of individual macro-particles; a slow macro-particle produces a more intense exposure to the camera detector than the fast particle [89].

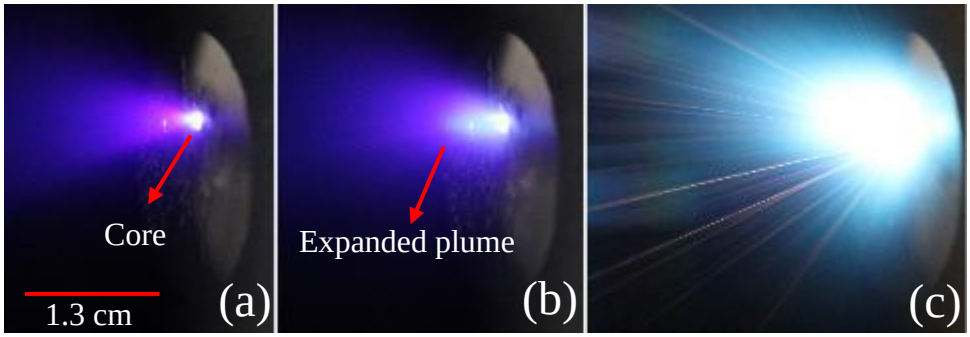

Fig. 5.7 (a) The image of C plasma captured by a digital camera for laser pulse alone, (b) for 7 kV DC voltage on target, and (c) for 1.2 J spark-discharge energy coupled with a laser plasma. Laser pulse intensity is fixed at 3.0×10^9 W/cm^2.

The camera is triggered by applying a reset pulse (+5 V) from the delay generator. The time delay of the camera exposure and spark-discharge triggering is estimated to be 1.5 ms. 20 images are taken for a similar time delay to ensure the repeatability. A similar experimental setup was used in a previous report [90].

5.4 Conclusion

A carbon ion with a charge up to C^{6+} is generated by 1.2 J spark-coupled to carbon plasma generated by 80 mJ laser pulse ablation of a C target, whereas up to C^{4+} is detected with a DC voltage applied to the target for similar conditions. A time delay between the spark-discharge and the laser pulse of ~0.9 µs maximizes the generated charge and charge state. This geometry of coupling the spark discharge energy to the expanding plasma plume with the electric field along the direction of plume expansion enhances the total ion generation and reduces the complexity of the laser-spark discharge for ion generation.

CHAPTER 6

NANOSCALE HEAT TRANSFER MEASUREMENT BY FEMTOSECOND PUMP-PROBE SPECTROSCOPY

6.1 Introduction

Ultrafast laser spectroscopy is a very effective technique for studying the non-equilibrium electron dynamics in the solid. Experimental investigations of non-equilibrium electron dynamics are demonstrated by several techniques such as ultrafast time-resolved thermomodulation reflectivity/transmissivity (TTR) [91, 92], surface-plasmon polariton resonance (SPP) [93, 94], time-resolved two-photon photoemission (TPPE) [95, 96], and single-photon photoemission [97]. A simple experimental setup known as the pump-probe technique is used in these experiments. In the pump-probe technique, a high-intensity pump beam is used to heat up the target surface, while the low-intensity probe beam is used to measure the induced changes in the target surface. Thermomodulation experiments in metals rely on the use of an ultrashort pulse to perturb the hot electrons and then probe the changes in the optical properties of the metal with a delayed probe pulse.

The heat transfer mechanism in the micro and nanoscale is of much interest to the development of nanoscale devices and to probe surface phenomena [98-103]. The thermal conductivity measurement techniques can be divided into steady-state and transient methods. The steady-state method measures the thermal properties by creating a time-independent temperature difference, whereas the transient method measures the time-dependent heat dissipation process of a sample. The appropriate method to use for thermal conductivity measurement depends on the material's thermal properties, sample configuration, and measurement temperature. The most commonly used thin films thermal conductivity measurement techniques are the steady-state methods, the 3ω method (periodical heating), and the transient thermoreflectance technique in both time-domain (TDTR) and frequency-domain (FDTR) [104].

The femtosecond transient thermoreflectance technique was widely applied to observe the transient changes in reflectance. In this technique, a femtosecond laser pulse is split into a heating pulse and a weaker probe pulse. The heating pulse is used to generate transient heating while the probe pulse detects changes in the optical properties of the sample. A variable time delay between the pump and probe pulses is produced by a translation stage. The probe then takes a snapshot of the sample reflectance or transmittance at a specific experimental time delay relative to the pump, where the temporal resolution of the snapshot is on the order of the probe pulse duration. Transient thermomodulation measurement was conducted on Cu films using 8 ps laser pulses [91]. Subsequently, sub-picosecond lasers were used to resolve nonequilibrium heating in Au and Cu [92, 105]. Electron–phonon coupling in various metals was subsequently studied [106]. The effect of film grain structure on electron–phonon coupling and electron transport in Au was studied by performing transient thermomodulation experiments on single-crystalline and polycrystalline Au films [107]. Alfano *et al.* reported on the investigation of electron-phonon relaxation in Nb by femtosecond pump-probe experiment [108-110]. Most of the early investigations were performed on thin films in order to isolate the effect of electron–phonon relaxation on the thermomodulation signal from signal due to carrier transport. Paddock and Eesley used transient thermoreflectance to measure thermal conductivity [111]. Several investigators have recently revisited this idea since the thermal properties of thin films have become a topic of great interest to the microelectronics industry [112].

6.2 Pump–probe technique in different experiments

Thermal conductivity and interfacial thermal conductance play crucial roles in the design of engineering systems where temperature and thermal stress are of concern. A variety of measurement techniques are available for both bulk and thin film solid-state materials with a broad temperature range. For thermal characterization of bulk material, the steady-state method, transient hot-wire method, laser flash diffusivity method, and transient plane source method are mostly used. For thin film measurement, the 3ω method and the transient thermoreflectance technique including both time-domain and frequency-domain analysis are widely employed. Modulated photothermal techniques have been used to measure the thermal conductivity over the past few years. In these techniques, heating from a modulated optical source causes an

oscillatory temperature field on the sample surface that is measured by phase sensitive detection instrumentation. David *et al.* used modulated thermoreflectance microscopy to study thermal conductivity degradation in irradiated ceramic materials [113]. Jensen *et al.* used lock-in infrared thermography and photothermal radiometry to study the effect of proton irradiation on ZrC [114]. More recently, Khafizov *et al.* used a double color laser based modulated thermoreflectance method without a metal coating to report on the thermal conductivity of proton irradiated silicon [115].

6.3 Experimental setup

An optical pump-probe setup is used to observe the time domain thermoreflectance signal of Nb thin films. A femtosecond Ti:sapphire laser, wavelength λ = 800 nm is used to produce laser pulses with pulse width τ ~100 fs (full width at half-maximum) as measured by a second harmonic generation crystal at a repetition rate of 80 MHz. The laser beam is split into pump and probe beams by a nonpolarizing beam splitter with an intensity ratio of 9:1. The pump pulse with the energy of ~0.15 nJ/pulse is used to heat the sample. An acousto-optic modulator (IntraAction AOM-402AF3) is used to modulate the pump beam at a maximum modulation frequency of 1 MHz. A half-wave $\lambda/2$ plate is used to rotate the polarization of the pump beam, generating P or S-polarized beam. The pump beam passes through a set of two mirrors mounted on a linear stage (Newport FC100), which is used to change the optical path between the pump and probe pulses. The minimum step size of the linear stage corresponds to a 6.67 fs time delay between the pump and the probe pulses. A schematic of the experimental setup is shown in Fig. 6.1.

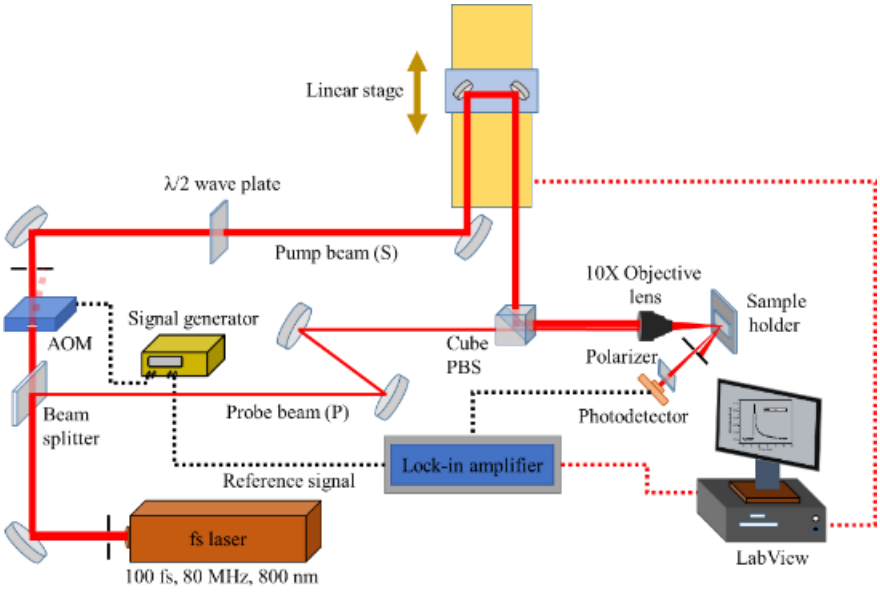

Fig. 6.1 Femtosecond time-domain thermoreflectance pump-probe setup. An acousto-optic modulator is used to modulate the pump beam at 1 MHz. The linear translational stage is used to create the time delay between the pump and the probe pulses.

A 10× objective lens is used to focus the pump and the probe beams on the surface of the sample to diameters of ~5 and ~20 µm, respectively. The size of the pump beam is kept larger than the probe beam to ensure that the probe beam remains entirely within the heated region. The reflected probe beam is detected by the Si photodiode detector (Thorlabs, DET 10A). A polarizer is positioned before the detector to block the scattered S polarized pump light. A lock-in amplifier (Stanford Research Systems, SR865A) is used to detect the transient signal at the reference frequency of the AOM. A LabView program is used to record the transient signal (ΔR) and control the linear stage. The transient signal (ΔR) is divided by the static DC signal from the photodetector *(R)* in the absence of the pump beam to determine $\Delta R/R$. This process eliminates any dependence of the final signal on the probe intensity or the size of the pinhole in front of the photodiode. A photo of the femtosecond pump-probe setup at the ODU Applied Research Lab is shown in Fig. 6.2.

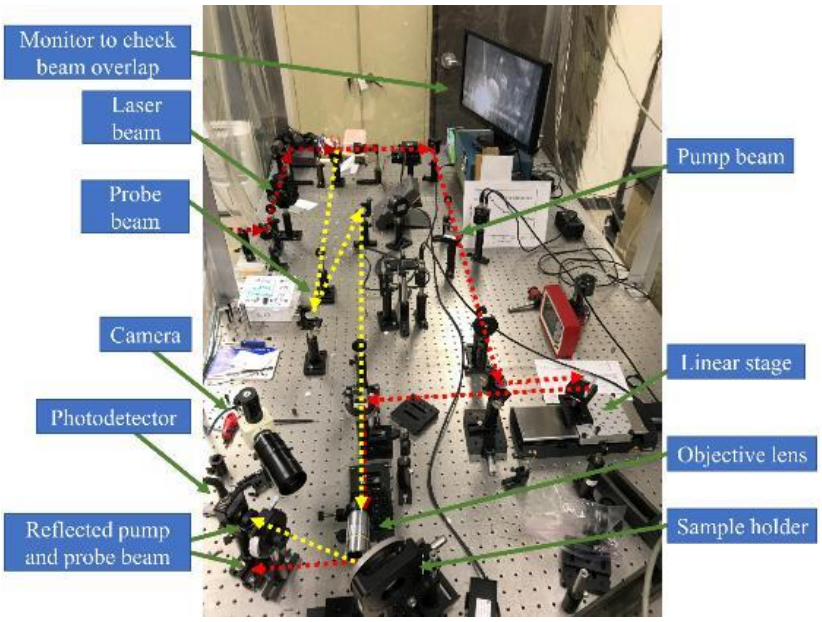

Fig. 6.2 Femtosecond pump-probe setup.

6.3.1 Acousto – optic modulator (AOM)

The AOM is operated in the Bragg mode, where the maximum diffraction efficiency occurs when the incident laser beam and the first-order diffraction beam are adjusted to form symmetrical angles with respect to the acoustic wave fronts shown in Fig. 6.3. Up to 90% of the incident light can be diffracted into 1^{st} order. Since acousto-optic devices are not 100% efficient, all the light cannot be removed from 0 to 1^{st} order [116]. No light remains in the 1^{st} order when the sound power is removed. The 1^{st} order diffraction is most commonly used in applications such as amplitude modulation. Fig. 6.4 shows the modulated pump beam photodiode signal. The modulation frequency is selected as 600 kHz.

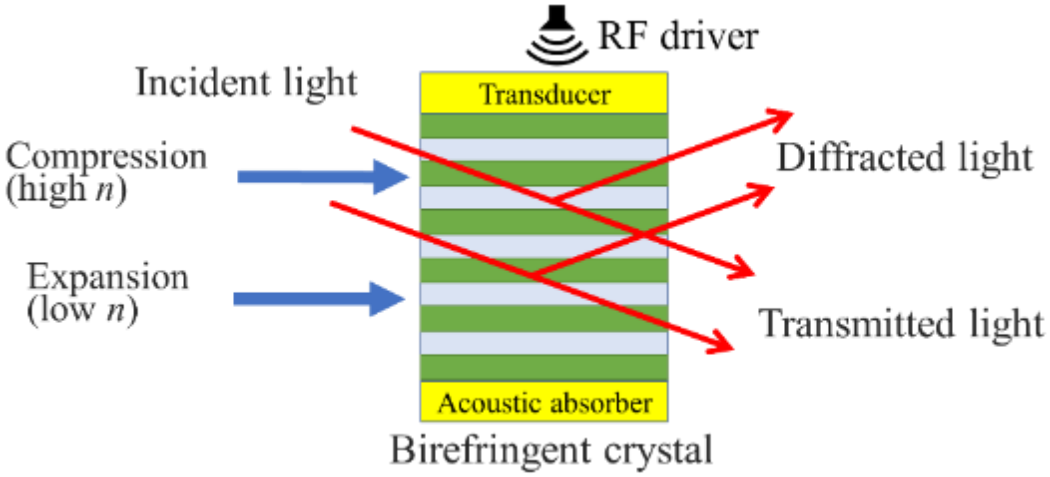

Fig. 6.3 Schematic diagram of acousto-optic modulator. Reconstructrd after ref [116].

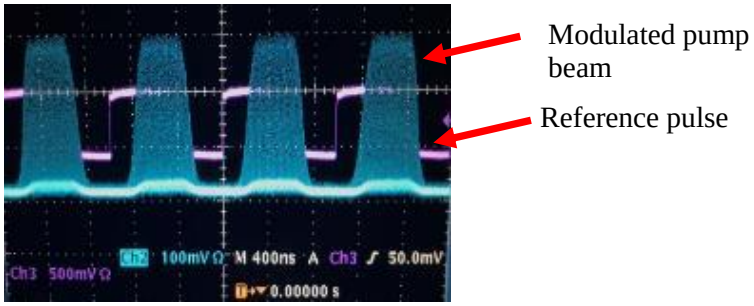

Fig. 6.4 The modulation of the pump beam using acousto-optic modulator. The modulation frequency is 600 kHz.

6.3.2 Lock-in-amplifier

The change in thermoreflectance of the probe pulses due to the interaction with the modulated pump beam is detected using a lock-in amplifier. The heating pulses, schematically shown in Fig. 6.6(a), are incident on the surface of the sample and create a temperature rise with each pulse. The period where there are no heating pulses results in a relaxation back to the initial temperature. It is important that the sample cools before the next pulse arrives to ensure that the sample does not continually heat up to a high base temperature. The corresponding change in reflectivity of the sample is schematically shown in Fig. 6.7(c). As the reflectivity of the metal surface is proportional to the imaginary part of dielectric constant, which is linearly dependent

on temperature, the reflectivity will have the same shape as the temperature profile. Fig. 6.7(b) shows the probe beam intensity before reflecting off the sample. After reflection, the probe beam intensity is modulated according to the temperature of the sample surface as depicted in Fig. 6.7(c).

The photocurrent generated by the photodiode is passed through a band-pass filter that selects only the generated thermoreflectance signal in a narrow band around 1 MHz. The lock-in amplifier takes the Fourier transform of this wave and reports the magnitude of the wave as a voltage typically on the order of 50 to 100 pico-volt. The temporal cooling curve is constructed by moving the stage a small amount and measuring the magnitude of the sine wave at that point. When the probe pulse arrives at the sample surface after the pump pulse, the resulting reflectivity change corresponds to the sample after the deposition of energy and during the cooling process.

6.4 Thermomodulation study of Al thin film on Si by PLD

The pulsed laser deposition is used to generate Al thin film on Si substrate. The thermomodulation data is measured during the film growth. Fig. 6.5 shows the $\Delta R/R$ during the film growth. A 20-60 mJ laser nanosecond laser pulse at 5 Hz repetition rate is used to ablate a 99.999% pure Al foil. The continuous thermomodulation data is collected from the thin film.

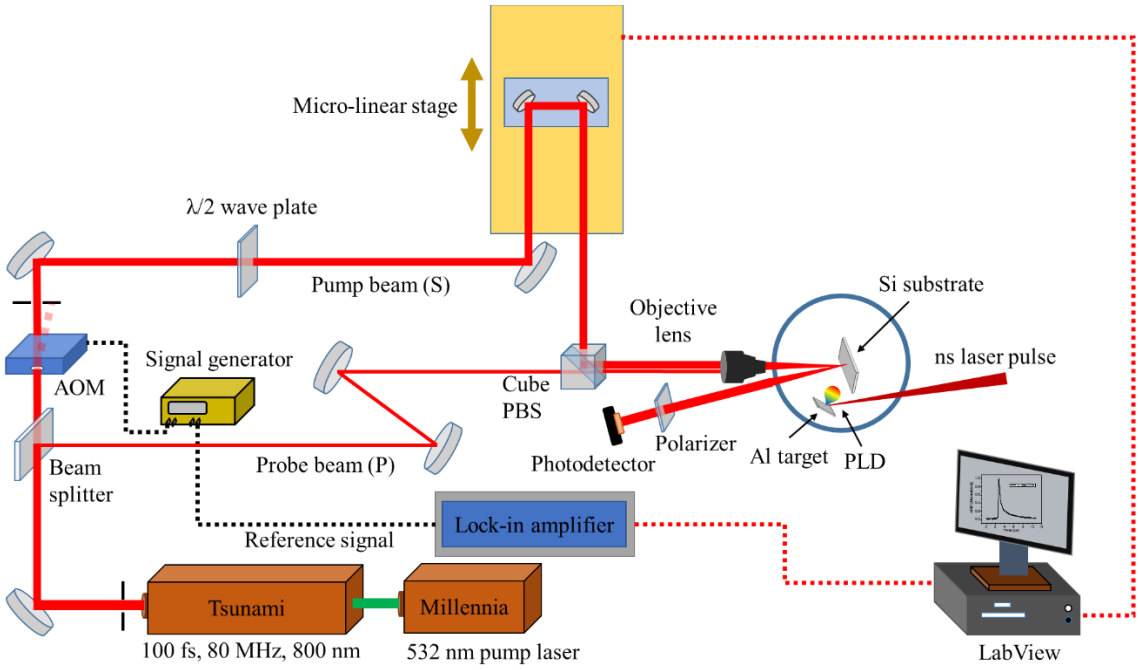

Fig. 6.5 Femtosecond time-domain thermoreflectance pump-probe setup. Nanosecond Nd:YAG laser pulse is used to deposition Al thin-film on Si substrate. Thermoreflectivity of Al film is measured with respect to deposition time.

Fig 6.6 shows the thermomodulation signal from the Al on the Si substrate. The Al is deposited up to 40 minutes with laser pulse intensity ~ 2×10^{9} W/cm^{2} on the target surface considering the ~10% energy loss in kodial glass viewport. The laser is hitting the target at a 45° angle normal to the target surface. The laser spot on the target is measured as ~2.5×10^{-3} cm^{2}. Up to Al^{3+} ion generation was reported for a similar laser intensity. Fig. 6.6 (a) shows the $\Delta R/R$ measurement during the Al deposition. The Al film is deposited for 20 min. The heat diffusion equation is fitted with the exponential data to calculate the thermal conductivity of the Al film. The thermal conductivity increases from 200 W/mK to 270 W/mK when the Al film thickness increased from ~20 nm to ~100 nm, respectively shown in Fig. 6.6 (b). The initial fast response for Al thin film is also measured for different thermal conductivity shown in Fig. 6.6 (c). The two-temperature model is used to fit the thermomodulation data up to 10 ps. The electron-phonon coupling coefficient and heat capacity of Al is collected from [117]. The thermal conductivity is varied from 200 to 300 W/mK to observe the change in thermoreflectivity. The initial decay from the peak due to electron phonon-coupling shows a very small dependence on thermal conductivity

and the experimental result closely follows the heat diffusion model. The rise time of our experimental data is a few picoseconds.

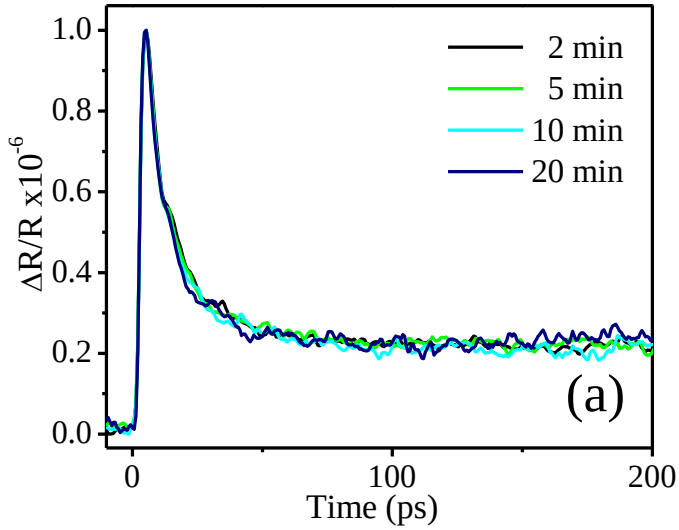

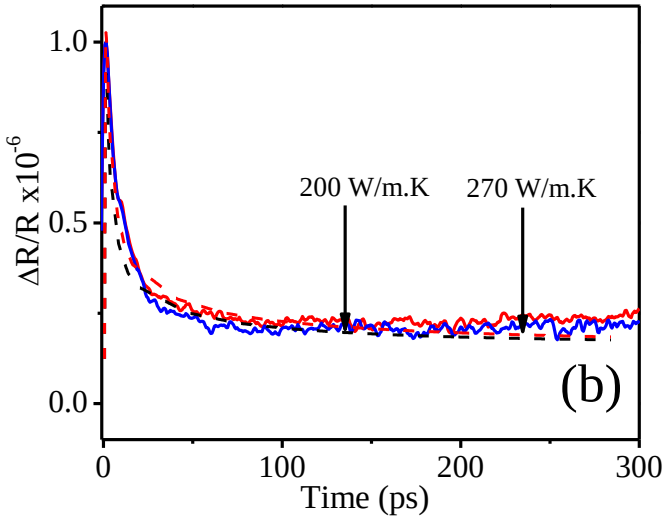

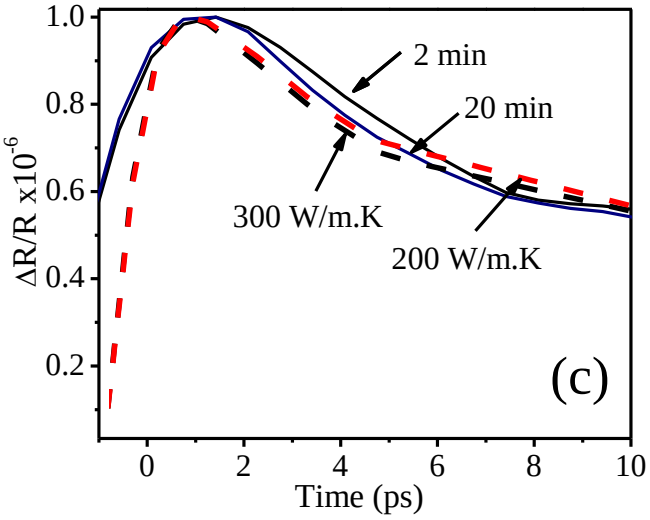

Fig. 6.6 (a) *In-situ ΔR/R* is measured during pulsed laser deposition of Al film on Si substrate. ~ 2×10^9 W/cm^2 laser intensity and 5 Hz repetition rate are used for pulsed laser deposition. (b) The thermal conductivity is measured between 200 to 270 W/mK for response time up to 300 ps. (b) The initial thermomodulation response is fitted with two temperature model which also agree with the thermal conductance in range of 200 to 300 W/mK. The two temperature model parameters are collected from ref. [117]

The cross-section SEM image of the Al/Si is taken to measure the film thickness. The SEM image shows film with big Al clusters due to the pulse laser deposition. A continuous substrate rotation and low power laser pulse deposition is an important factor to avoid the particle cluster. The film thickness is measured as ~ 50 nm.

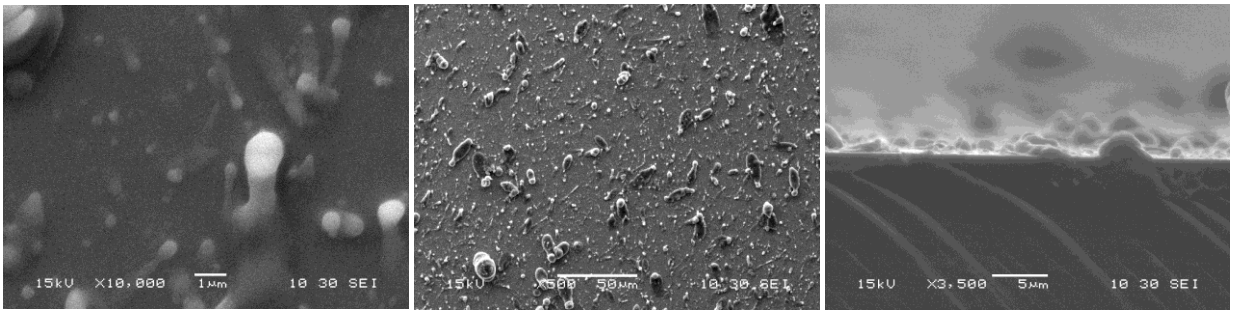

Fig. 6.7 SEM image of Al on Si deposited by the pulse laser deposition. Nd:YAG laser pulse intensity ~ 2×10^9 W/cm^2 at 5 Hz repetition rate is used. The film thickness of approximately 100 nm is detected from the cross-section image.

The laser pulse intensity is increased to ~ 5×10^9 W/cm. 5 Hz pulse repetition rate is used for Al deposition for maximum 90 min. Fig. 6.9 (a) and (b) show the change in the thermal conductivity for different deposition time. The thermal conductivity is increased from 200 to 300 W/mK when the deposition time is increased from 30 to 90 min deposition. Fig. 6.9 (b) shows the initial change in the thermomodulation signal. The two-temperature model is used to fit the electron-phono coupling. The parameters used for the fitting are acquired from [117].

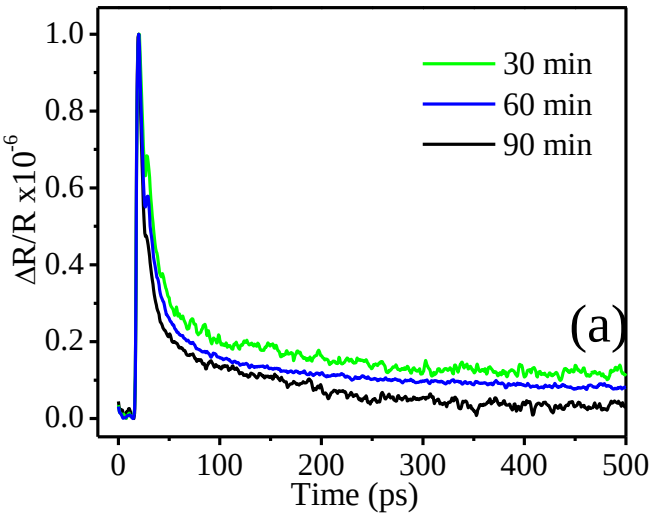

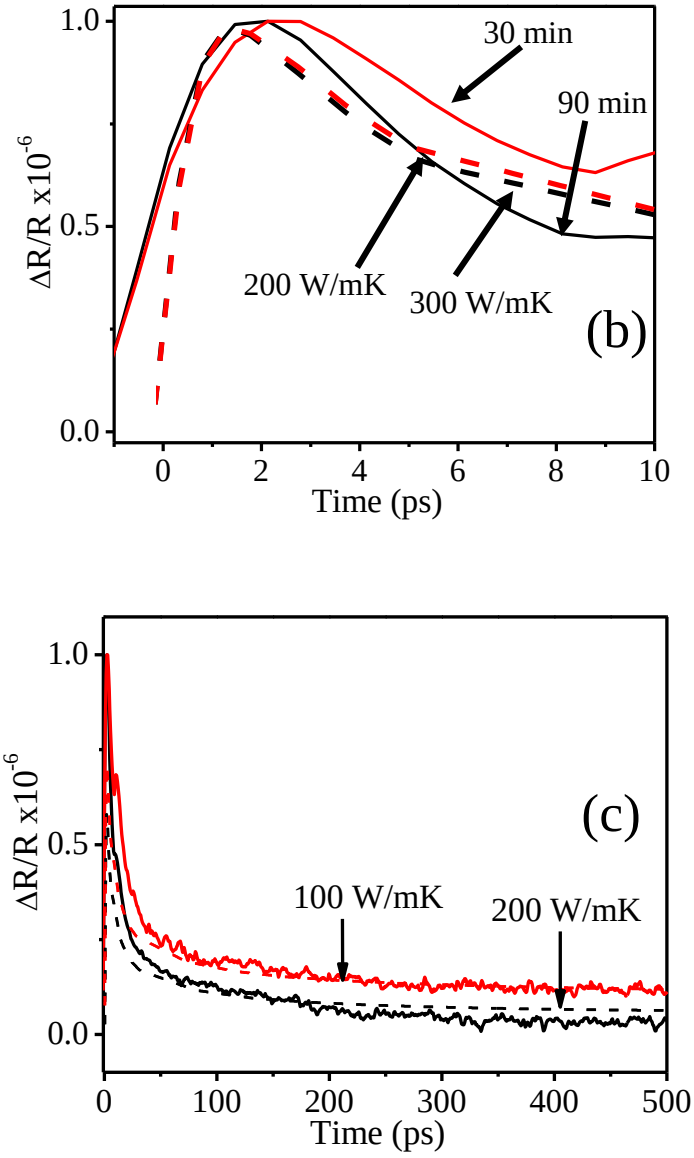

Fig. 6.8 In-situ *ΔR/R* response measurement of Al on Si with ~ 2×10^9 W/cm^2 laser intensity and 5 Hz repetition rate are used for pulsed laser deposition pulsed laser deposition is used. Laser parameters: 40 mJ, ns laser pulse, 5 Hz repetition rate

The amount of Al clusters are increased which is confirmed by the SEM image. From the cross-section SEM image, the film thickness is measured as ~200 µm for 90 min Al deposition. The shift in the initial fast response with increasing film thickness can be related to the defect and the film topography. The increase in the laser energy adds a significant number of defects to the

thin-film. The defect and morphology of the thin film has a significant effect on the thermoreflectance signal that was previously reported [118-120].

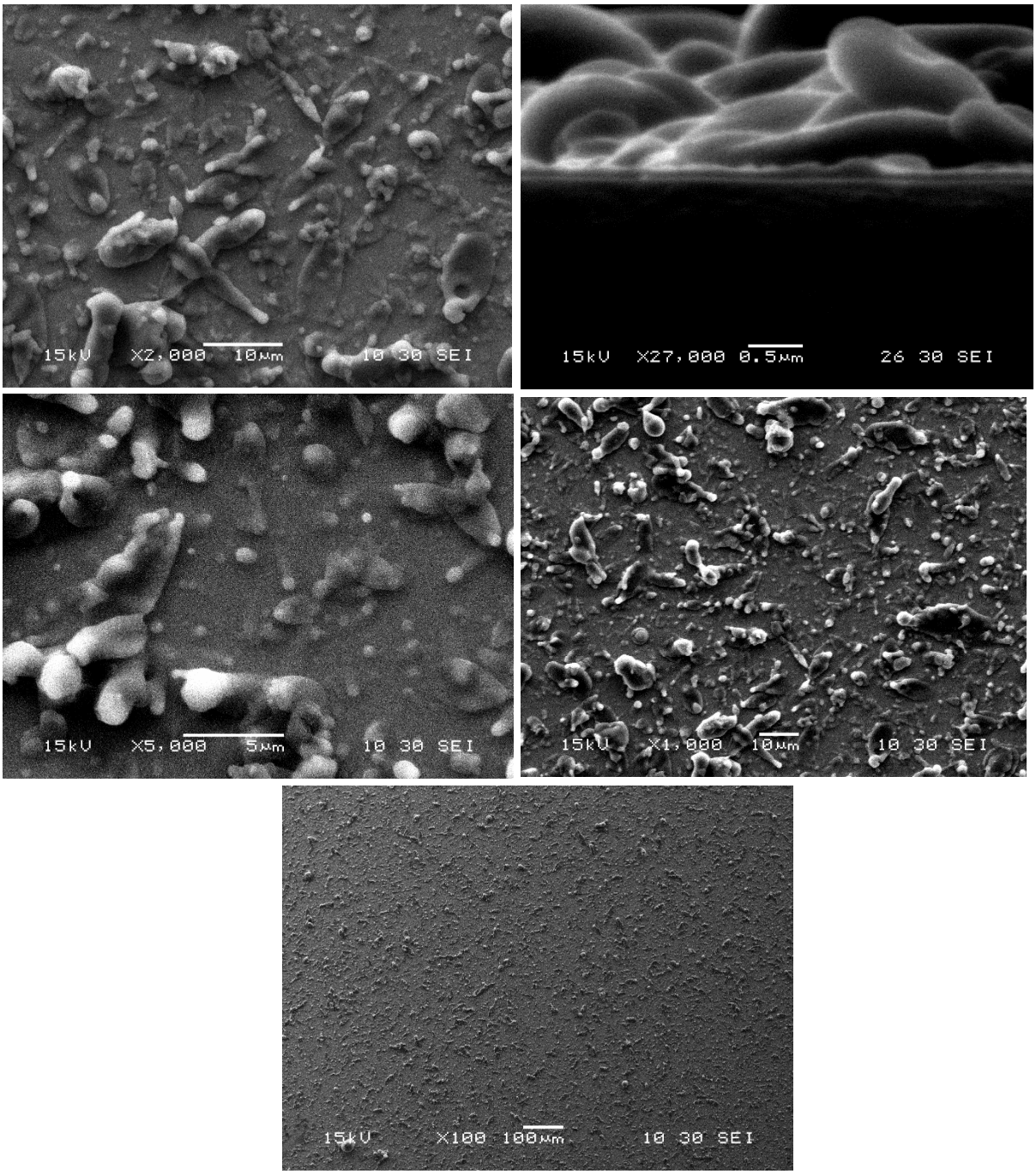

Fig. 6.9 SEM image of Al on Si deposited by the pulse laser deposition. Nd:YAG laser pulse intensity ~ 5×10^9 W/cm^2 at 5 Hz repetition rate is used to deposit Al for 90 min. The film thickness of approximately ~200 nm is detected from the cross-section image.

6.5 On-line aluminum thin-film thickness measurement

Picosecond acoustics was initially developed by Maris and Tauc at Brown University [121]. This technique is extended to the sub-picosecond time domain and utilized in the study of the properties of buried interfaces and in characterizing the acoustic properties of thin-films and interfaces [122, 123]. Picosecond ultrasonic setup was used to deduce Young's modulus and Poisson's ratio of any isotropic thin-film [124]. Picosecond acoustics was also studied in polymer, transparent thin-films and metal-liquid interfaces [125-127]. Jacqueline *et al.* measured the time-of-flight of the acoustic pulse at $\Delta R(t)/R$ of about 10^{-5} to detect up to the fifth picosecond acoustics echo in a 50 nm Al film on the sapphire substrate [128]. Norris *et al.* extrapolated the thermal conductivity of a tungsten thin-film through a curve-fitting method that compares results with the parabolic two-step (PTS) heat diffusion model and the thickness by the observation of ultrasonic waves generated by femtosecond laser heating pulses [129].

In this work, we used a non-contact and non-destructive optical pump-probe spectroscopy to probe the *in-situ* growth of Al and on Si during thermal evaporation. The thickness of the film is varied between 30 to 370 nm.

6.6 Experimental setup

The *in-situ* Al thin film growth is monitored inside a vacuum chamber. A customized vacuum chamber is designed for this experimental purpose. Si substrate is mounted on a thermal evaporator that is used to grow the thin-film on Si substrate. Al wire (99.999%) is evaporated using tungsten filament at a 45º angle to the normal target surface. The vacuum pressure of the chamber is maintained in the low 10^{-7} range which increases up to a low of 10^{-6} during deposition.

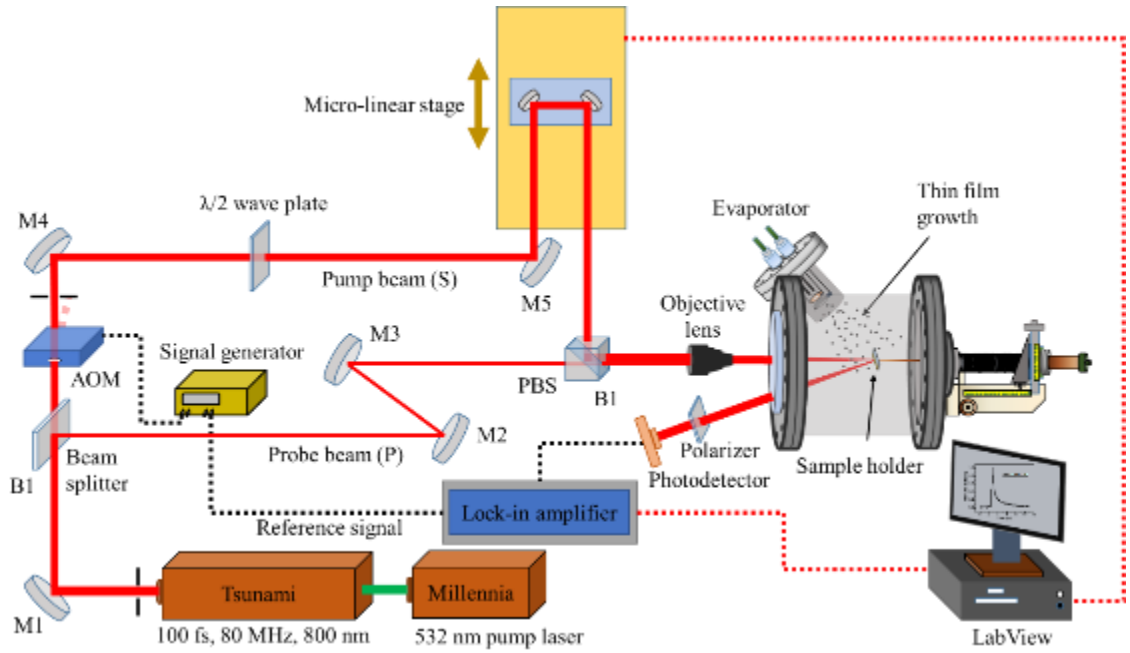

Fig. 6.10 Femtosecond time-domain thermoreflectance pump-probe setup. The acousto-optic modulator is used to modulate the pump beam at 1 MHz frequency. The linear stage is used to create the time delay between pump and probe beam.

6.7 Results

The principle of the pump-probe technique is shown in Fig. 6.10. A femtosecond pump pulse is focused onto the Al thin-film. The temperature rise in the Al surface depends on the incident laser intensity, reflectance and skin depth of the thin-film material [130]. The sudden increase in temperature causes thermal stress in the illuminated area. The material on the surface region expands and launches a longitudinal acoustic pulse into the thin-film. The spatial dependence of the pulse depends on the absorption profile and the acoustic boundary condition of the thin-film. The generated pulse propagates through the film, reflects at the interface to substrate or at an inhomogeneity in the film and returns to the front surface after a time $t = 2d/v$where d is the thickness of the film. The thickness of the thin-film d can be determined with the given knowledge of the sound velocity v inside the thin-film. The defect inside the thin-film can also be detected if its extent is parallel to the surface is comparable with the illuminated area of the sample. In the pump-probe setup, the probe pulse, whose duration is the same as pump

pulse, is focused onto the same spot as the pump but is delayed in time. The reflectivity undergoes a change ΔR when the acoustic pulse approaches the surface. The change in reflectivity is related to the temperature derivative of the refractive index, and for small temperature excursions the temperature derivative is constant [131]. The reflectivity of a metal surface decreases with the increasing temperature. This situation is analogous to the decrease in electrical conductivity with increasing temperature, and it is the result of an increased electron-phonon collision frequency [131]. Thomsen *et al.* showed that the complex index of refraction coefficients is a function not only of temperature, but also strain, $\eta(z,t)$ [121]. The corresponding change in the refraction coefficients as a function of strain is given by the equations

$$\Delta n(z,t) = \frac{\partial n}{\partial \eta}\eta(z,t)$$

$$\Delta k(z,t) = \frac{\partial k}{\partial \eta}\eta(z,t)$$

where z is the spatial variable perpendicular to the film surface and t is the acoustic propagation time in the film. The refraction coefficients are material constants. The knowledge of the change in refraction coefficients due to strain is not required for thickness measurements. The round-trip time of the echoes are determined, and the thin-film thickness is calculated by correlating period of the echoes with the longitudinal sound velocity inside the thin-film.

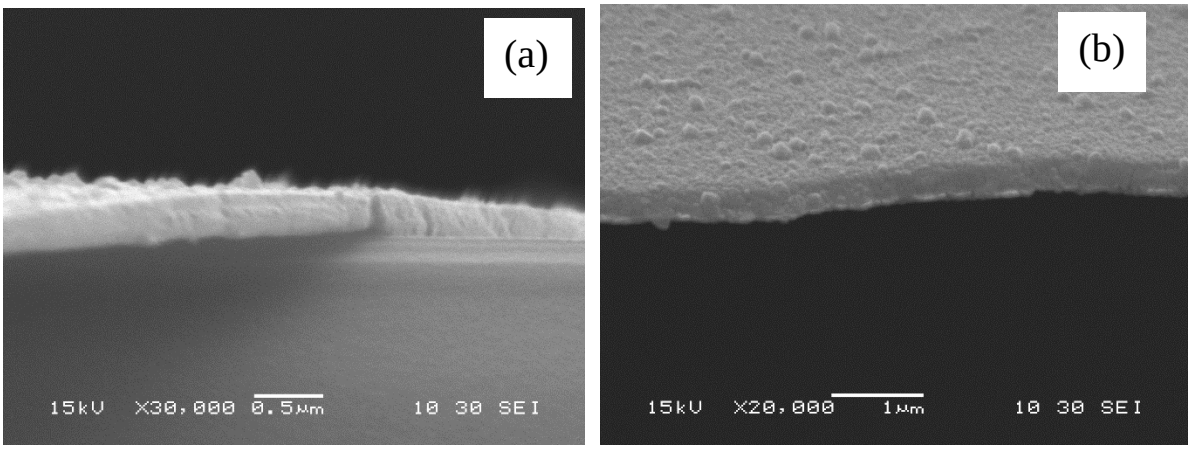

Fig. 6.11 The cross-section SEM image of Al film. The film is deposited for 1.5 hr. The input voltage on the variac transformer is 10 V. The Al film thickness is measured as 370 nm.

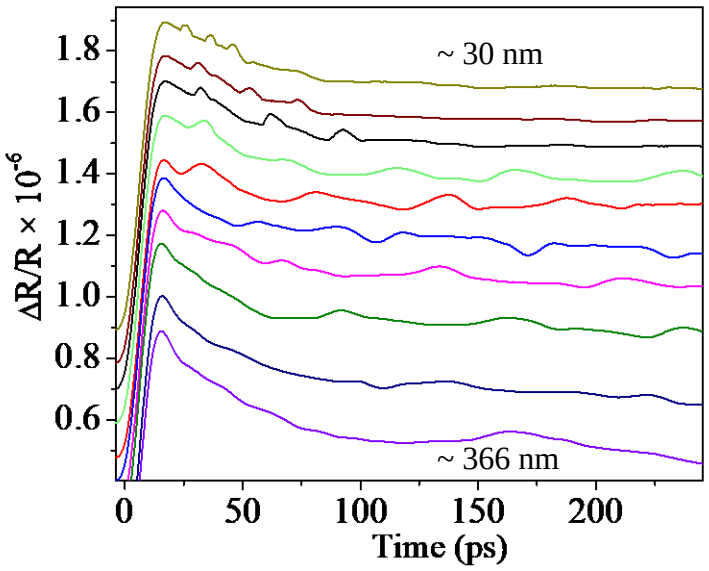

Fig. 6.12 Online thermoreflectance response of Aluminum thin film on a silicon substrate. The *ΔR/R* response is measured during the film deposition by thermal evaporation. The film thickness of 30 to 366 nm is detected by the thermoreflectance response.

The online thermoreflectance signal from the Al film at room temperature is monitored. Fig. 6.12 shows the reflectivity response of the Al thin-film deposited on a silicon substrate for 1.5 hrs. The acoustic pulse reflection and attenuation at the film surface is detected at 25 ps. The ultrasonic echoes have a period of 10 ps, which corresponds to a film thickness of ~30 nm for a longitudinal sound velocity of 6,320 ms^{-1} inside Al thin-film. The *ΔR/R* is measured continuously at the same spot. The film thickness is measured as 30, 63, 94, 126, 183, 199, 225, 233, and 366 nm. No ultrasonic eco is observed for the film thickness out of the 30 – 366 nm range. The cross-section SEM image shows the film thickness of 370 nm.

The femtosecond laser pulse localized the heat both spatially and temporally on the thin films. To measure the thermal properties, a relationship between the reflectance of the film and the theoretical thermal response must be known. The parabolic one-step heat transfer model is given by

$$C\frac{\partial T_{(x,t)}}{\partial t} = -K\frac{\partial^2 T_{(x,t)}}{\partial x^2}) + I(1-R).\alpha.exp(-\alpha x)\,exp(t/\tau)^2 \qquad (6.1)$$

where $T(x,t)$ is the temperature profile, x is the distance normal to the film surface, C is the heat capacity per unit volume, K is the thermal conductivity, R is the reflectance of the film, I is the laser intensity, α is absorption per unit length or the skin depth, τ is the laser pulse width, x is the direction normal to the film surface, J is the laser fluence, t_p is the laser pulse width, R is the reflectance of the film, and d is the optical penetration depth. The assumption of a one-dimensional thermal model is valid for film thicknesses much less than the diameter of the heated region. Thermoreflectance results have an initial fast transient, followed by a gradual decay and finally, some nominal value of the signal remains. This spike is primarily due to the initial absorption of the laser by electrons followed by electron-phonon relaxation. Although the initial response depends on the electron temperature, the signal after ~100 ps of initial change depends entirely on the lattice temperatures.

The heat transfer mechanism can be evaluated by extrapolating the simulation data with the experimental data. The comparison between the heat equation and the experimental data is shown in Fig. 6.13. In the heat transfer model, the heat diffusion is calculated with respect to film thickness as well as heat diffusion time. For the 30 nm film, the heat transfer result shows a zero slope after 25 ps whereas the 366 nm Al film shows a nearly exponential decay of the temperature with time. The thermal conductivity of the Si substrate is ~180 times less than the Al thin film, so no significant heat transfer occurs between the Al thin film and Si substrate. The detail thin film thickness dependence heat diffusion simulation is provided in appendix A.

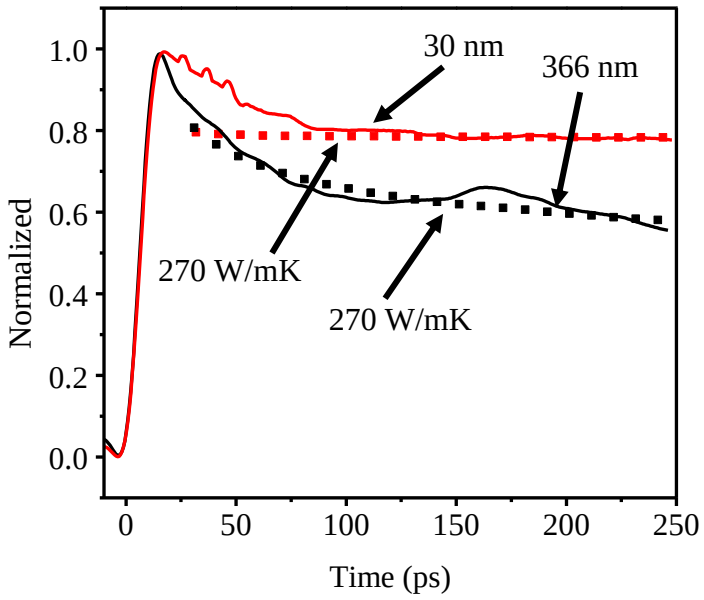

Fig. 6.13 Comparison between the thermomodulation experimental data with the heat diffusion model at different thickness. The heat diffusion model is fitted for 270 W/mK.

6.8 Conclusion

The major outcomes of our work are the construction and optimization of a femtosecond pump-probe experimental setup to measure the thermal conductivities of superconductive Nb. A 100 mm delay line is used to measure the themoreflectance signal ($\Delta R/R$) in the order of ~10^{-6} up to 650 ps. In addition, the modulation frequency, modulation depth and power of the pump beam are optimized for our experimental setup. A femtosecond pump-probe experimental setup is used to determine the *in-situ* thickness of thermally evaporating Al onto a silicon substrate by detecting propagating ultrasonic acoustic waves. The procedure shows a non-contact, *in-situ* thin-film characterization. This technique is most effective for highly reflective thin-films as well as a substrate film combined with a high coefficient of acoustic mismatch.

CHAPTER 7

SUMMARY

A Q-switched Nd:YAG laser pulse is used to generate multicharged ions from the solid Al and C target. Laser plasma is characterized by optical emission spectra and the time-of-flight ion detection system which consists of a Faraday cup, retarding field analyzer and electrostatic energy analyzer. Retarding electric field is used to determine the kinetic energy of multicharged ions. Up to C^{4+} and Al^{4+} are generated using the laser pulse only.

The ion transport line components of the laser ion system such as einzel lens and hemispherical electrostatic energy analyzer are simulated by ion simulation software SIMION to detect the optimum condition of ion beam focusing and bending. Up to a 1 mm diameter beam can be generated using an einzel lens, and specific ion groups can be detected by the hemispherical energy analyzer depending on their energy to charge ratio.

A spark discharge pulse forming network is integrated with the laser ion source to increase the ionization of laser plasma. The spark discharge coupling to laser plasma delivered up to C^{6+} and Al^{8+}. Spark-discharge energy further ionized the plasma produced by the laser pulse at low laser energies. Optical emission spectra and the time-of-flight signal are investigated to estimate the plasma temperature and density. The optical emission spectra and TOF signal confirm that the plasma temperature increases when the spark-discharge is initiated. Introducing an additional electrical field to the source chamber showed that the generated ions can gain extra kinetic energy and can be accelerated to several keV energies.

Several experiments were conducted to study the thermal conductivity of the Al thin film. For this purpose, femtosecond pump-probe spectroscopy is constructed in the research facility of Applied Research Center in Newport News, VA. First, the pulse laser deposition technique was used to deposit the Al thin film on Si substrate. The thermal conductivity was measured, butno ultrasonic eco was detected for pulse laser deposition Al film. The thermal evaporation was used to deposit more uniform Al thin film. *In-situ* film thickness from 30 to 366 nm was detected using the ultrasonic eco generated by the femtosecond laser pulse.

REFERENCES

[1] T. Fujihana, A. Sekiguchi, Y. Okabe, K. Takahashi, and M. Iwaki, "Effects of room temperature carbon, nitrogen and oxygen implantation on the surface hardening and corrosion protection of iron," *Surface and Coatings Technology,* vol. 51, no. 1, pp. 19-23, 1992.

[2] S. Witanachchi, A. M. Miyawa, and P. Mukherjee, "Highly Ionized Carbon Plasma Generation by Dual-Laser Ablation for Diamond-Like Carbon Film Growth," *MRS Proceedings,* vol. 617, 2000, Art. no. J3.6.

[3] T. K. Hirohiko Tsujii, Toshiyuki Shirai, Koji Noda, Hiroshi Tsuji, Kumiko Karasawa, *Carbon-Ion Radiotherapy*. Japan: Springer, Tokyo, 2014.

[4] G. Impellizzeri *et al.*, "C ion-implanted TiO2 thin film for photocatalytic applications," *Journal of Applied Physics,* vol. 117, no. 10, pp. 105308, 2015.

[5] J. Kim, G. Lee, and J. Kim, "Wafer-scale synthesis of multi-layer graphene by high-temperature carbon ion implantation," *Applied Physics Letters,* vol. 107, no. 3, pp. 033104, 2015.

[6] J. D. Gillaspy, "Highly charged ions," *Journal of Physics B: Atomic, Molecular and Optical Physics,* vol. 34, no. 19, pp. R93, 2001.

[7] K. Amemiya, J. Ito, and K. Tokiguchi, "High energy aluminum ion implantation using a variable energy radio frequency quadrupole implanter," *Journal of Vacuum Science & Technology A: Vacuum, Surfaces, and Films,* vol. 16, no. 2, pp. 472-476, 1998.

[8] J. D. Gillaspy, D. C. Parks, and L. P. Ratliff, "Masked ion beam lithography with highly charged ions," *Journal of Vacuum Science & Technology B: Microelectronics and Nanometer Structures Processing, Measurement, and Phenomena,* vol. 16, no. 6, pp. 3294-3297, 1998.

[9] F. Aumayr and H. Winter, "Potential sputtering," *Philosophical Transactions of the Royal Society of London. Series A: Mathematical, Physical and Engineering Sciences,* vol. 362, no. 1814, pp. 77, 2004.

[10] W. Takahashi *et al.*, "Carbon ion radiotherapy for oligo-recurrent lung metastases from colorectal cancer: a feasibility study," *Radiation Oncology (London, England)*, vol. 9, pp. 68-68, 2014.

[11] T. Ohno, "Particle radiotherapy with carbon ion beams," *The EPMA Journal*, vol. 4, no. 1, pp. 9-9, 2013.

[12] A. Y. Boytsov *et al.*, "Electron string ion sources for carbon ion cancer therapy accelerators," *Review of Scientific Instruments*, vol. 86, no. 8, pp. 083308, 2015.

[13] M. Muramatsu and A. Kitagawa, "A review of ion sources for medical accelerators (invited)," *Review of Scientific Instruments*, vol. 83, no. 2, pp. 02B909, 2012.

[14] X. Wang, S. Zhang, X. Cheng, E. Zhu, W. Hang, and B. Huang, "Ion kinetic energy distributions in laser-induced plasma," *Spectrochimica Acta Part B: Atomic Spectroscopy*, vol. 99, pp. 101-114, 2014.

[15] M. H. A. Shaim, M. M. Rahman, O. Balki, A. Sarkissian, M. L. Korwin-Pawlowski, and H. E. Elsayed-Ali, "Transport line for laser multicharged ion source," *Vacuum*, vol. 137, pp. 14-22, 2017.

[16] M. Kenji, "Selective Sputtering of Impurity Hydrogen Atoms from a GaN(0001) Surface by Slow Multicharged Ion Impact," *Applied Physics Express*, vol. 3, no. 12, pp. 126301, 2010.

[17] R. Christiane, S. Dieter, S. Markus, D. D. Robert, and B. Rod, "Protein fragmentation due to slow highly charged ion impact," *Nanotechnology*, vol. 9, no. 3, pp. 251, 1998.

[18] A. Kitagawa *et al.*, "Multiply charged carbon-ion production for medical application," *Review of Scientific Instruments*, vol. 79, no. 2, pp. 02C303, 2008.

[19] C. Pierret *et al.*, "Friction and wear properties modification of Ti–6Al–4V alloy surfaces by implantation of multi-charged carbon ions," *Wear*, vol. 319, no. 1, pp. 19-26, 2014.

[20] N. J. Peacock and R. S. Pease, "Sources of highly stripped ions," *Journal of Physics D: Applied Physics*, vol. 2, no. 12, pp. 1705, 1969.

[21] V. B. Kutner, Y. A. Bykovsky, V. P. Gusev, Y. P. Kozyrev, and V. D. Peklenkov, "The laser ion source of multiply charged ions for the U-200 LNR JINR cyclotron," *Review of Scientific Instruments*, vol. 63, no. 4, pp. 2835-2837, 1992.

[22] D. Hiroyuki, N. Mamiko, and S. P. Alexander, "Review of laser-driven ion sources and their applications," *Reports on Progress in Physics*, vol. 75, no. 5, pp. 056401, 2012.

[23] M. Haider A. Shaim and H. E. Elsayed-Ali, "Aluminum multicharged ion generation from laser plasma," *Nuclear Instruments and Methods in Physics Research Section B: Beam Interactions with Materials and Atoms,* vol. 356, pp. 75-80, 2015.

[24] K. Bernhardi *et al.*, "Studies of electron heating and multiply charged ion production in an electron cyclotron resonance plasma," *Plasma Physics,* vol. 18, no. 2, pp. 77, 1976.

[25] A. L. Morton, R. E. Marrs, J. R. Henderson, D. A. Knapp, and B. S. Marilyn, "The Electron Beam Ion Trap: A New Instrument for Atomic Physics Measurements," *Physica Scripta,* vol. 1988, no. T22, pp. 157, 1988.

[26] O. Balki and H. E. Elsayed-Ali, "Multicharged carbon ion generation from laser plasma," *Review of Scientific Instruments,* vol. 87, no. 11, p. 113304, 2016.

[27] M. H. A. Shaim and H. E. Elsayed-Ali, "Spark discharge coupled laser multicharged ion source," *Review of Scientific Instruments,* vol. 86, no. 7, pp. 073304, 2015.

[28] O. Balki, M. M. Rahman, S. Xiao, and H. E. Elsayed-Ali, "Generation of C6+ in a spark-discharge coupled laser plasma," *Optics Communications,* vol. 403, no. Supplement C, pp. 50-54, 2017.

[29] A. M. M, "Factors Enhancing Production of Multicharged Ion Sources and Their Applications," *Science and Technology,* vol. 2, pp. 98-108, 2012.

[30] R. Kelly and R. W. Dreyfus, "On the effect of Knudsen-layer formation on studies of vaporization, sputtering, and desorption," *Surface Science,* vol. 198, no. 1, pp. 263-276, 1988.

[31] F. F. Chen, "Decay of a plasma created between negatively biased walls," *Physics of Fluids,* vol. 25, no. 12, pp. 2385-2387, 1982.

[32] H. Horisawa and I. Kimura, "Fundamental study on laser plasma accelerator for propulsion applications," *Vacuum,* vol. 65, no. 3, pp. 389-396, 2002.

[33] I. G. Brown, "Vacuum arc ion sources," *Review of Scientific Instruments,* vol. 65, no. 10, pp. 3061-3081, 1994.

[34] M. M. M. Bilek, P. J. Martin, and D. R. McKenzie, "Influence of gas pressure and cathode composition on ion energy distributions in filtered cathodic vacuum arcs," *Journal of Applied Physics,* vol. 83, no. 6, pp. 2965-2970, 1998.

[35] A. Anders, "A Brief History of Cathodic Arc Coating," in *Cathodic Arcs: From Fractal Spots to Energetic Condensation*, A. Anders, Ed. New York, NY: Springer New York, 2008, pp. 1-68.

[36] P. A. Lindfors, W. M. Mularie, and G. K. Wehner, "Cathodic arc deposition technology," *Surface and Coatings Technology,* vol. 29, no. 4, pp. 275-290, 1986.

[37] E. Hantzsche, "- Theories of Cathode Spots," in *Handbook of Vacuum Arc Science and Technology*, R. L. Boxman, D. M. Sanders, and P. J. Martin, Eds. Park Ridge, NJ: William Andrew Publishing, 1996, pp. 151-208.

[38] J. Kutzner and H. C. Miller, "Integrated ion flux emitted from the cathode spot region of a diffuse vacuum arc," *Journal of Physics D: Applied Physics,* vol. 25, no. 4, p. 686, 1992.

[39] H. J. Scheibe, P. Siemroth, W. Pompe, and B. Schoeneich, "Laser-arc: A new method for preparation of diamond-like carbon films," *Surface and Coatings Technology,* vol. 47, no. 1, pp. 455-464, 1991.

[40] H. J. Scheibe, B. Schultrich, R. Wilberg, and M. Falz, "Laser-Arc technology for industrial hard coating deposition," *Surface and Coatings Technology,* vol. 97, no. 1, pp. 410-413, 1997.

[41] A. B. Girum *et al.*, "Laser-assisted vacuum arc extreme ultraviolet source: a comparison of picosecond and nanosecond laser triggering," *Journal of Physics D: Applied Physics,* vol. 49, no. 22, p. 225201, 2016.

[42] M. M. Rahman, O. Balki, and H. E. Elsayed-Ali, "Diagnostics of a spark-discharge coupled to laser aluminum plasma by optical emission spectroscopy and ion time-of-flight," *Optics & Laser Technology,* vol. 111, pp. 762-769, 2019.

[43] J. S. Lash, R. M. Gilgenbach, and H. L. Spindler, "Characterization of a laser-ablation-assisted-plasma-discharge-metallic ion source," *Plasma Sources Science and Technology,* vol. 4, no. 4, pp. 511, 1995.

[44] S. Takagi, S. Ohtani, K. Kadota, and J. Fujita, "Collision experiment on highly ionized ions using a vacuum spark source," *Nuclear Instruments and Methods in Physics Research,* vol. 213, no. 2, pp. 539-544, 1983.

[45] A. V. Kabashin *et al.*, "Nanofabrication with Pulsed Lasers," *Nanoscale Research Letters,* vol. 5, no. 3, pp. 454, 2010.

[46] J. A. Aguilera and C. Aragón, "A comparison of the temperatures and electron densities of laser-produced plasmas obtained in air, argon, and helium at atmospheric pressure," *Applied Physics A,* vol. 69, no. 1, pp. S475-S478, 1999.

[47] T. Moscicki, J. Hoffman, and Z. Szymanski, "The effect of laser wavelength on laser-induced carbon plasma," *Journal of Applied Physics,* vol. 114, no. 8, pp. 083306, 2013.

[48] S. S. Harilal, C. V. Bindhu, M. S. Tillack, F. Najmabadi, and A. C. Gaeris, "Internal structure and expansion dynamics of laser ablation plumes into ambient gases," *Journal of Applied Physics,* vol. 93, no. 5, pp. 2380-2388, 2003.

[49] M. S. Brown and C. B. Arnold, "Fundamentals of Laser-Material Interaction and Application to Multiscale Surface Modification," in *Laser Precision Microfabrication*, K. Sugioka, M. Meunier, and A. Piqué, Eds. Berlin, Heidelberg: Springer Berlin Heidelberg, 2010, pp. 91-120.

[50] H. R. Griem, *Principles of Plasma Spectroscopy*. Cambridge University Press, 1997.

[51] S. Amoruso, M. Armenante, V. Berardi, R. Bruzzese, and N. Spinelli, "Absorption and saturation mechanisms in aluminium laser ablated plasmas," *Applied Physics A,* vol. 65, no. 3, pp. 265-271, 1997.

[52] K. Jakubczak, "High-order Harmonic Generation," 2010.

[53] O. Samek *et al.*, "Quantitative laser-induced breakdown spectroscopy analysis of calcified tissue samples," *Spectrochimica Acta Part B: Atomic Spectroscopy,* vol. 56, no. 6, pp. 865-875, 2001.

[54] D. A. Cremers, L. J. Radziemski, and T. R. Loree, "Spectrochemical Analysis of Liquids Using the Laser Spark," *Applied Spectroscopy*, vol. 38, no. 5, pp. 721-729, 1984.

[55] F. Anabitarte, A. Cobo, and J. M. Lopez-Higuera, "Laser-Induced Breakdown Spectroscopy: Fundamentals, Applications, and Challenges," *ISRN Spectroscopy,* vol. 2012, pp. 12, 2012.

[56] J. Cooper, "Plasma spectroscopy," *Reports on Progress in Physics,* vol. 29, no. 1, pp. 35-130, 1966.

[57] T. P. Hughes, *Plasmas and laser light*. New York: Wiley, 1975.

[58] M. Mattioli and D. Véron, "Electron-ion recombination in laser produced plasma," *Plasma Physics,* vol. 11, no. 8, pp. 684-686, 1969.

[59] C. Blancard, G. Faussurier, T. Kato, and R. M. More, "Effective Boltzmann law and Prigogine theorem of minimum entropy production in highly charged ion plasmas," *Journal of Quantitative Spectroscopy and Radiative Transfer*, vol. 99, no. 1, pp. 75-83, 2006.

[60] C. Deutsch, "Validity of complete local thermodynamic equilibrium for HeI," *Physics Letters A*, vol. 28, no. 11, pp. 752-753, 1969.

[61] I. V. Veryovkin, W. F. Calaway, and M. J. Pellin, "Ion optics of a new time-of-flight mass spectrometer for quantitative surface analysis," *Nuclear Instruments and Methods in Physics Research Section A: Accelerators, Spectrometers, Detectors and Associated Equipment*, vol. 519, no. 1, pp. 353-362, 2004.

[62] Y. Toker *et al.*, "The kick-out mass selection technique for ions stored in an Electrostatic Ion Beam Trap," *Journal of Instrumentation*, vol. 4, no. 09, pp. P09001-P09001, 2009.

[63] A. V. Steele, B. Knuffman, J. J. McClelland, and J. Orloff, "Focused chromium ion beam," *Journal of Vacuum Science & Technology B*, vol. 28, no. 6, pp. C6F1-C6F5, 2010.

[64] O. Sise, M. Ulu, and M. Dogan, "Multi-element cylindrical electrostatic lens systems for focusing and controlling charged particles," *Nuclear Instruments and Methods in Physics Research Section A: Accelerators, Spectrometers, Detectors and Associated Equipment*, vol. 554, no. 1, pp. 114-131, 2005.

[65] O. Sise, M. Ulu, and M. Dogan, "Characterization and modeling of multi-element electrostatic lens systems," *Radiation Physics and Chemistry*, vol. 76, no. 3, pp. 593-598, 2007.

[66] O. Sise, M. Ulu, and M. Dogan, "Aberration coefficients of multi-element cylindrical electrostatic lens systems for charged particle beam applications," *Nuclear Instruments and Methods in Physics Research Section A: Accelerators, Spectrometers, Detectors and Associated Equipment*, vol. 573, no. 3, pp. 329-339, 2007.

[67] M. Abdelrahman, "Ion beam simulation using a three electrode diaphragm Einzel lens system," *J. Nucl. Rad. Phys*, vol. 3, no. 2, pp. 93-100, 2008.

[68] M. Rashid, "Simple analytical method to design electrostatic einzel lens," in *Proceedings of the DAE Symp. on Nucl. Phys*, 2011, vol. 56, pp. 1132.

[69] F. A. Al-Moudarris, O. A. Hussein, and M. M. A. Ali, "Design of an Einzel Lens Using Non-Classical Variation Technique."

[70] D. Dahl, J. Delmore, and A. Appelhans, "SIMION PC/PS2 electrostatic lens design program," *Review of Scientific Instruments,* vol. 61, no. 1, pp. 607-609, 1990.

[71] D. A. Dahl, "simion for the personal computer in reflection," *International Journal of Mass Spectrometry,* vol. 200, no. 1, pp. 3-25, 2000.

[72] L. Torrisi, S. Gammino, L. Andò, and L. Laska, "Tantalum ions produced by 1064 nm pulsed laser irradiation," *Journal of applied physics,* vol. 91, no. 7, pp. 4685-4692, 2002.

[73] N. M. Bulgakova, A. V. Bulgakov, and O. F. Bobrenok, "Double layer effects in laser-ablation plasma plumes," *Physical Review E,* vol. 62, no. 4, pp. 5624, 2000.

[74] L. Torrisi, F. Caridi, D. Margarone, and A. Borrielli, "Plasma–laser characterization by electrostatic mass quadrupole analyzer," *Nuclear Instruments and Methods in Physics Research Section B: Beam Interactions with Materials and Atoms,* vol. 266, no. 2, pp. 308-315, 2008.

[75] S. Shan *et al.*, "Charge state distribution analysis of Al and Pb ions from the laser ion source at IMP," *Chinese Physics C,* vol. 37, no. 11, pp. 117006, 2013.

[76] E. Woryna, P. Parys, and J. Wołowski, "Corpuscular diagnostics and processing methods applied in investigations of laser-produced plasma as a source of highly ionized ions," *Laser and Particle Beams,* vol. 14, no. 03, pp. 293-321, 1996.

[77] A. D. Appelhans and D. A. Dahl, "SIMION ion optics simulations at atmospheric pressure," *International Journal of Mass Spectrometry,* vol. 244, no. 1, pp. 1-14, 2005.

[78] G. N. Glasoe and J. V. Lebacqz, *Pulse generators,* 1st ed. New York,: McGraw-Hill Book Co., 1948,

[79] B. B. Kadomtsev and V. N. Tsytovich, "Collective Plasma Phenomena and their Role in the Dynamics of the Interstellar Medium," in *Interstellar Gas Dynamics*, H. J. Habing, Ed. Dordrecht: Springer Netherlands, pp. 108-132, 1970,

[80] N. M. Bulgakova, A. V. Bulgakov, and O. F. Bobrenok, "Double layer effects in laser-ablation plasma plumes," *Physical Review E,* vol. 62, no. 4, pp. 5624-5635, 2000.

[81] P. Yeates, J. T. Costello, and E. T. Kennedy, "The DCU laser ion source," *Review of Scientific Instruments,* vol. 81, no. 4, pp. 043305, 2010.

[82] A. Anders, S. Anders, B. Juttner, W. Botticher, H. Luck, and G. Schroder, "Pulsed dye laser diagnostics of vacuum arc cathode spots," *IEEE Transactions on Plasma Science,* vol. 20, no. 4, pp. 466-472, 1992.

[83] P. Siemroth, B. Schultrich, and T. Schülke, "Fundamental processes in vacuum arc deposition," *Surface and Coatings Technology,* vol. 74-75, pp. 92-96, 1995.

[84] F. F. Chen, "Decay of a plasma created between negatively biased walls," *The Physics of Fluids,* vol. 25, no. 12, pp. 2385-2387, 1982.

[85] K. Yamada, T. Tetsuka, and Y. Deguchi, "New scaling relation for ion extraction by external electric field on a barium plasma produced between parallel-plate electrodes," *Journal of Applied Physics,* vol. 69, no. 10, pp. 6962-6967, 1991.

[86] H. Ryufuku and T. Watanabe, "Total and partial cross sections for charge transfer in collisions of multicharged ions with atomic hydrogen," *Physical Review A,* vol. 20, no. 5, pp. 1828-1837, 1979.

[87] S. S. Harilal, A. Hassanein, and M. Polek, "Late-time particle emission from laser-produced graphite plasma," *Journal of Applied Physics,* vol. 110, no. 5, p. 053301, 2011.

[88] A. Anders, "Approaches to rid cathodic arc plasmas of macro- and nanoparticles: a review," *Surface and Coatings Technology,* vol. 120-121, pp. 319-330, 1999.

[89] A. Anders, "Interaction of vacuum-arc-generated macroparticles with a liquid surface," *Applied Physics Letters,* vol. 73, no. 22, pp. 3199-3201, 1998.

[90] S. Thomas and AndréAnders, "Velocity distribution of carbon macroparticles generated by pulsed vacuum arcs," *Plasma Sources Science and Technology,* vol. 8, no. 4, p. 567, 1999.

[91] G. L. Eesley, "Observation of Nonequilibrium Electron Heating in Copper," *Physical Review Letters,* vol. 51, no. 23, pp. 2140-2143, 1983.

[92] H. E. Elsayed-Ali, T. B. Norris, M. A. Pessot, and G. A. Mourou, "Time-resolved observation of electron-phonon relaxation in copper," *Physical Review Letters,* vol. 58, no. 12, pp. 1212-1215, 1987.

[93] R. H. M. Groeneveld, R. Sprik, and A. Lagendijk, "Femtosecond spectroscopy of electron-electron and electron-phonon energy relaxation in Ag and Au," *Physical Review B,* vol. 51, no. 17, pp. 11433-11445, 1995.

[94] H. Inouye, K. Tanaka, I. Tanahashi, and K. Hirao, "Ultrafast dynamics of nonequilibrium electrons in a gold nanoparticle system," *Physical Review B,* vol. 57, no. 18, pp. 11334-11340, 1998.

[95] J. Cao, Y. Gao, R. J. D. Miller, H. E. Elsayed-Ali, and D. A. Mantell, "Femtosecond photoemission study of ultrafast electron dynamics on Cu(100)," *Physical Review B,* vol. 56, no. 3, pp. 1099-1102, 1997.

[96] T. Mii and H. Ueba, "Theory of time-resolved two-photon photoemission spectroscopy from metal surfaces," *Journal of Luminescence,* vol. 87-89, pp. 898-901, 2000.

[97] R. Rosei and D. W. Lynch, "Thermomodulation Spectra of Al, Au, and Cu," *Physical Review B,* vol. 5, no. 10, pp. 3883-3894, 1972.

[98] T. M. Tritt and D. Weston, "Measurement Techniques and Considerations for Determining Thermal Conductivity of Bulk Materials," in *Thermal Conductivity: Theory, Properties, and Applications*, T. M. Tritt, Ed. Boston, MA: Springer US, pp. 187-203, 2004.

[99] R. C. Zeller and R. O. Pohl, "Thermal Conductivity and Specific Heat of Noncrystalline Solids," *Physical Review B,* vol. 4, no. 6, pp. 2029-2041, 1971.

[100] T. Borca-Tasciuc, A. R. Kumar, and G. Chen, "Data reduction in 3ω method for thin-film thermal conductivity determination," *Review of Scientific Instruments,* vol. 72, no. 4, pp. 2139-2147, 2001.

[101] D. G. Cahill, K. Goodson, and A. Majumdar, "Thermometry and Thermal Transport in Micro/Nanoscale Solid-State Devices and Structures," *Journal of Heat Transfer,* vol. 124, no. 2, pp. 223-241, 2001.

[102] T. Borca-Tasciuc and G. Chen, "Experimental Techniques for Thin-Film Thermal Conductivity Characterization," in *Thermal Conductivity: Theory, Properties, and Applications*, T. M. Tritt, Ed. Boston, MA: Springer US, pp. 205-237, 2004.

[103] D. G. Cahill *et al.*, "Nanoscale thermal transport. II. 2003–2012," *Applied Physics Reviews,* vol. 1, pp. 011305, 2014.

[104] D. Zhao, X. Qian, X. Gu, S. A. Jajja, and R. Yang, "Measurement Techniques for Thermal Conductivity and Interfacial Thermal Conductance of Bulk and Thin Film Materials," *Journal of Electronic Packaging,* vol. 138, no. 4, pp. 040802-040802-19, 2016.

[105] R. W. Schoenlein, W. Z. Lin, J. G. Fujimoto, and G. L. Eesley, "Femtosecond studies of nonequilibrium electronic processes in metals," *Physical Review Letters,* vol. 58, no. 16, pp. 1680-1683, 1987.

[106] S. D. Brorson *et al.*, "Femtosecond room-temperature measurement of the electron-phonon coupling constant γ in metallic superconductors," *Physical Review Letters,* vol. 64, no. 18, pp. 2172-2175, 1990.

[107] H. E. Elsayed-Ali, T. Juhasz, G. O. Smith, and W. E. Bron, "Femtosecond thermoreflectivity and thermotransmissivity of polycrystalline and single-crystalline gold films," *Physical Review B,* vol. 43, no. 5, pp. 4488-4491, 1991.

[108] M. Mihailidi, Q. Xing, K. M. Yoo, and R. R. Alfano, "Electron-phonon relaxation dynamics of niobium metal as a function of temperature," *Physical Review B,* vol. 49, no. 5, pp. 3207-3212, 1994.

[109] M. Mihailidi and R. R. Alfano, "Time dependence of the electron-phonon coupling parameter of niobium," *Applied Physics Letters,* vol. 65, no. 1, pp. 106-108, 1994.

[110] K. M. Yoo *et al.*, "Femtosecond thermal modulation measurements of electron-phonon relaxation in niobium," *Applied Physics Letters,* vol. 56, no. 19, pp. 1908-1910, 1990.

[111] C. A. Paddock and G. L. Eesley, "Transient thermoreflectance from thin metal films," *Journal of Applied Physics,* vol. 60, no. 1, pp. 285-290, 1986.

[112] R. Cheaito, C. S. Gorham, A. Misra, K. Hattar, and P. E. Hopkins, "Thermal conductivity measurements via time-domain thermoreflectance for the characterization of radiation induced damage," *Journal of Materials Research,* vol. 30, no. 9, pp. 1403-1412, 2015.

[113] L. David *et al.*, "Characterization of thermal conductivity degradation induced by heavy ion irradiation in ceramic materials," *Journal of Physics D: Applied Physics,* vol. 41, no. 3, pp. 035502, 2008.

[114] C. Jensen, M. Chirtoc, N. Horny, J. S. Antoniow, H. Pron, and H. Ban, "Thermal conductivity profile determination in proton-irradiated ZrC by spatial and frequency scanning thermal wave methods," *Journal of Applied Physics,* vol. 114, no. 13, pp. 133509, 2013.

[115] M. Khafizov, V. Chauhan, Y. Wang, F. Riyad, N. Hang, and D. H. Hurley, "Investigation of thermal transport in composites and ion beam irradiated materials for nuclear energy applications," *Journal of Materials Research,* vol. 32, no. 1, pp. 204-216, 2016.

[116] R. G. Hunsperger, "Acousto-Optic Modulators," in *Integrated Optics: Theory and Technology*, R. G. Hunsperger, Ed. Berlin, Heidelberg: Springer Berlin Heidelberg, 2002, pp. 175-191.

[117] J. L. Hostetler, A. N. Smith, D. M. Czajkowsky, and P. M. Norris, "Measurement of the electron-phonon coupling factor dependence on film thickness and grain size in Au, Cr, and Al," *Applied Optics,* vol. 38, no. 16, pp. 3614-3620, 1999.

[118] B. F. Donovan *et al.*, "Localized thin film damage sourced and monitored via pump-probe modulated thermoreflectance," *Review of Scientific Instruments,* vol. 88, no. 5, pp. 054903, 2017.

[119] J. L. Braun *et al.*, "Size effects on the thermal conductivity of amorphous silicon thin films," *Physical Review B,* vol. 93, no. 14, pp. 140201, 2016.

[120] K. E. Meyer *et al.*, "Crystalline coherence length effects on the thermal conductivity of MgO thin films," *Journal of Materials Science,* vol. 51, no. 23, pp. 10408-10417, 2016.

[121] C. Thomsen, H. T. Grahn, H. J. Maris, and J. Tauc, "Surface generation and detection of phonons by picosecond light pulses," *Physical Review B,* vol. 34, no. 6, pp. 4129-4138, 1986.

[122] K. Ishioka *et al.*, "Sub-picosecond acoustic pulses at buried GaP/Si interfaces," *Applied Physics Letters,* vol. 111, no. 6, pp. 062105, 2017.

[123] C. S. Gorham, J. T. Gaskins, G. N. Parsons, M. D. Losego, and P. E. Hopkins, "Density dependence of the room temperature thermal conductivity of atomic layer deposition-grown amorphous alumina (Al_2O_3)," *Applied Physics Letters,* vol. 104, no. 25, pp. 253107, 2014.

[124] P. A. Mante, J. F. Robillard, and A. Devos, "Complete thin film mechanical characterization using picosecond ultrasonics and nanostructured transducers: experimental demonstration on SiO_2," *Applied Physics Letters,* vol. 93, no. 7, pp. 071909, 2008.

[125] Y. C. Lee, K. C. Bretz, F. W. Wise, and W. Sachse, "Picosecond acoustic measurements of longitudinal wave velocity of submicron polymer films," *Applied Physics Letters,* vol. 69, no. 12, pp. 1692-1694, 1996.

[126] P. Emery and A. Devos, "Acoustic attenuation measurements in transparent materials in the hypersonic range by picosecond ultrasonics," *Applied Physics Letters*, vol. 89, no. 19, p. 191904, 2006.

[127] Akira Harata, Qing Shen, and T. Sawada, "PHOTOTHERMAL APPLICATIONS OF LASERS: Study of Fast and Ultrafast Photothermal Phenomena at Metal-Liquid Interfaces," *Annual Review of Physical Chemistry*, vol. 50, no. 1, pp. 193-219, 1999.

[128] J. Vollmann, D. M. Profunser, and J. Dual, "Sensitivity improvement of a pump–probe set-up for thin film and microstructure metrology," *Ultrasonics*, vol. 40, no. 1, pp. 757-763, 2002.

[129] A. N. S. J. L. Hostetler and P. M. Norris, "Thin-film thermal conductivity and thickness measurements using picosecond ultrasonics," *Microscale Thermophysical Engineering*, vol. 1, no. 3, pp. 237-244, 1997.

[130] T. Q. Qiu and C. L. Tien, "Heat Transfer Mechanisms During Short-Pulse Laser Heating of Metals," *Journal of Heat Transfer*, vol. 115, no. 4, pp. 835-841, 1993.

[131] B. M. Clemens, G. L. Eesley, and C. A. Paddock, "Time-resolved thermal transport in compositionally modulated metal films," *Physical Review B*, vol. 37, no. 3, pp. 1085-1096, 1988.

[132] J. Hohlfeld, S. S. Wellershoff, J. Güdde, U. Conrad, V. Jähnke, and E. Matthias, "Electron and lattice dynamics following optical excitation of metals," *Chemical Physics*, vol. 251, no. 1, pp. 237-258, 2000.

APPENDIX A

LABVIEW AND MATLAB CODE FOR PUMP-PROBE EXPERIMENTAL SETUP

Parabolic one step (POS) temperature model for gold thin film:

```
function pdex4
m = 0;
x = linspace(0,20E-9,1000);                          % 0 to 20 nm film thickness
t = linspace(-2*90E-15,5E-12,1000);                  % -180 fs to 5 Ps time range
sol = pdepe(m,@pdex4pde,@pdex4ic,@pdex4bc,x,t);      %  MATLAB function for PDPE
u = sol(:,:,1);                                      %  Solution for Te

xlswrite('C:\Users\Mahmud\Desktop\matlab example\test1.xls',t(:));      %  record time (x axis )
xlswrite('C:\Users\Mahmud\Desktop\matlab example\test1.xls',u,'b1:b1000');  %  record Te (Y
axis )

function [c,f,s] = pdex4pde(x,t,u,DuDx)
c = 2.5E6;                                                  % heat capacity (C)
f = 315*DuDx;                                               % Conductivity (K)
s = ((1-0.93)*10/(96E-15*15.3E-9))*exp(-(x/15.3E-9)-(2.77*(t/96E-15)^2));    % Source
% ------------------------------------------------------------
function u0 = pdex4ic(x);
u0 = 300;                                                   % initial condition
% ------------------------------------------------------------
function [pl,ql,pr,qr] = pdex4bc(xl,ul,xr,ur,t)             % boundary condition
pl = 0;
ql = 1;
pr = 0;
qr = 1;
```

Two temperature model for Au:

```
function pdex4
m = 0;
x = linspace(0,20E-9,1000);
t = linspace(0E-12,20E-12,1000);

sol = pdepe(m,@pdex4pde,@pdex4ic,@pdex4bc,x,t);
u1 = sol(:,:,1);
u2 = sol(:,:,2);

xlswrite('C:\Users\Mahmud\Desktop\matlab example\test1.xls',t(:));
xlswrite('C:\Users\Mahmud\Desktop\matlab example\test1.xls',u1,'b1:b1000');
xlswrite('C:\Users\Mahmud\Desktop\matlab example\test1.xls',u2,'c1:c1000');

function [c,f,s] = pdex4pde(x,t,u,DuDx)
c = [67.96*u(1); 2.4E6];
f = [318*u(1)/u(2); 0].* DuDx;
y = u(1)-u(2);
F = 2E16*y;
sour=((1-0.4)*4.9/(100E-15*15.3E-9))*exp(-(20e-9/15.3E-9)-(2.77*(t/100E-15)^2));
s = [-F+sour; F];

% --------------------------------------------------------------
function u0 = pdex4ic(x);
u0 = [300;300];
% --------------------------------------------------------------
function [pl,ql,pr,qr] = pdex4bc(xl,ul,xr,ur,t)
pl = [0; 0];
ql = [1; 1];
pr = [0; 0];
qr = [1; 1];
```

Single temperature model for Nb

```
function pdex4
m = 0;
x = linspace(0,100E-6,1000);
t = linspace(-200E-15,700E-12,5000);

sol = pdepe(m,@pdex4pde,@pdex4ic,@pdex4bc,x,t);
u = sol(:,:,1);

% A surface plot is often a good way to study a solution.
%surf(x,t,u)
%title('Numerical solution computed with 20 mesh points.')
%xlabel('Distance x')
%ylabel('Time t')
% ------------------------------------------------------------
xlswrite('C:\Users\Mahmud\Desktop\matlab example\test2.xls',t(:));
xlswrite('C:\Users\Mahmud\Desktop\matlab example\test2.xls',u,'b1:b5000');
function [c,f,s] = pdex4pde(x,t,u,DuDx)
c = 2.3E6;
f = 55*DuDx;
s = ((1-0.93)*.51/(100E-15*15.3E-9))*exp(-(x/15.3E-9)-(2.77*(t/100E-15)^2));
% ------------------------------------------------------------
function u0 = pdex4ic(x);
u0 = 300;
% ------------------------------------------------------------
function [pl,ql,pr,qr] = pdex4bc(xl,ul,xr,ur,t)
pl = 0;
ql = 1;
pr = 0;
qr = 1;
```

Two temperature model for Nb

```
function pdex4
m = 0;
x = linspace(0,1E-6,1000);
t = linspace(-400E-15,500E-12,1000);

sol = pdepe(m,@pdex4pde,@pdex4ic,@pdex4bc,x,t);
u1 = sol(:,:,1);
u2 = sol(:,:,2);

xlswrite('C:\Users\Mahmud\Desktop\matlab example\test1.xls',t(:));
xlswrite('C:\Users\Mahmud\Desktop\matlab example\test1.xls',u1,'b1:b1000');
xlswrite('C:\Users\Mahmud\Desktop\matlab example\test1.xls',u2,'c1:c1000');

function [c,f,s] = pdex4pde(x,t,u,DuDx)
c = [720*u(1); 2.3E6];
f = [55*u(1)/u(2); 0].* DuDx;
y = u(1)-u(2);
F = 20E17*y;
sour=((1-0.93)*.51/(100E-15*15.3E-9))*exp(-(x/15.3E-9)-(2.77*(t/100E-15)^2));
s = [-F+sour; F];
% --------------------------------------------------------------
function u0 = pdex4ic(x);
u0 = [300;300];
% --------------------------------------------------------------
function [pl,ql,pr,qr] = pdex4bc(xl,ul,xr,ur,t)
pl = [0; 0];
ql = [1; 1];
pr = [0; 0];
qr = [1; 1];
```

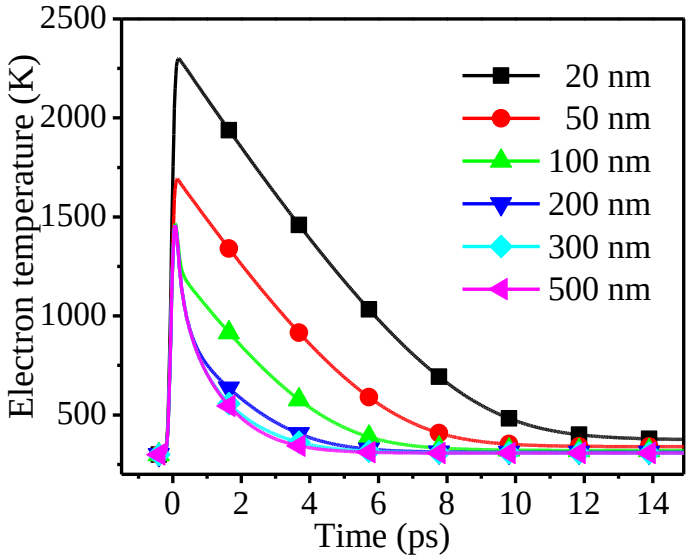

Fig. A.1 Reproduction of Electron temperature relaxation at the surface of 20 to 500 nm Au sample after ref [132]. The following material parameters are used: reflectivity R=0.408, skin depth 1/a = 15.328×l0^{-9} m, electron-phonon coupling coefficient G = 2×10^{16} W/m^{3}K, conductivity K=318 W/mK, A_e=67.96 mJ/cm^2, and absorbed fluence 0.49 mJ/cm^2.

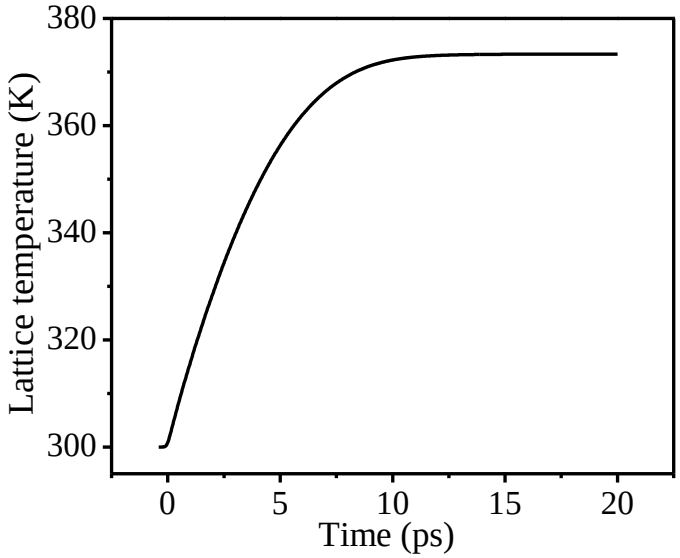

Fig. A.2 Reproduction of Electron and lattice temperature relaxation at the surface of 20 nm Au sample after [132]. The following material parameters are used: R=0.408, 1/a = 15.328×l0^{-9} m, G = 2×1016 W/m^{3}K, K=318 W/mK, Ae=67.96 mJ/cm^2, and 0.49 mJ/cm^2 absorbed fluence.

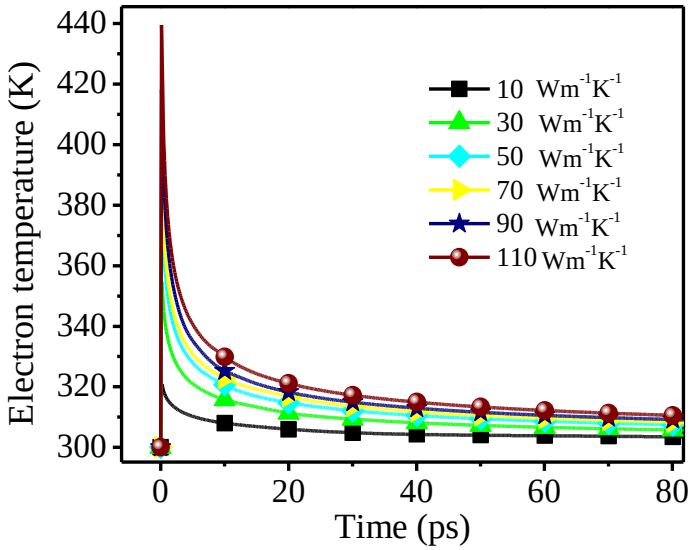

Fig. A.3 Electron temperature relaxation simulation at the surface of 1 µm Nb sample. The thermal conductivity varied from 10 to 110 $Wm^{-1}K^{-1}$ all other material parameters are obtained from reference [108].

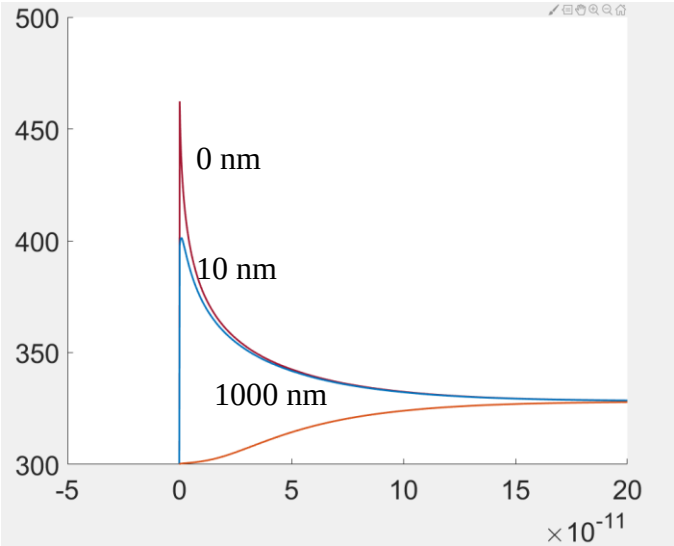

Fig. A.4 Electron temperature relaxation for different thickness of Nb thin film. The material parameters are used from reference [108].

LabVIEW data acquisition

The LabVIEW program is used to control the stage and the lock-in-amplifier simultaneously. The main two section of the operations are

1. The stage control:
2. Data acquisition from the lock-in-amplifier

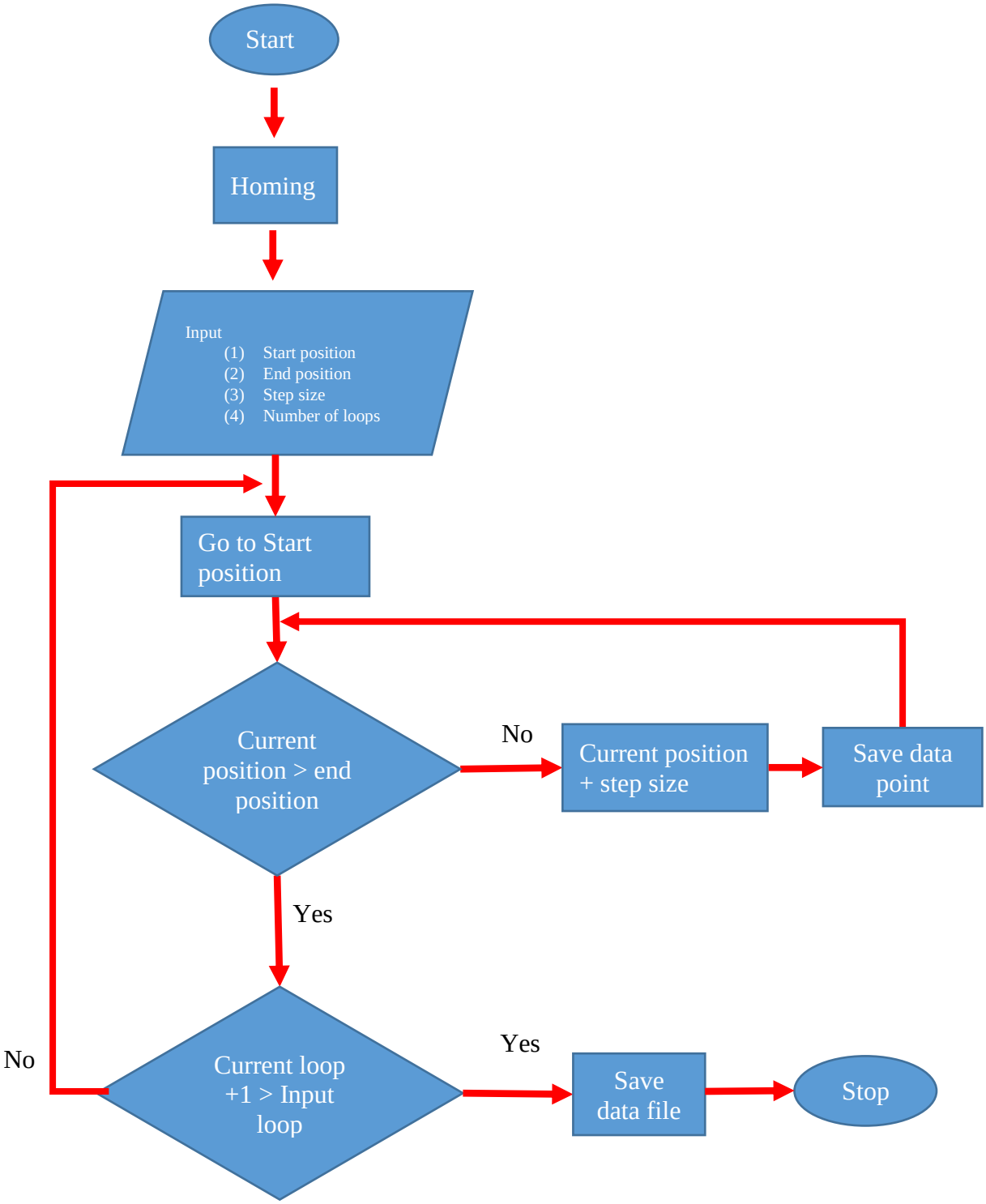

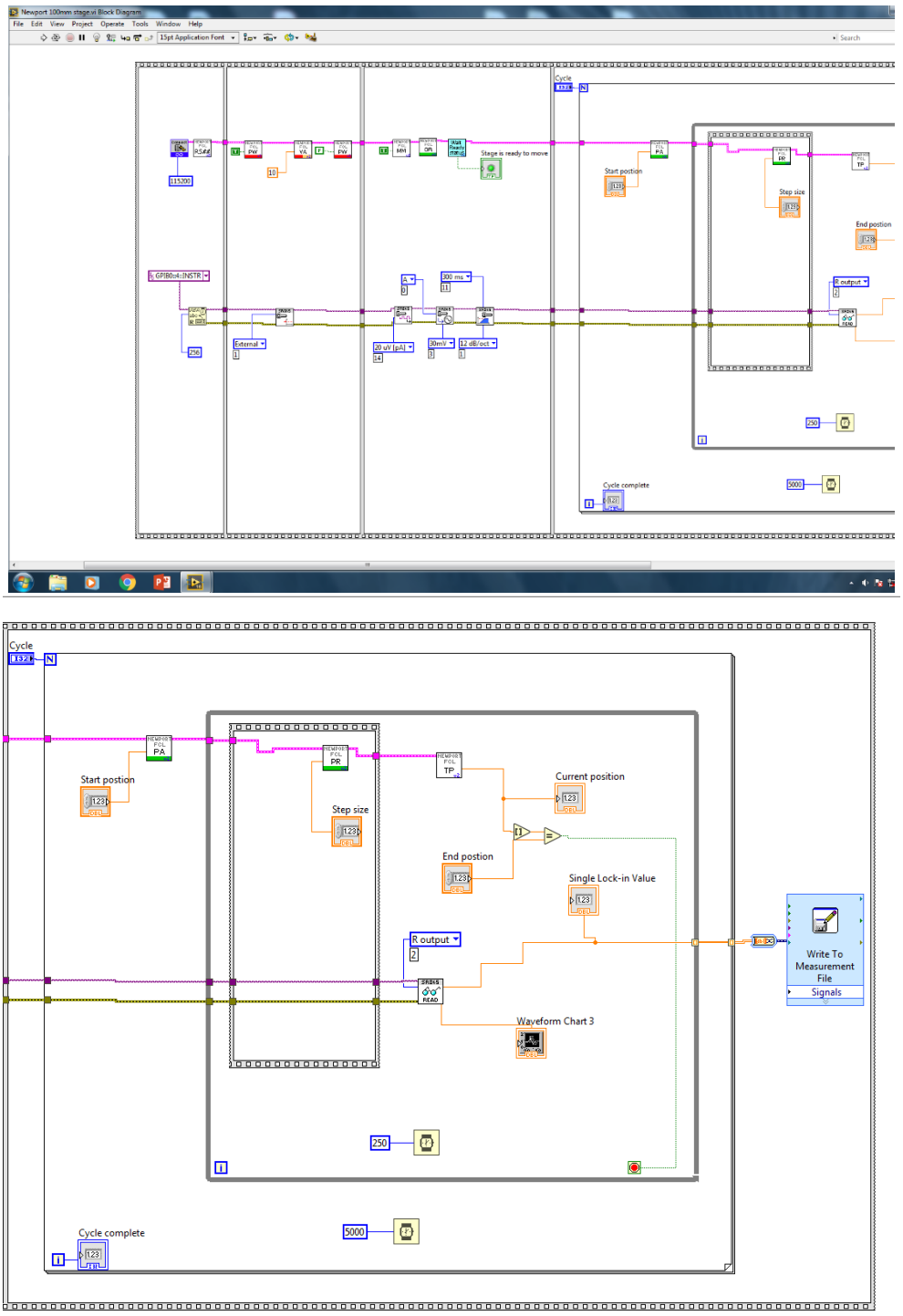

Fig. A.5 LabVIEW program: FLC 100 Newport corporation 100 mm stage control.

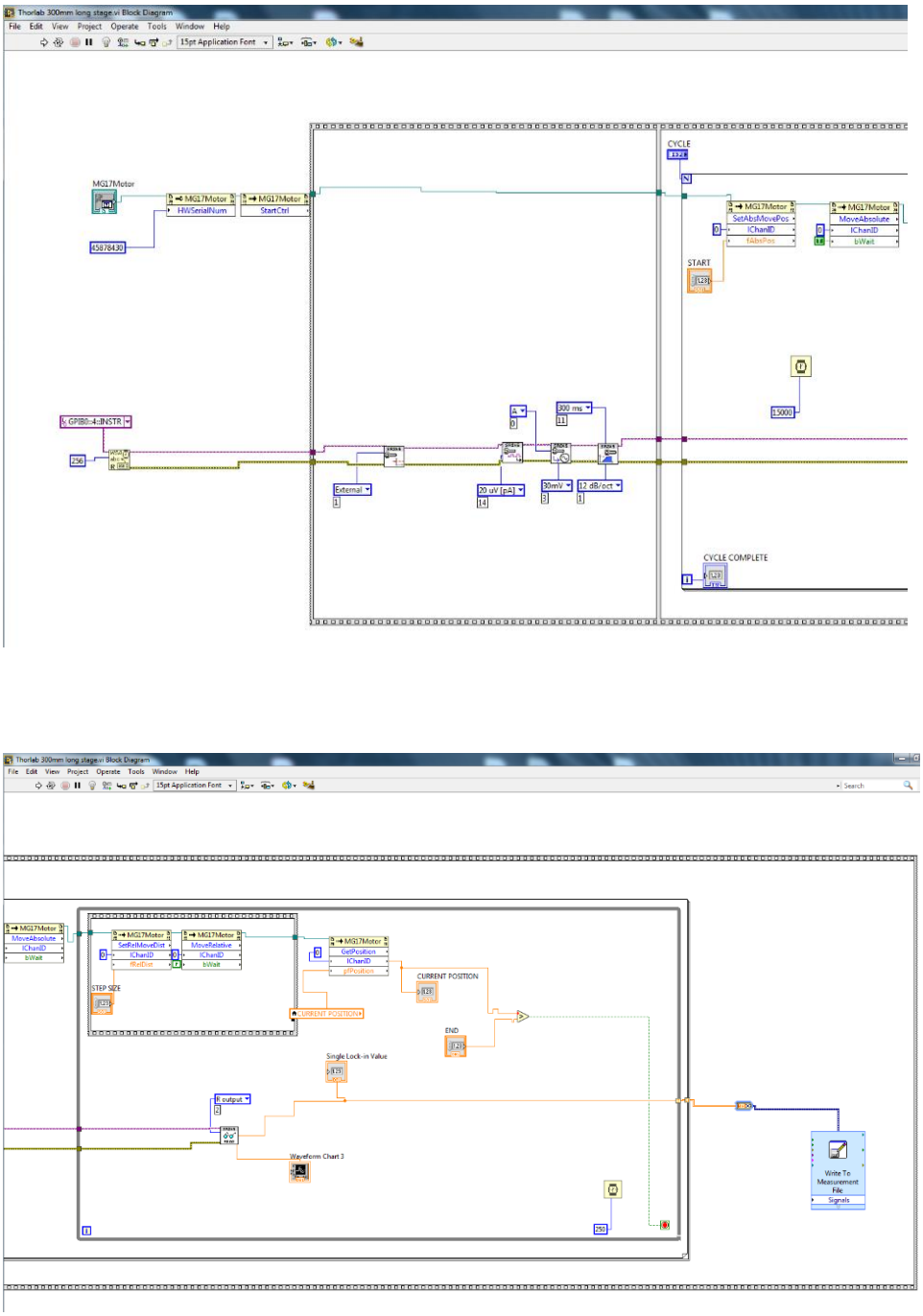

Fig. A.6 LabVIEW program: Thorlab 300 mm stage control.

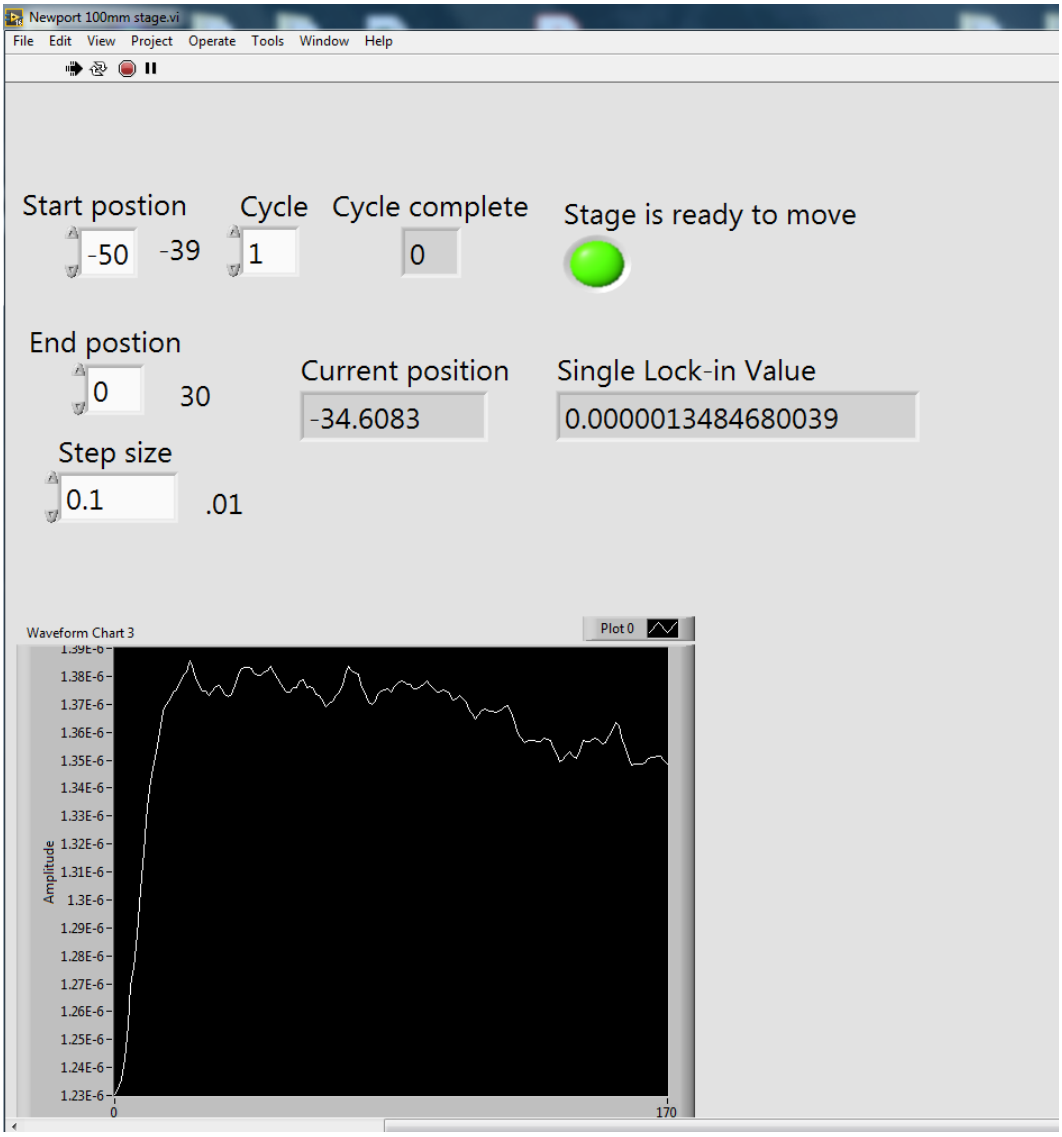

Fig. A.7 the front panel of the LabVIEW data acquisition program.

APPENDIX B

CONSTRUCTION OF PUMP-PROBE EXPERIMENTAL SETUP

Laser turn-on procedure

1. Make sure the laser power supply is on. After turning on the power supply, it should take 20~30 min to warm up the system.

2. Turn on the chiller for the Millennia green pump laser. The chiller temperature should be at 23° C.

3. Turn on the chiller for the Tsunami oscillator. The chiller temperature should be 17° C.

4. Press the “laser power” button to start the warm-up process. The warm-up time bar will appear on the “main” screen. It should take 5~10 min to warm up.

5. When the warm-up process is completed, go to the “setup info” menu.
   The mode > power.

6. Long press the “Power” button to start the lasing. The “laser Emission” sign will turn on. The laser on the sign will light up on the millennia. The laser power will gradually increase up to the set power.

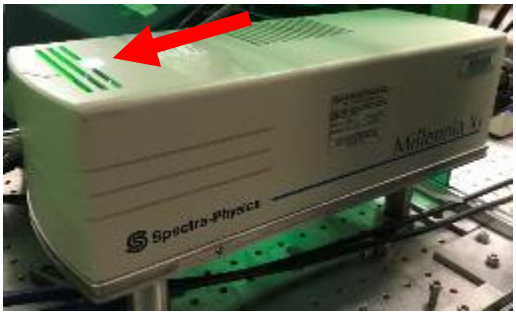

7. The laser power can be set in two different setpoints P1 and P2. To change the laser output power change the P1 or P2 set. Open the shutter when required.

Mode-locking Procedure

1. Keep the laser on for 30 min.
2. Measure the output power. The output power should be more than 850 mW. Check the optical spectra. A narrow optical line should appear around 780 nm.

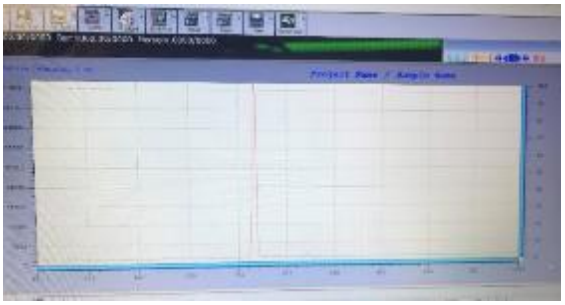

3. Use the two-control knob in the middle portion of the Tsunami to achieve the mode lock. The top and the bottom knobs are used to control the slit and the prism, respectively. A small vibration in the prism is required to achieve lock mode.

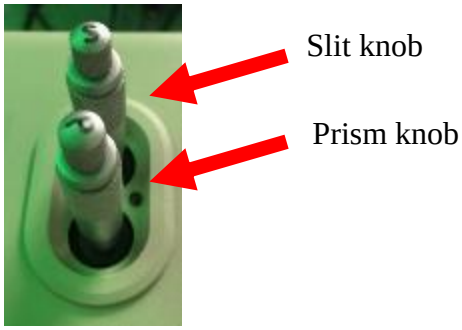

4. Keep both the prism and slit knob around 7 mm. Now quickly change the prism knob position to the forward or backward direction ± 1 mm. The lock mode should be achieved. The spectrum will be broadened.

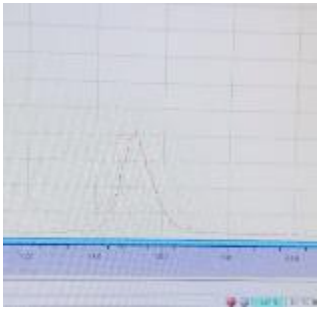

Alignment of acousto-optic-modulator

1. Mount the acousto-optic-modulator so that the rotation and X-Y movement is available.
2. A beam expender can be used inversely to reduce the beam diameter at 2 mm. The smaller beam diameter is required for better efficiency of the acousto-optic-modulator.

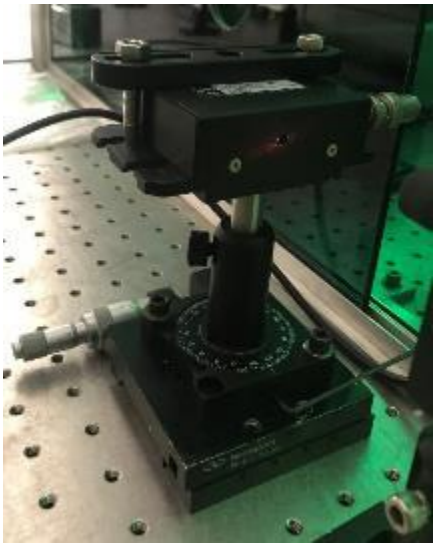

3. Connect the RF power supply and the signal generator.
4. Turn on the RF power supply. Increase the power to "level 8". Keep the signal generator off.

5. Change the X-Y position of the modulator head if required. The fundamental beam should appear along with 1st, 2nd or even higher order harmonics. Carefully rotate the modulator head clockwise and anticlockwise to increase the intensity of the 1st order beam compared to the fundamental.

6. Use an iris to block all other beams except 1st order harmonics.
7. Turn on the signal generator and change the RF power level to adjust the modulation depth.

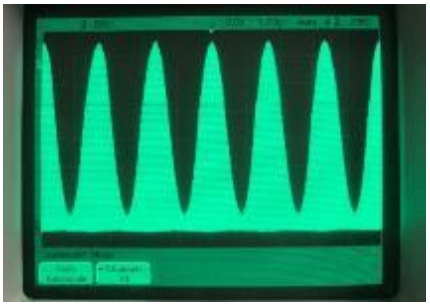

Linear Stage alignment

1. The beam profiler is used to detect the beam movement in the near and far end of the stage.

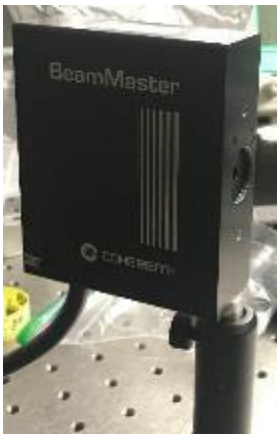

2. The stage needs to be inspected before mounting. An extra base is required for some stages for proper alignment.
3. The retroreflector mirror is used on the stage to make the in and outgoing beam almost perfectly parallel (1 arcmin).
4. First, the beam movement in the X direction is adjusted by changing the X position of the mirror in from of the retroreflector.
5. Then the beam movement in the Y direction is adjusted by X position in the same mirror.

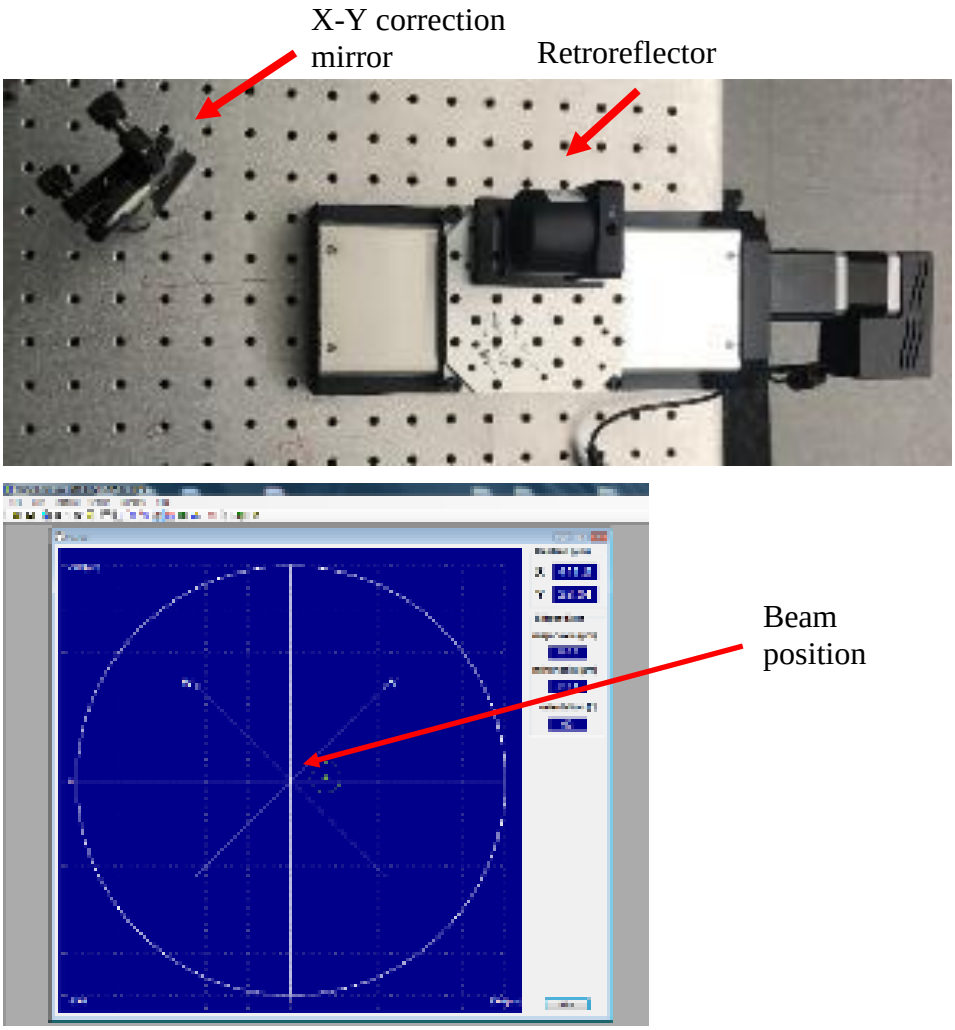

6. The maximum shift in the beam is achieved up to ± 5 µm

Pump and probe beam overlapping

1. A camera with a zoom lens is used to ensure the overlapping of the pump and the probe beam.
2. Make the pump and probe beam perfectly parallel in the far end by using two mirrors and two iris in the probe line. Use first mirror to center the beam to the first iris and second mirror to center the beam to the second iris.
3. Put the lens or the sample on a linear stage.
4. Block the pump beam. Move the lens or the sample until the probe beam size is at its minimum.
5. Unblock the pump. The pump and probe should be very close to each other.

6. Try to overlap the pump and the probe by changing the position of the polarized beam splitter.
7. For very fine tuning of the beam overlaping, slightly change the lens or sample position.

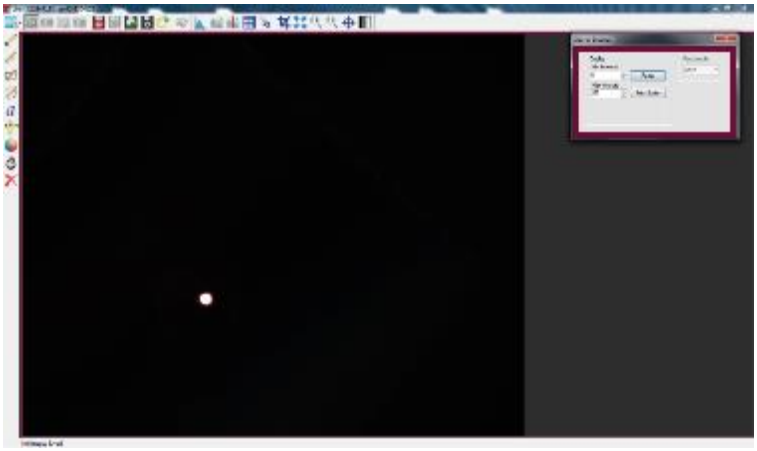

Signal detection and lock-in-amplifier

1. The ΔR signal is in order of 10^{-6} range. To detect the signal the strength of the pump and probe beam is very important. Measure the voltage of the probe beam using an oscilloscope.
2. A glass slide can be used to check the saturation of the signal if the signal is too high. Glass slides usually cut 10% of the power

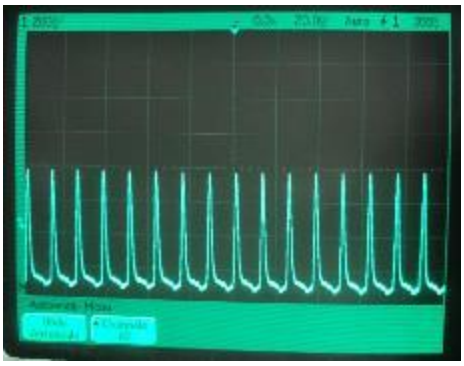

3. The ΔR is observed between 10^{-6} to 10^{-8} for any type of samples. The different variables of the lock-in-amplifier are also very important to detect a clear signal The parameters are given in the table below.

Table B.1 general parameter for the operation of lock-in-amplifier

Minimum probe voltage	12 mV (rms)
Maximum probe voltage (signal saturate)	300 mV (rms)
Sensivity	20 µV
Time contant	300 ms
Input range	10 mV
Filter	12 db
Current	1 µA
External Trigger	600 kHz

APPENDIX C

THERMAL CONDUCTIVITY MEASUREMENT OF Nb THIN-FILM

X-ray diffraction (XRD) pattern of Nb on sapphire is shown in Fig. C.1. A polycrystalline 1-μm Nb film, with a highly oriented (1,1,0) plane, is deposited on sapphire substrate by magnetron sputtering. A weak Nb (2,2,0) peak is also observed. The crystallite size of Nb (1,1,0) is calculated as 17.6 nm using the Debye-Scherrer equation. The transient signal (ΔR) is collected using the lock-in-amplifier. The ΔR is divided by the static DC signal (R) from the photodiode to eliminate any dependence of the final signal on the intensity or size of the probe beam. The normalized $\Delta R/R$ is shown in Fig. C.2. The values of the parameters in Table C.1 are used to measure the thermal conductivity (K) by curve fitting to the 1D heat diffusion equation C.1.

$$C\frac{\partial T_{(x,t)}}{\partial t} = -K\frac{\partial^2 T_{(x,t)}}{\partial x^2}) + I(1-R).\alpha.exp(-\alpha x)\,exp(t/\tau)^2 \qquad \text{C.1}$$

The experimental result is fitted with the 1D heat equation to determine the thermal conductivity as 54 ± 2 $Wm^{-1}K^{-1}$. The data is fitted after 50 ps as the heat propagation mostly depends on the diffusion process. Physical constants of Nb are used in the calculations [108]. Reflectivity (R) = 0.9, radiation penetration depth (d) = 15.3 nm, initial temperature (T_0) = 300 K, lattice heat capacity (C) = 2.3 × l06 J/m^3K.

Table C.1 Physical constants of Nb used in calculations [108]

Reflectivity (R)	0.9
Radiation penetration depth (d)	15.3 nm
Initial temperature (T_0)	300 K
Lattice heat capacity *(C)*	2.3 × $l0^6$ J/m^3K

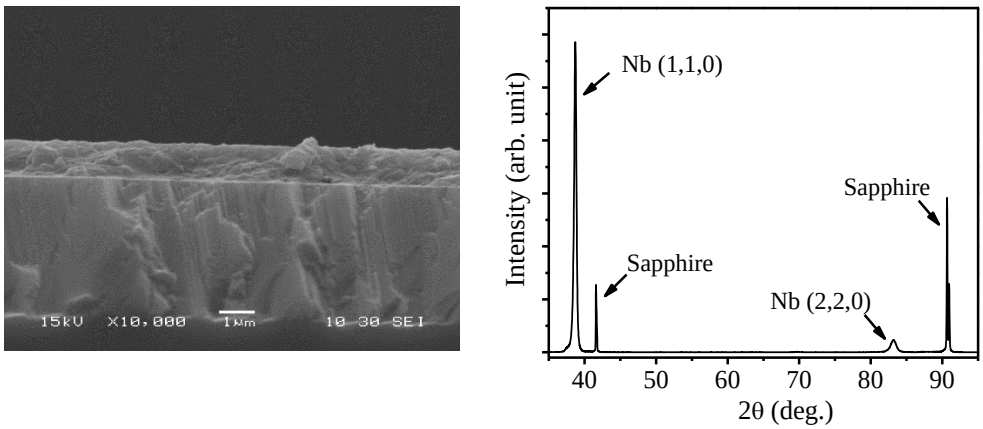

Fig C.1 (a) XRD pattern of 1 μm Nb film on the sapphire substrate. (b) The thickness of the thin film is confirmed by SEM.

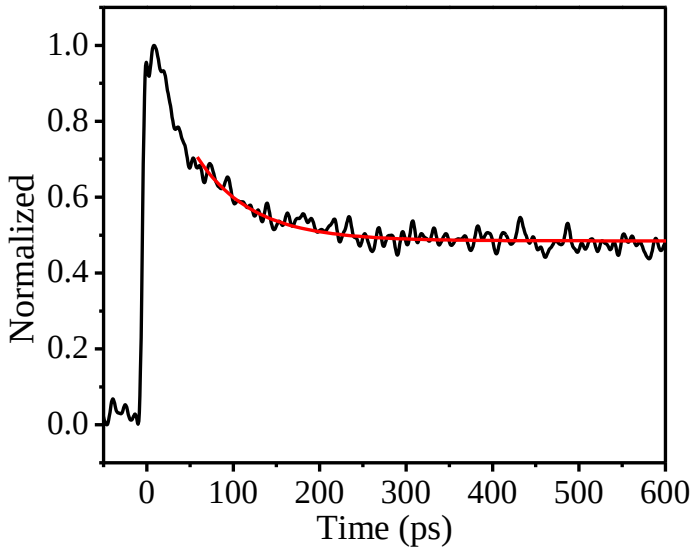

Fig. C.2 The normalized change in thermoreflectance of a 1 μm Nb on sapphire. The experimental result is fitted with the 1D heat equation to determine the thermal conductivity as 54 ± 2 $Wm^{-1}K^{-1}$.

APPENDIX D

TEMPERATURE DEPENDANCE THERMAL CONDUCTIVITY MEASUREMENT OF INGOT NIOBIUM

cryogenic chamber is used to measure the temperature-dependent thermal conductivity of Nb shown in Fig.D.1. A closed-loop He cooled cariogenic chamber is used to cool down the Nb sample. The roughing and thermomolecular pump are used to vacuum the system up to 10^{-6} torr. The minimum temperature recorded from the cryogenic system is 6 K. However, no thermoreflectance measurement is conducted at 6 K due to the vibration of the cryogenic chamber. Helium compressor is turned off to avoid the vibration the and the thermoreflectance result is collected at 70 K where the temperature drop is much slower compared to at 6 K. Fig. D.2 shows that no significant change in the slop of the $\Delta R/R$ is observed. According to the previous reports the thermal conductivity of Nb is 55 ± 5 $Wm^{-1}K^{-1}$ in the range of 10 to 300 K. A significant rise in thermal conductivity is reported around 6 K which is the critical temperature of Nb.

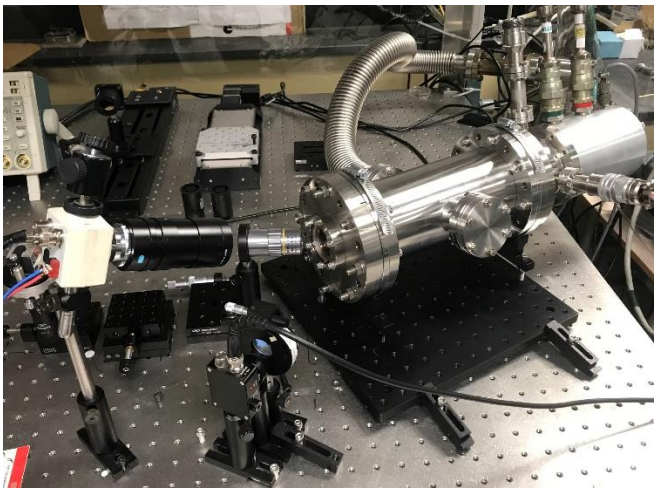

Fig. D.1 Cryogenic chamber for temperature dependence thermal conductivity measurement.

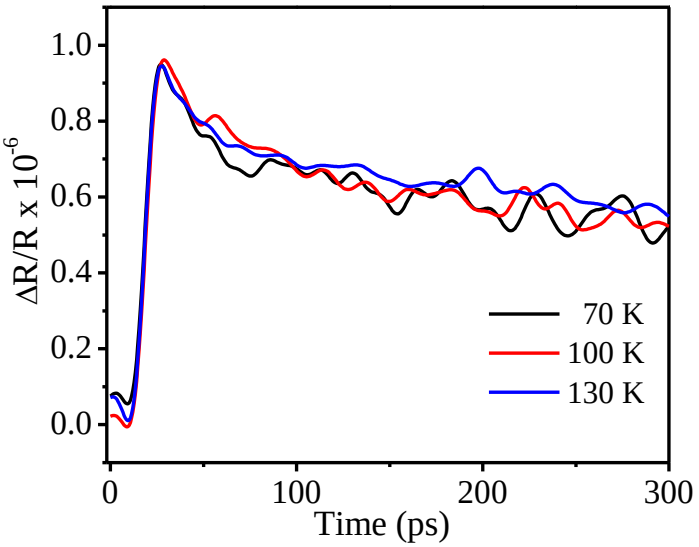

Fig. D.2 Temperature dependence of the thermoreflectance measurement of ingot Nb.

APPENDIX E

THE LIST OF PARTS IN PUMP-PROBE EXPERIMENTAL SETUP

Item	Qty	Part Number	Description	Company	Link	Unit price	Price
1	1	AOM-402AF3	MODULATOR	Intra action		$832.00	$832.00
2	1	ME-403	ME-403 MODULATOR DRIVER	Intra action		$1013.00	$1013.00
3	1	GBE03-B	3X Achromatic Galilean Beam Expander, AR Coated: 650 - 1050 nm	Thorlabs	https://www.thorlabs.com/thorproduct.cfm?partnumber=GBE03-B	$494.70	$494.70
4	1	MY10X-803	MY10X-803 - 10X Mitutoyo Plan Apochromat Objective, 0.28 NA, 34 mm WD	Thorlabs	https://www.thorlabs.com/thorproduct.cfm?partnumber=MY10X-803	$890.46	$890.46
5	2	DET10A2	Si Detector, 200 - 1100 nm, 1 ns Rise Time, 0.8 mm2, Universal 8-32 / M4 Mounting Holes	Thorlabs	https://www.thorlabs.com/thorproduct.cfm?partnumber=DET10A2	$159.12	$318.24
6	1	BSN11	Ø1" 10:90 (R:T) UVFS Plate Beamsplitter, Coating: 700-1100 nm, t = 5 mm	Thorlabs	https://www.thorlabs.com/thorproduct.cfm?partnumber=BSN11	$120.36	$120.36
7	1	LPNIRE100-B	Ø1" Linear Polarizer with N-BK7 Windows, 600-	Thorlabs	https://www.thorlabs.com/thorproduct.cfm?partn	$112.20	$112.20

			1100 nm		umber=LPNIRE100-B		
8	1	PBS252	1" Polarizing Beamsplitter Cube, 620 - 1000 nm	Thorlabs	https://www.thorlabs.com/thorproduct.cfm?partnumber=PBS252	$222.36	$222.36
9	1	XYF1 - XY	XYF1 - XY Mount for 1" - 3" Rectangular Optics, 8-32 Taps	Thorlabs	https://www.thorlabs.com/thorproduct.cfm?partnumber=XYF1	$345.00	$345.00
10	2	HRS1015-AG	1" x 1" Hollow Roof Prism Mirror, Ultrafast-Enhanced Silver	Thorlabs	https://www.thorlabs.com/thorproduct.cfm?partnumber=HRS1015-AG	$333.54	$667.08
11	2	WPH10E-780	WPH10E-780 - Ø1" Polymer Zero-Order Half-Wave Plate, 780 nm	Thorlabs	https://www.thorlabs.com/thorproduct.cfm?partnumber=WPH10E-780	$276.42	$552.84
12	1	GBE02-B	GBE02-B - 2X Achromatic Galilean Beam Expander, AR Coated: 650 - 1050 nm	Thorlabs	https://www.thorlabs.com/thorproduct.cfm?partnumber=GBE02-B	$411.06	$411.06
13	8	UM10-AG	UM10-AG - Ø1" Ultrafast-Enhanced Silver Mirror, 750 - 1000 nm	Thorlabs	https://www.thorlabs.com/newgrouppage9.cfm?objectgroup_id=8159	$98.94	$791.52
14	1	UGP-1	Ultima Gimbal Prism Mount, 1 in., 100 TPI Adjustment Screws	Newport	https://www.newport.com/f/gimbaled-three-axis-optic-tilt-mount	$331	$331

APPENDIX F

SPUTTERING SYSTEM OPERATION

Operating procedure of sputtering system:

1. Sample loading:

    a. Clean the substrate holder with ethanol and clean it properly.
    b. Ensure your gloves are clean.
    c. Select 4” or 6” substrate holder keeping in mind that 4” holder can be heated up to 850°C while 6” holder can be heated only up to 400° C.
    d. Clean the screw and clips by ultrasonic cleaner for 5 min.
    e. Mount the substrates using screws and clips. To avoid contamination, do not touch the substrates with hands, handle with tweezers.

2. Transferring the Substrate to Chamber

    a. Ensure the substrate transfer door is open. Always place the door with O-ring facing up to avoid damaging it.
    b. Hold the substrate holder plate from the edges with your right hand. The substrate should be facing your palm but not touching.
    c. Turn the plate over with substrate facing down now and transfer through the substrate mounting door.
    d. Raise it against the propeller in the center of the quartz plate and turn the propeller clockwise with your left hand by turning the motor shaft on the top lid. This will engage the propeller in the grooves on the back of the substrate plate.
    e. Ensure the substrate plate is held securely before removing your hand

3. Pump Down process

a. Close the top lid gently using the handle and tighten the screw.
b. Close the side door.
c. Ensure the nitrogen pressure valves are off. Fig. F.1
d. Ensure the argon pressure valves are off. Fig. F.2
e. Ensure the vent valve is off. Fig. F.3
f. Ensure gas1 shutter is off. Fig. F.4
g. Ensure the turbo isolation valve is fully open. Fig. F.5
h. Turn the pump on/off switch to ON. Fig. F.6
i. Watch the turbo speed going up on its controller. It should reach 100%. If it does not turn the pump switch off and let the staff know.

4. Deposition rate measurement process

a. Change the crystal of the thickness monitor if necessary.
b. Press program >Next> (set up density with control knob) > next > (set up Z value with control knob) > Press Program for main menu.
c. Make the substrate holder higher.
d. Put the crystal in the middle of the substrate holder.

5. Deposition process:

a. Make sure that the power supply relates to the right gun.
b. Open the argon cylinder pressure valves. Fig. F.9
c. Open the gas shutter. Fig. F.11
d. Select the 1st nob. Fig. F.12
e. Pull the nob and rotate fully clockwise to make the gas pressure maximum. Fig. F.13
f. Make the turbo gate valve nearly close to increasing the pressure to 3×10^{-2} torr to generate plasma.
g. Set up the power rotating the nob of the power supply.

h. Turn on the power supply. Fig. F.14

i. Change the pressure back to working pressure 3×10^{-3} torr. Fig. F.15

6. Venting the Chamber:

a. All gases and plasma must be off before attempting to vent the chamber.

b. Ensure turbo-isolation valve is open

c. Ensure the ion gauge is off

d. Open the nitrogen pressure valve

e. Turn the pump switch off to turn off the turbo and backing pump.

f. When the turbo stops spinning the chamber vent valve can be slowly opened to speed up venting.

Pump down process

Fig. F.3 N_2 gas valve off

Fig. F.1 Ar gas valve off

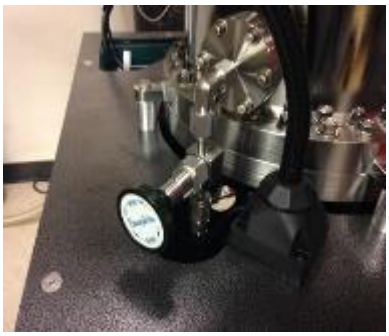

Fig. F.2 Ar Vent valve off

Fig. F.4 Gas shutter off

Fig. F.6 MFCX off

Fig. F.5 Turbo gate valve open (fully)

Fig. F.7 turn on the turbo pump

Fig. F.8 Frequency of the turbo pump should reach 963 Hz

Deposition process

Fig. F.11 lower Substrate for deposition

Fig. F.10 Ar gas valve on

Fig. F.9 Gas shutter on

Fig. F.14 MFCX on

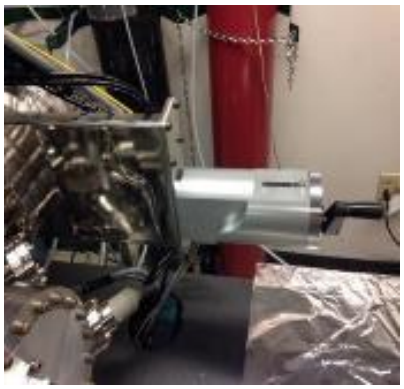

Fig. F.13 Change pressure to 3×10^{-2} torr by changing gate valve position

Fig. F.12 Set the power

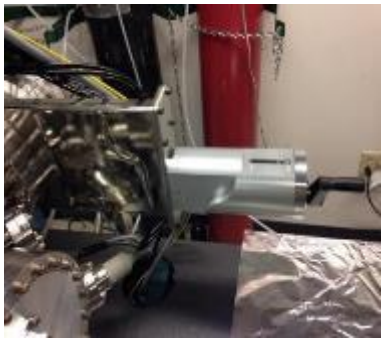

Fig. F.17 Change pressure to 3×10^{-3} torr by changing gate valve position

Fig. F.15 Open the shutter of appropriate gun

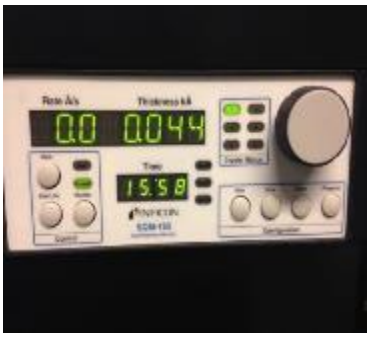

Fig. F.16 Set time to zero thickness monitor

APPENDIX G

LASER INTERLOCK SYSTEM

The laser interlock system in ESB laser lab ODU is consists of 5 different components

1. The laser interlock system board ICS 6
2. Shutter LS-10
3. Interlock override switch
4. Access keypad (Ics-KP12)
5. ICS-6 Illuminated Sign

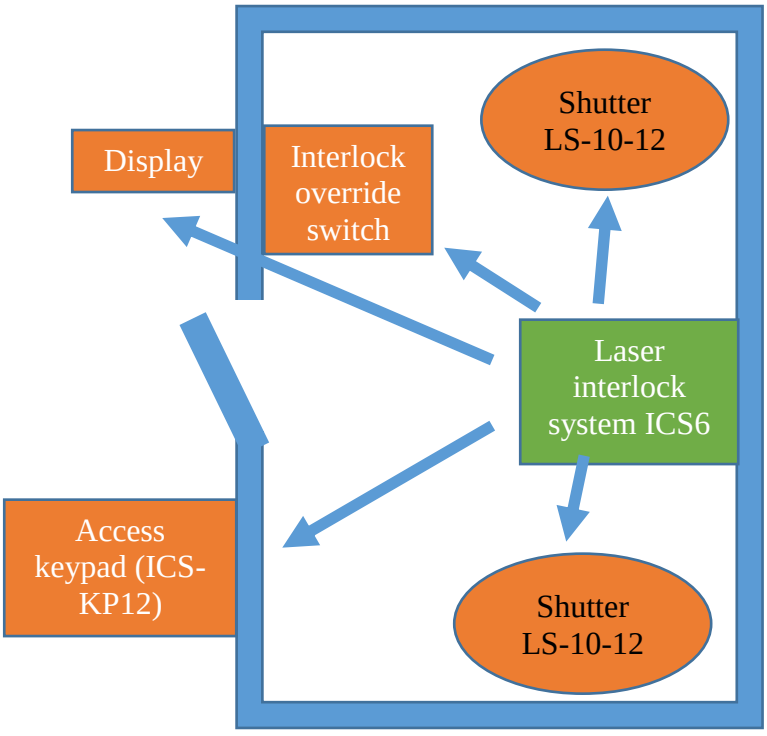

Fig. G.1 Schemeics ODU ESB laser interlock system.

The laser interlock system board ICS 6

The laser interlock system board monitors the signal from different switches. The detail description of the indicators is discussed in this section. The instructions are collected from the ICS 6 manual.

LED indicators

"Interlock LED's are provided for each of the four Interlock Monitors. Each pair refers to an interlock switch it could be a shutter or door magnet. For each Interlock, a pair of yellow LEDs' indicate that the interlock is open. The left-hand LED indicates the 'A' contact, the right-hand LED indicates the 'B' contact. If the contact is not used and a wire link has been fitted, the corresponding LED will not illuminate. If both 'A' and 'B' contacts are fitted and it is observed that one LED is on and the other off, this indicates a fault which will be detected by the mismatch detector if it is enabled."

Fig. G.2 The laser interlock system board ICS 6.

Mismatch detector

“The ICS-6 trips out and disables the interlock when either of its two safety circuits opens. Also, the emergency stop button can trigger the mismatch detector. A mismatch is triggered, and the mismatch fault light illuminates on the front panel when the second safety circuit does not open within a short time of the first (typically around 1 second). It is not possible to arm the system if the mismatch fault occurs. The restart is required to remove the mismatch fault.”

Arm button (illuminates blue)

“The Arm button will illuminate when both safety circuits are complete, and all output devices are detected as being in a safe condition. This indicates that the ICS-6 is ready to be armed. If both Safety Circuit Complete lights are lit but the button is not illuminated, this indicates that one or more output devices are not detected in the safe condition.”

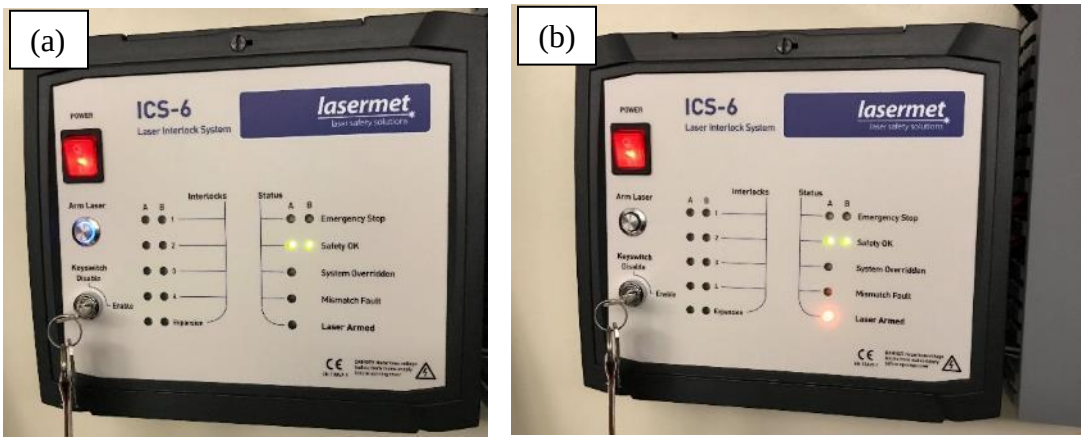

Fig. G.3 (a) The system is ready to arm. The blue LED is on. (b) The laser is armed by pressing the arm button. The laser arm LED is on.

Laser armed LED

“When the 'Safety Circuit Complete' LED has lit and the Arm Laser button has been pressed, the 'Laser Armed' LED will light orange to warn that the ICS-6 has enabled the laser. If the ‘Safety Circuit Complete’ LED is illuminated but the ‘Laser Armed’ LED does not illuminate when the

Arm Laser button is pressed, this could indicate that the internal checking circuitry of the ICS-6 has detected a fault condition."

Emergency stop

"The emergency stop led to indicate the emergency stop button is pressed for any of the shutter"

System override

"System override led indicates the system is overwritten either by internal or external override switch/keypad."

1. **Beam blocking shutters**

"The ICS-6 may operate one or more beam shutters and one or more laser interlocks. For permanent fixed installations these may be directly wired to the ICS-6. Where there is any possibility of the equipment being changed or moved it is often most convenient to be able to unplug the equipment.

When the power supply to pin 1 of the shutter comes on, the middle yellow LED will light. The green LED will also light indicating that the shutter is closed. Pressing the green button momentarily will open the shutter. The Orange LED will light indicating that the shutter is open, and the beam is exposed. To manually close the shutter, press the red button. Loss of power to the shutter, such as when a door interlock switch trips the interlocked power supply, will also cause it to close."

Fig. G.4 Laser shutter.

2. **Override switch**

“Lasermet override board allows an interlocked door to be opened for a short time without interrupting the laser. When the override is activated a warning, the indicator is shown on the ICS-6 and a buzzer sound. The override is time-limited, and the duration of override can be adjusted between 6 and 27 seconds by adjusting the potentiometer marked R19, on the Override board.

Fig. G.5 (a) Override keypad outside laser lab. (b) override switch inside laser lab. Both are used to temporarily override the laser interlock for 10 sec.

3. Override entry keypad

"The Lasermet ICS-KP12 is an entry keypad with built-in fail-safe override timer. It may be used either as a key-coded override control, as a door release where door locks are used, or both. The keypad is usually fitted adjacent to the entry door on the outside of the controlled area, and a door release exit button is provided on the inside which activates the keypad remotely."

Fig. G.6 Illuminated indicator outside the room.

4. ICS-6 Illuminated sign

“If the output LS-10 shutters or contactors are closed that prove that it is a safe condition. The sign control show “no hazard laser off”. The sign control will revert to the ‘Danger’ laser-armed indication if these devices are not in the safe condition or they are removed from the system.”

Starting up

1) Set the mains switch on the unit to ‘1’.

2) Insert the key into the interlock key switch and turn to the right, ‘Enable’.

3) Close all interlocked doors. The LED’s on the front panel will indicate yellow if the corresponding door is open.

4) Check any Emergency Stop buttons are released- if any have been pressed the emergency stop lights will illuminate yellow.

4) The 'Safety Circuit Complete' LED’s will light green and the Arm laser illuminates blue.

5) When you are ready to operate the laser, press the Arm Laser button.

Resuming operation after an interlock switch has been opened

When any interlocked door is opened or the emergency stop button is activated, the ICS-6 will cut the power to the laser or the shutters. To resume laser operation:

1) Close all interlocked doors (where necessary). Note LED state on the front panel.

2) Reset the emergency stop button (where necessary).

3) When ready to restart, press the ICS-6 Arm Laser button.

Using the override

The override facility, where fitted, allows interlocked doors to be opened for a short time without the laser being interrupted.

1) To activate the override with a push button, simply press the button on the push-to-exit switch. The system will now go into override mode for a short time, and a buzzer will sound.

2) To activate the override externally with the use of an ICS-KP12 keypad simply type in the user’s 4-digit code (**default is 3333**) the system will now go into override mode for about 15 seconds. If there is a magnetic lock on the door this typically will be released for 5 seconds.

APPENDIX H

UNPUBLISHED DATA

In-situ ΔR/R response measurement of Al on Si. Thermal evaporation is used to deposit the film. The deposition parameters are: input voltage on variac 12 V, deposition rate approximately ~ 12.5 nm/min, the

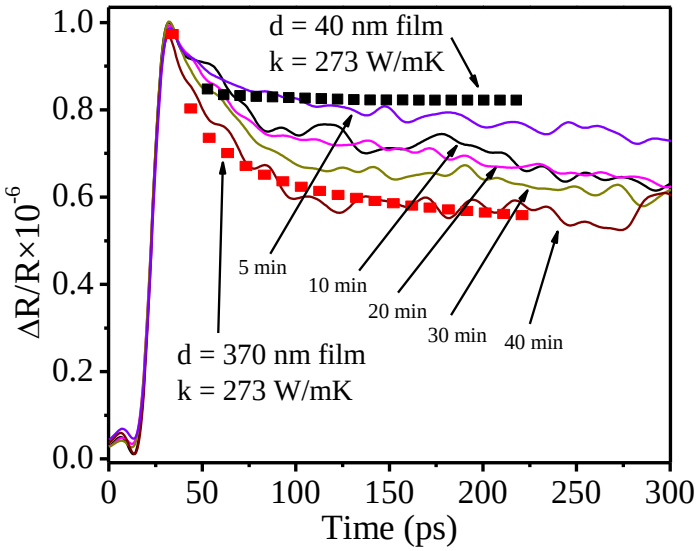

Fig. H.1 *In-situ ΔR/R* response measurement of Al on Si. Thermal evaporation is used for 0 to 120 min.

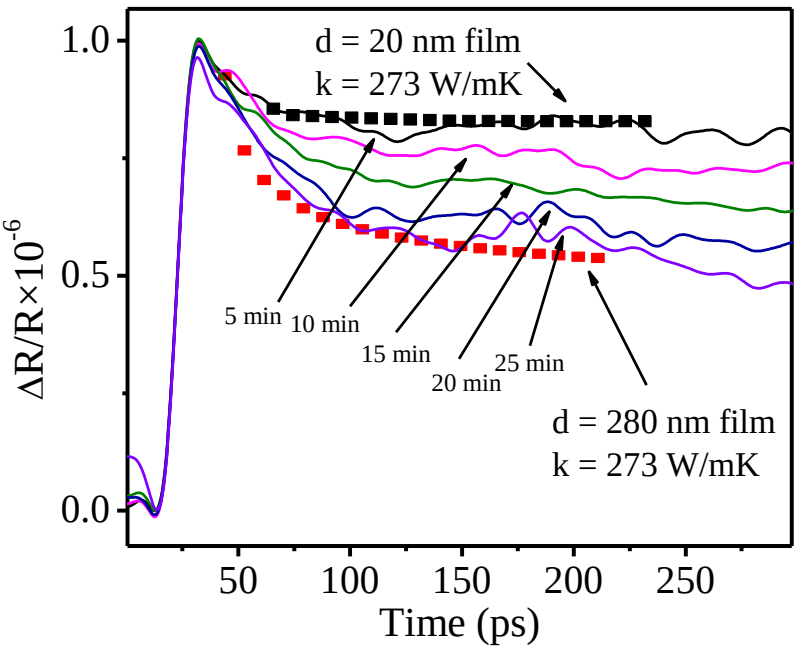

Fig. H.2 *In-situ ΔR/R* response measurement of Al on Si. Thermal evaporation is used for 5 to 25 min.

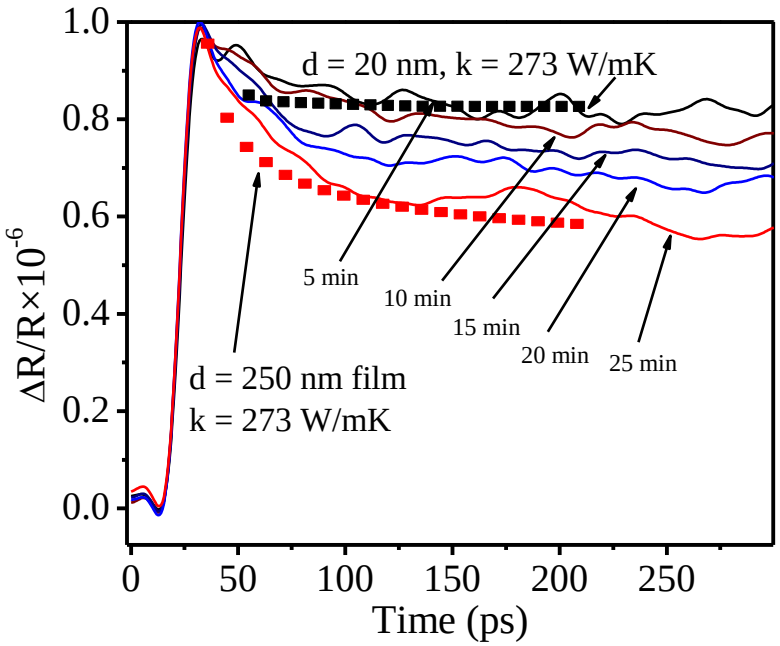

Fig. H.3 *In-situ ΔR/R* response measurement of Al on Si. Thermal evaporation is used for 5 to 25 min.

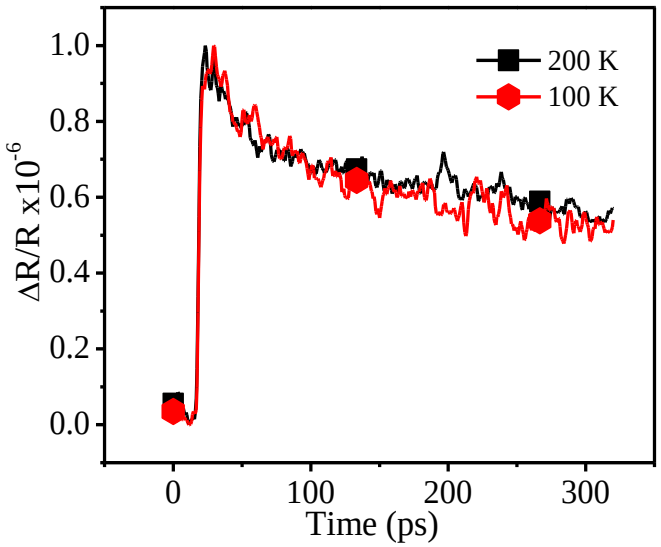

Fig. H.4 *ΔR/R* response of ingot Nd at different temperature.

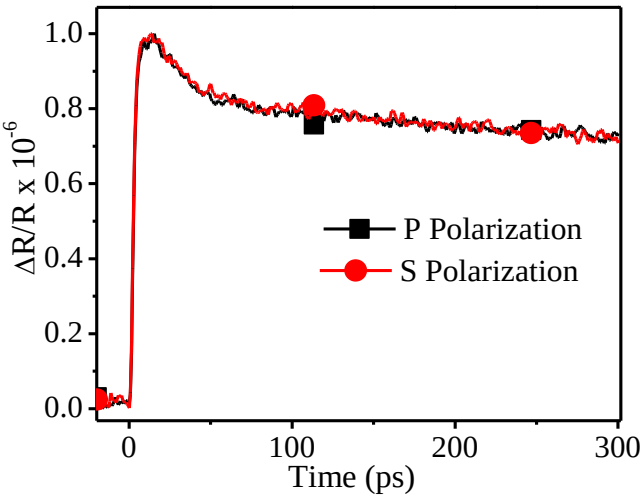

Fig. H.5 *ΔR/R* response of ingot Nd for different polarization of pump beam. No significant difference is observed.

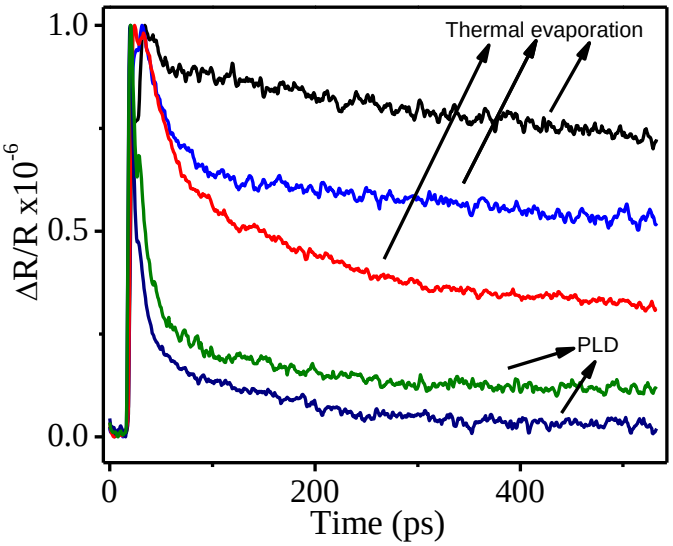

Fig. H.6 Comparison between *in-situ* measurement of ΔR/R from the thermal evaporation and PLD generated thin film.

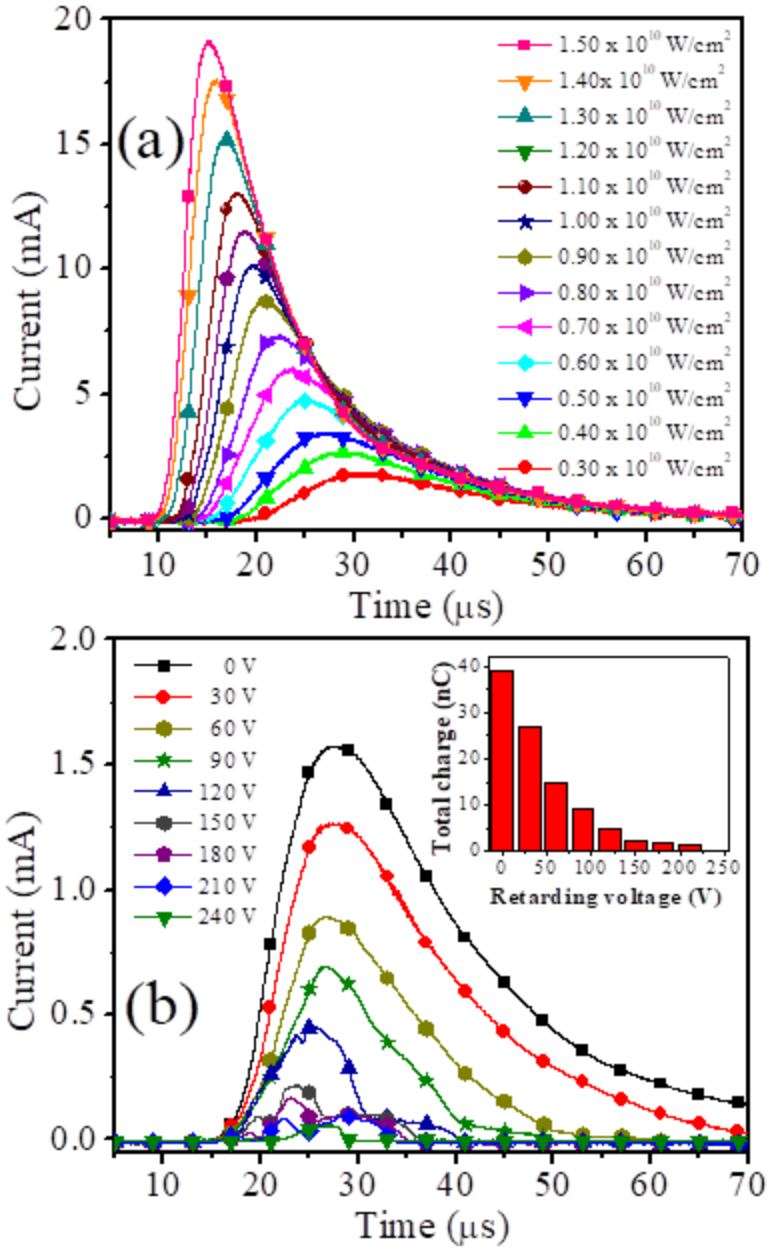

Fig. H.7 (a) The time of flight signal for various laser intensity (b) time of flight signal for Al ions, passing a retardation potential of 240V for a laser intensity of 3×10^9 W/cm^2.

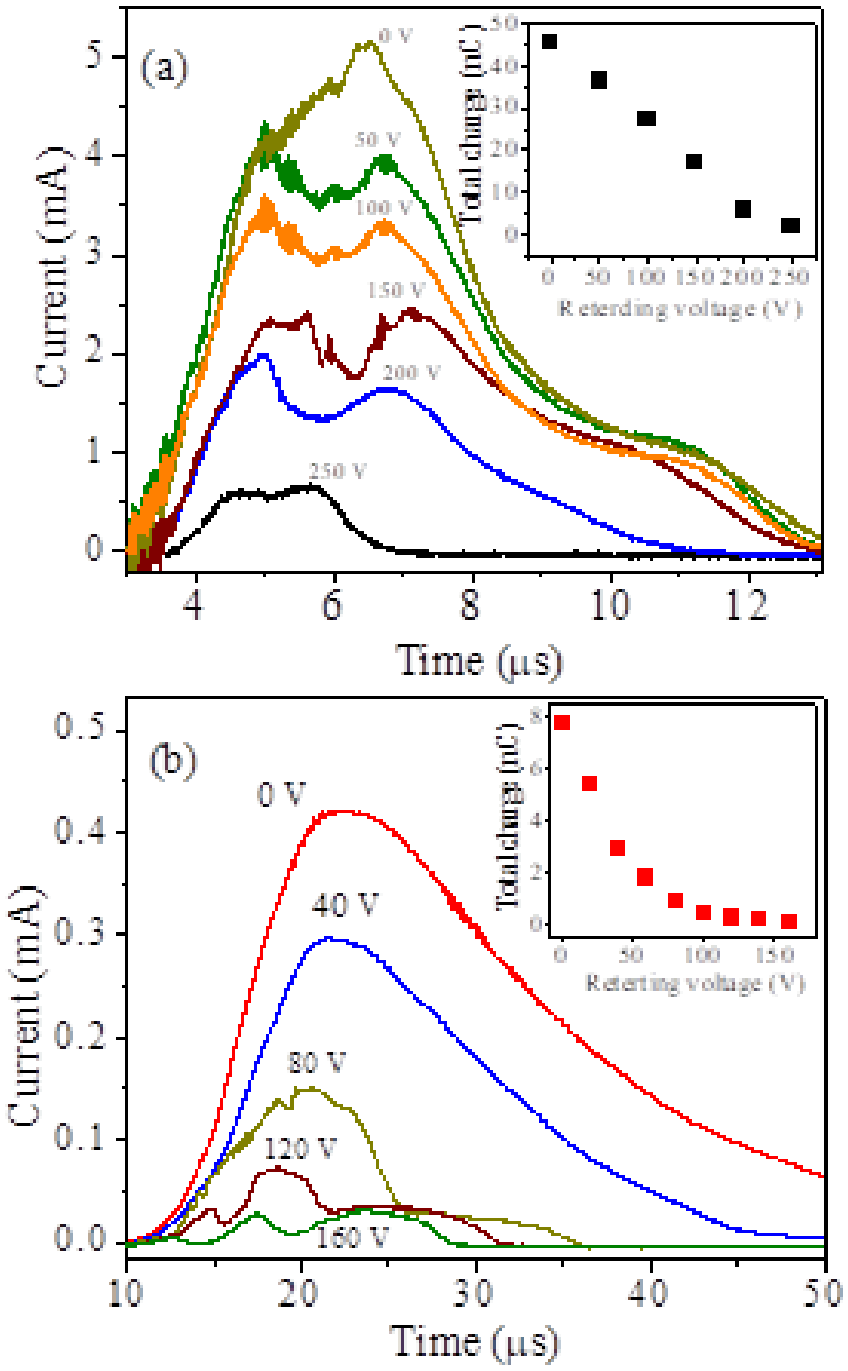

Fig. H.8 The ion retardation for spark-discharge and without spark discharge. (a) For 1.2 J spark-discharge energy retardation voltage is 240 V and (b) without spark-discharge retardation voltage is 160 V. For both case the laser intensity is 1.5×10^{9} W/cm^{2}.

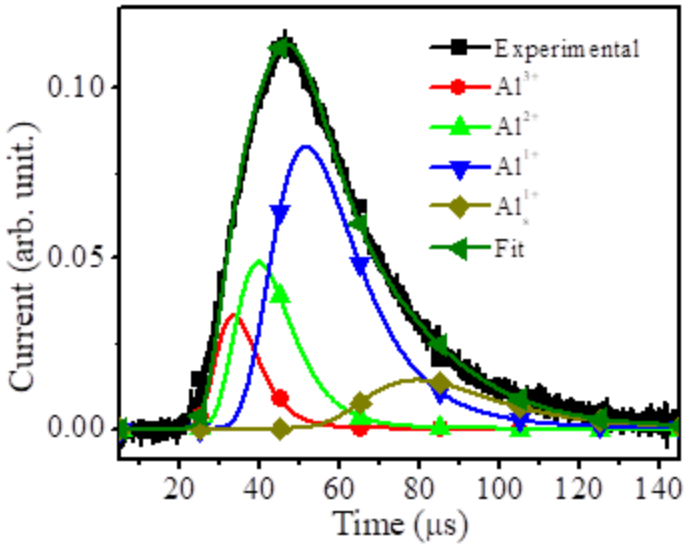

Fig. H.9 Deconvolution of the ion TOF signal into different ion charges, each with an SMB distribution. Al^{1+}, Al^{2+}, and Al^{3+} are used to fit the TOF signals to estimate the Ti~15 eV for a laser intensity of 1.5×10^{9} W/cm^2.

VITA

MD MAHMUDUR RAHMAN

(757) 550-9332 ● mrahm003@odu.edu ● www.linkedin.com/in/mr-rahman

Education

- *Old Dominion University, Norfolk, Virginia*
  Ph.D. candidate in Electrical and Computer Engineering — Dec 2019

- *Bangladesh University of Engineering and Technology, Dhaka*
  M.Sc. in Electrical & Electronics Engineering — Jun 2013

- *Military Institute of Science and Technology, Dhaka*
  B.Sc. in Electrical, Electronics & Communication Engineering — Jan 2010

Work Experience

Surface and metrology engineer — Aug 2019 – Present

Material and metrology group, ASML, Wilton, Connecticut, USA.

Graduate teaching assistant — Aug 2013 – Aug 2019

Department of Electrical & Computer Engineering, ODU, Norfolk, Virginia, USA

Lecturer — Jan 2010 – Jun 2013

Department of Electrical Engineering, Military Institute of Science & Technology, Dhaka, Bangladesh